University of Firenze

Facoltà di scienze matematiche, fisiche e naturali, Dipartimento di Fisica & LENS

Ph. Degree in Physics, cycle XXI, Academic year 2008/2009

Spectroscopy of single $GaAs$ nanoemitters towards quantum communication

Marco Abbarchi

December 2008

Supervisor: Prof. Massimo Gurioli

UNIVERSITY OF FIRENZE CANDIDATE DECLARATION:

I certify that the thesis entitled: *Spectroscopy of single GaAs nanoemitters towards quantum communication*, submitted for the degree of Doctor of Philosophy in Physics, contains no material that has been accepted for the award of any other degree or diploma. To the best of my knowledge, this thesis contains no material previously published or written by another author, except where due reference is made in the text of the thesis. All work presented is primarily the result of my own research.

Full Name: Marco Abbbarchi

Signed: ..... Date: .....

Abstract

The present work collects the foremost results obtained during the three years of my PhD degree. The aim of this research is the detailed characterization of the nanoemitters, stressing the accent on intrinsic and extrinsic aspects of the exciton and multiexciton radiative recombination, for testing their applicability as single and entangled photons emitters. The thesis contains specific studies related to optical and electronic properties of $GaAs/AlGaAs$ single nanostructures (quantum dots and concentric quantum rings) grown by Modified Droplet Epitaxy. The nanostructure radiative emission is investigated through micro–photoluminescence spectroscopy experiments at cryogenic temperature under laser excitation. The methods we used comprehend time resolved and time correlated spectroscopy, high spectral resolution measurements and magneto-optical characterization. The excitonic radiative recombination is studied under several points of view: firstly a large part of the investigation is devoted to the assignment of the main photoluminescence components of the single nanostructure to the corresponding excitonic transition (neutral exciton, neutral biexciton, charged complexes, etc...). Secondly we take into account specific features of the excitonic transitions: the line broadening and the related dephasing mechanism (spectral diffusion, phonon interaction), exciton dynamic, spin effects and photon correlation statistics.

Contents

General aspects

Starting from the latter half of the 20th century the miniaturization of semiconductor devices has led to increased integration and functionality, and to a reduced energy consumption. Semiconductor devices have evolved from millimeter-sized into micrometer-sized devices handling both electricity and light. Nowadays the challenge is nanometer-sized semiconductor devices that can both provide non-classical single-carrier and single-photon states [1, 2, 3]. Advanced epitaxial growth techniques enable the realization of high-quality semiconductor alloys under precisely controlled conditions, and open a new way in the semiconductor physics: the control over the nanostructure dimensionality and the consequent control of the carrier confinement. In the late 1980s the interest of researchers shifted from quasi two-dimensional nanostructures toward structures with further reduced dimensionality: quantum wires with quasi one-dimensional confinement and quantum dots (QDs) with quasi zero-dimensional confinement [4, 5, 6, 7, 8, 9]. Especially interesting are the modified electronic and optical properties of these structures, which are controllable to a certain degree through the flexibility in the structure design. The discrete energy level structure of semiconductor quantum dots opens new chapters both in fundamental physics, in which they can be regarded as artificial atoms, and in potential applications as devices [10, 11, 12]. Quantum dot materials have found potential applications as lasers, photon detectors, photon amplifiers, superluminescent LED. However, the full impact of QD technology is

yet to come especially in the emerging field of quantum communication.

Quantum dots and applications

Recent advances towards the development of QD optoelectronic devices for Quantum Communication offer many new physical aspects and possible applications that would be worth noticing. Here I would just stress the accent on some ideas that have recently sparked off an intense debate: the single photon emission [13, 14], the photons (and eventually carrier eigenstates) entanglement and related items [15, 16, 17, 18, 19].

The discrete nature of the electronic state in a QD makes possible the selection of the radiative recombination between two individual states (in a two level-like feature), which naturally gives a single photon emitter. The demand and the application of single photon sources is rapidly increasing since a single photon is a good prototype of a QBit, that represents the first step toward the implementation of quantum computation and quantum information protocols. Single photons can be used to encode a secret key in a quantum cryptography system as described in the work of Bennet and Brassard [20] where the QBit encoding is done on the polarization of a single photon. Further single photons can be transported over long distances enabling the exploitation of non-local properties of quantum states [21, 22, 23]. These aspects pose the accent on a peculiar characteristic of the QD system: the direct link between the confined carriers quantum states and the corresponding emitted photons.

Other possibilities are potentially offered by QDs technology in quantum computation and quantum information [24, 25, 26], for istance exploiting the multiparticle states formed in a QD, such as the biexciton complex (two electrons and two holes confined in a QDs usually indicated as XX). In fact the radiative recombination of the XX state toward the single neutral exciton (one electron

and one hole confined in a QD usually indicated as X) and the final X radiative relaxation toward the QD ground state [27] may result in the emission of polarization entangled photon pairs, under several conditions that strongly depend on the QD properties. Therefore one of the most interesting and promising aspects of the QDs phenomenology is nowadays the opportunity to implement a solid-state source of triggered, entangled photons pairs, for quantum computation and quantum information protocols dealing with *flying QBits* [15, 17, 28]. Emission of polarization entangled photons from biexciton recombination in a QD has been recently claimed [29], even if the result have been debated. Other interesting purposes in order to obtain entangled electronic states deal with laterally or vertically aligned QDs. In this case the entanglement is obtained via the exchange Coulomb interaction between charges confined in the two coupled nanostructures [26, 30] and/or entangled photon pairs. If the implementation of QDs as single photon source for quantum cryptography seems an affordable task, the possibility to use single QDs as building blocks of a quantum computer is far to come. In fact there are still relevant drawbacks due to the non-ideality of the QDs system that may complicate the possibility of obtaining an entangled photons source. For example, it is well known that the environment usually plays a relevant role in the QDs physics. In the case of quantum computation the non ideality of the QD/QBit may led to serious problems for a realistic implementation of some quantum computation algorithms. In this sense the five (more two) Di Vincenzo's criteria represent an useful framework in order to understand if a physical system may be or not a resource for the realization of a quantum computer. Nowadays the QDs properties cannot fulfill all the Di Vincenzo's criteria [31], especially for the scalability and the long dephasing time. Therefore it is actually important to investigate how the intrinsic and extrinsic properties of QDs can be tailored and to understand which aspect can be suitable and exploitable in order to obtain a realistic and working

quantum device.

0.1 The present work

GaAs/AlGaAs nanostructures

$GaAs$ and the related $Al_xGa_{1-x}As$ alloy have been intensively studied for more than forty years with tremendous improvement in the growth processes and in the characterization of their properties. These semiconductors form a family of important materials used not only as active elements in many devices but also as constituents of lattice matched heterostructures. A detailed review of the photoluminescence in $Al_xGa_{1-x}As$ materials can be found in ref. [32].

One of the most important steps in the exploitation of these materials was the planar growth of alternate layers of $GaAs$ and $Al_xGa_{1-x}As$ for the efficient realization of superlattices, quantum wells, Bragg mirrors, etc.., due to the almost perfect lattice match. Next steps of the research have seen the realization of lower dimensional $GaAs/Al_xGa_{1-x}As$ nanostructures, such as quantum wires and quantum dots. Therefore in a first stage, the effect of carriers confinement inside $GaAs/Al_xGa_{1-x}As$ quantum dots was obtained by studying interface fluctuations in narrow $GaAs/AlGaAs$ quantum wells [33]. Finally the invention of the modified droplet epitaxy technique (MDE) in 1991 [34] has led to the possibility to realize effective three-dimensional $GaAs$ islands on top of a $AlGaAs$ surface, avoiding the usual two-dimensional layered growth. Such non conventional growth method has opened the route to a novel generation of quasi 0D nanostructures even using lattice matched materials.

The present thesis is an investigation of these peculiar strain-free nanostructures by using high resolution spectroscopy. With respect to conventional Stranski-Krastanov QDs, where the growth is realized via strain associated to the islands

and the barrier material [35], the advantages of *MDE* are evident. On one side *MDE* offers a larger choice of QDs materials and in particular it allows the use of high quality compounds as the *GaAs* system. On the other side, as will be deeply underlined in the following, the residual strain in the *SK* growth is known to be at the basis of several problems in the optical quality of the QDs, such as piezoelectricity, e–h separation, In segregation, etc.. . In this sense, one advantage of *MDE* is the possibility to obtain strain-free nanocrystals, allowing a simpler description of the relevant physics and an easier interpretation of the experimental data. More generally the *MDE* growth is a very versatile technique and presents many advantages that will be widely discussed all over the present work. For example, MDE makes possible the formation of conventional QDs but also exotic nanostructures such as quantum ring, double concentric quantum rings and quantum dot molecules [36, 37]. The *GaAs/AlGaAs MDE* nanostructures present an intense photoluminescence (PL) emission from quantum confined excitons radiative recombination. The emission spectral window is usually centered at $680-750$ nm and the tuning is possible by changing the nanostructures size and the material composition. This is a further remarkable difference respect to the conventional *InAs SK* quantum dots, where the PL emission lies in the near infrared region down to the telecommunication window of the commercial optical fiber ($1300nm$). At the same time, for practical application such as single photon emitters, however, it would be desirable to work in wavelengths where commercial silicon-based single photon detectors reach their maximum quantum efficiency (up to 70% around 700 nm) and this is fulfilled by *GaAs MDE* nanostructures.

Outline of the thesis

The present research is an investigation of the main topics related to optical and electronic (excitonic) properties of self assembled *GaAs/AlGaAs* nanostructures

growth by *MDE* with particular attention to the *QD* and concentric quantum ring (*CQR*) cases. The experimental technique is photoluminescence spectroscopy of single emitters excited by continuous and pulsed laser beams.

The aim of this work is the detailed characterization of *MDE* nanostructures, putting the accent on intrinsic and extrinsic properties of the exciton and multi-exciton radiative recombination, for testing their applicability as single and entangled photons emitters. As demonstrated in the wide literature related to excitonic recombination inside a quantum potential, there are many questions still under study and far to be completely solved. Several features of the line shape of excitonic radiative recombination are here studied including the inhomogeneous line broadening and related phenomena such as the Coulomb interaction with trapped charges or the exciton-phonon interaction at high temperature. Taking advantage of the lack of strain in the *GaAs/AlGaAs* compound, the fine structure splitting is evaluated as effect due to geometrical anisotropy of the confining potential. Further the photon correlation is investigated as assignment method for the spectral lines and as a test for single photon emission. Finally the *GaAs/AlGaAs* concentric quantum ring nanostructures are taken into account in a pioneering investigation of their optical and electronic properties.

This thesis is organized as follows:

In Chapter 1, the main features of the excitonic radiative recombination in *QD*s are theoretically described. The condition in which the *QD* system can be regarded as source of single photons and/or a polarization entangled photons are also reviewed.

Chapter 2 displays some experimental issues presented in this thesis. In the first part, *MDE* nanostructure growth and morphology are described. In the second part, all the experimental apparatuses and investigation methods are addressed.

Chapter 3 reports the results of CW measurements, with particular attention

to the inhomogeneous broadening and decoherence mechanisms. The investigated aspects are the quantum confined Stark shift induced by charges in the QD environment (spectral diffusion) and temperature dependent measurement to provide information on the exciton-phonon interaction (polaronic effect).

In Chapter 4 time resolved measurements are presented to access kinetics of the exciton recombination. In order to give a clear interpretation of the sidebands nature in the exciton radiative recombination at high temperature, the exciton 0-phonon line and sidebands lifetime are studied. Besides, the quantum size effect on exciton lifetime at low temperature is studied.

Chapter 5 is a review of polarization resolved measurements. A study of the exciton fine structure in magnetic field is presented providing information on intrinsic features of $GaAs/AlGaAs$ QDs such as Landè g factor and diamagnetic shift. In addition, high resolution, polarization resolved measurements are performed in order to study the fine structure splitting at 0-magnetic field.

In Chapter 6, by time correlated measurement performed using an Hanbury-Brown and Twiss interferometer, the single photon emission and exciton correlation properties are studied. The bunching/antibunching feature of the second order correlation function ($g^{(2)}$) for the different spectral components of the PL emission provides information on the QD occupation, exciton dynamics and on the single photon emission properties of $GaAs/AlGaAs$ QDs.

In Chapter 7 we report CQR photoluminescence experiments. The specific study on CQRs deals with time resolved and time correlated measurements. This investigation provides additional information on the line broadening mechanism and thus on the exciton dynamics in these particular ring-shaped nanostructures. Further the single photon emission from individual CQR is discussed.

Chapter 1

Quantum dot level structure

In the following section the relevant phenomena related to the excitonic complexes recombination are shortly analyzed for discussing how the emission of single photons and entangled photons pairs can be obtained.

1.1 Neutral exciton, trion and biexciton complexes

Electron and hole, confined in a QD bind to form an exciton (X) through their mutual Coulomb interaction. The confinement in a nanometer sized quantum box influence the (X) dynamics being the electronic states quantized.

A naif representation of the exciton formation and recombination in a QD is presented in Fig.1.1. After the optical excitation of electrons and holes in the barrier and the consequent energy relaxation, the carriers can be captured in the QD and then recombine emitting a photon. When a single X (Fig.1.1 (a)) is created inside the QD, the radiative recombination results in a sharp line in the photoluminescence (PL) spectrum (note that the same symbol X is used to label the carriers complex in the QD and the corresponding line in the PL spectrum).

The underlying atom-like two-level structure of a single QD exciton transition can lead to nonclassical light emission, i.e., photon antibunching and sub-Poissonian photon statistics [38]. After the photon emission, the system is in the inactive ground state and a second photon cannot be emitted. The emission probability recovers its mean value only after the excited-state occupancy reaches the steady-state population, determined by the excitation and relaxation rates. The dead-time between successive photon emission events leads to photon antibunching and sub-Poissonian photon statistics. In fact, the X level is characterized by a radiative lifetime τ_r (as short as $\sim 1ns$) and we cannot expect to observe two photons in a time interval shorter than τ_r.

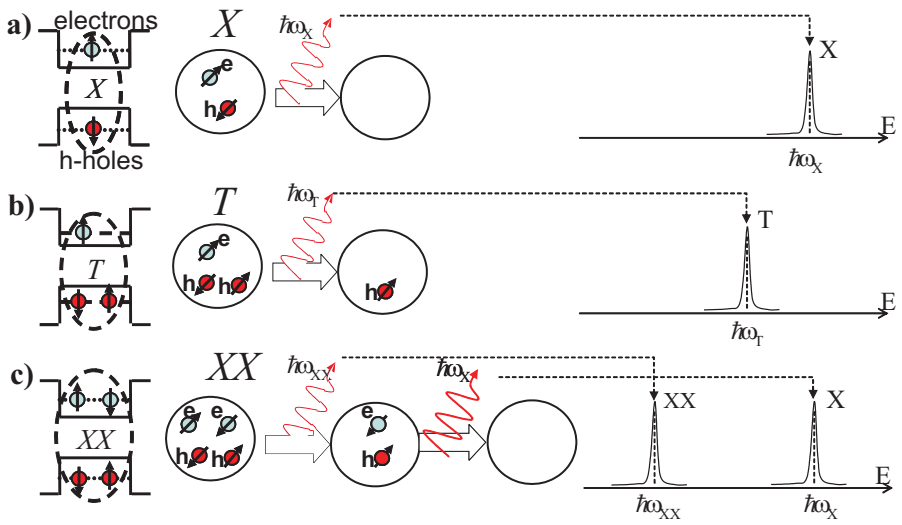

Figure 1.1: (a), (b) and (c): recombination scheme of neutral exciton X, charged exciton T and neutral biexciton XX respectively. The excitonic complexes are captured in the QD (represented as confining well potential for electrons and holes in conduction and valence band). In the first case (a) the X recombination leaves an empty QD and produces a single sharp line in the PL spectrum. In the second case (b) the trion recombines leaving an uncoupled charge in the QD producing a sharp line shifted in energy respect to the X case. In the last case (c) is represented the XX recombination which gives rise to a sharp line in the spectrum at lower energy than X and leaves the QD occupied by a X complex which recombines as described in the case (a).

Other frequently observed excitonic complexes are the charged excitons or trions T. In Fig.1.1 (b) the example of a positively charged T is shown. When the QD is occupied by an X and a spectator charge (a hole in the example of Fig. 1.1 (b)) the recombination energy of the $e-h$ pair is shifted depending on the sign of the additional charge and the QD geometry. The T recombination process leaves the QD occupied by a single charge previously present in the QD due to dopant defects or to extrinsic charge capture. The difference in energy between the X and T optical transitions is denominated binding energy [typically the T binding energy of our QD s varies around 1 and 2 meV, that is a large splitting compared to the line broadening which is between tens to hundreds of μeV]. Since the presence of X and T complexes in the QD are mutually exclusive, their spectral contributions can be recognized and isolated [39]. We are again in presence of a two-level like recombination and the T complex can also be regarded as a single photon source.

The last excitonic complex considered here is the biexciton XX (see Fig.1.1 (c)). When two $e-h$ pairs are captured in the QD the first state in conduction and valence band is filled by two electrons and two holes, respectively. The recombination of one of the two excitons results in a sharp line with lower energy respect to the X case, being the process influenced by the presence of the second $e-h$ pair. Typically the binding energy of biexcitons for $GaAs/AlGaAs$ QDs is in the range 2-5 meV. The recombination of one exciton leaves the QD in the X state that, as previously described, recombines emitting an X photon. In this peculiar recombination cascade, there is a direct correlation in the $XX-X$ photons which allows to obtain correlated photon pairs and eventually to produce polarization entangled photon pairs.

In conclusion of this review, let us briefly mention multiexciton (MX) states often observed in PL experiments. The QD state filling with more than two excitons produces radiative recombination denominated MX. The correspondent

emission spectrum is composed by several sharp lines and broad bands either at higher and lower energy respect to the fundamental X transition [40].

1.2 Fine structure of quantum dot excitons

We now introduce the spin configurations of the carriers bound to form excitonic complexes. In the case of the neutral exciton X the two carriers involved in the radiative recombination process have a definite spin, as schematically illustrated by Fig.1.1 (here we will only consider heavy holes states). The four excitons formed by the different spin combinations are characterized by their angular momentum $M = J_{\mathbf{h},z} + S_{\mathbf{e},z}$ where $J_{h,z} = \pm 3/2$ and $S_{e,z} = \pm 1/2$ are the hole and electron spin along the z axis, respectively [41]. The coupling with the radiation field is allowed only for the $M = \pm 1$ complex that is usually indicated as bright exciton, while for $M = \pm 2$ we obtain the dark exciton. In the present work we will always refer to the bright states $M = \pm 1$.

In presence of an ideal quantum dot, with perfect cylindrical symmetry around the z direction, the X levels with $M = \pm 1$ are degenerate and energetically indistinguishable, as summarized in Fig.1.2 (a) assuming orthogonal polarization Π^X and Π^Y. Taking into account the step of the recombination involving the X complex, the final electromagnetic field state can be interpreted as the superposition of the two opposite polarization states of the emitted photons and is described by Eq.1.1. In this sense the emitted photon can be considered as a $flying\ QBit$.

$$|\psi_f\rangle = \frac{|\Pi^X, \hbar\omega_X\rangle + |\Pi^Y, \hbar\omega_X\rangle}{\sqrt{2}} = \frac{|\Pi^X\rangle + |\Pi^Y\rangle}{\sqrt{2}} * |\hbar\omega_X\rangle \equiv \frac{|1\rangle + |0\rangle}{\sqrt{2}} \qquad (1.1)$$

The final state $|\psi_f\rangle$ of the X recombination is (for any chosen polarization basis) the superposition of the two photon states with opposite polarization $|\Pi^{X,Y}\rangle$ and energy $\hbar\omega_X$. Encoding the basis states $|1\rangle$ and $|0\rangle$ in the photon polarization and

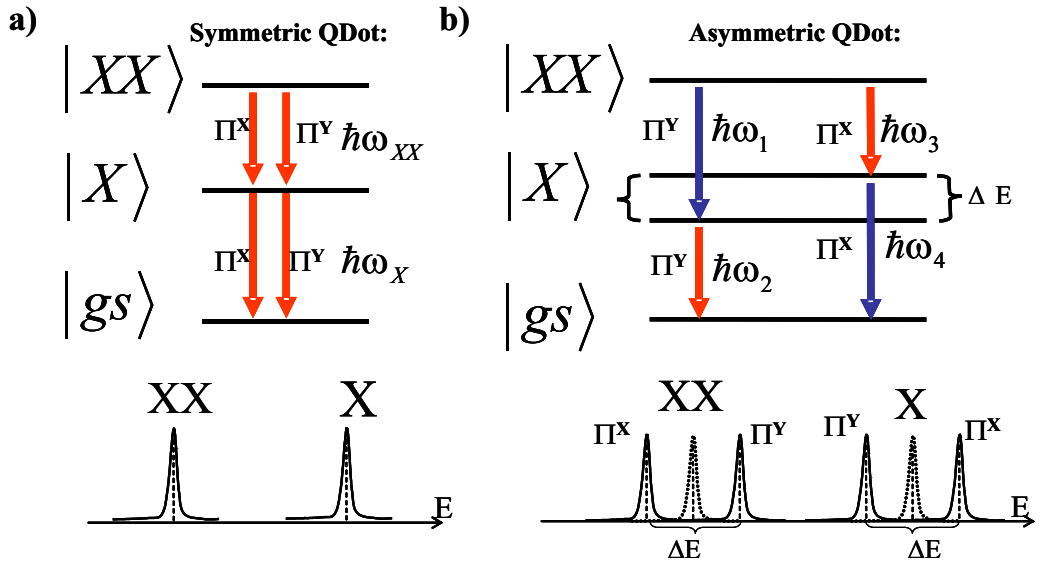

Figure 1.2: Recombination scheme of the X and XX compounds and corresponding features of the *PL* spectrum for a cylindrical symmetric *QD* (a), and an asymmetric *QD* (b)

tracing out the others degree of freedom (in this case acting a spectral filtering) we obtain a photonic $QBit$. The case of the T state can be schematized in a similar manner of the X case. The photon polarization obtained in the T recombination is described by 1.1 while the emission energy is different. The final state $|\psi_f\rangle$ comprehends the spectator charge in the QD but the photonic part can be isolated and the $QBit$ is encoded in the same way of the X case.

In the hypotheses of perfect QD symmetry is also possible to obtain polarization entangled photon pairs in the XX $\rightarrow$X $\rightarrow$ gs transition (see Fig.1.2). The XX is a singlet spin state and the associated spin interaction is in any case zero. The recombination from paths for the two XX spin states are equally probable and indistinguishable, the same is for the X recombination path (being the X level degenerate). In this situation the final photonic state after the almost simultaneous radiative cascade XX $\rightarrow$X $\rightarrow$ gs is described by Eq.1.2. Encoding the QBit in the photons polarization and tracing out the other degrees of freedom we can get an

entangled Bell state as summarized in Eq.1.2.

$$|\psi_f\rangle = \frac{|\Pi^X, \hbar\omega_X; \Pi^X, \hbar\omega_{XX}\rangle + |\Pi^Y, \hbar\omega_X; \Pi^Y, \hbar\omega_{XX}\rangle}{\sqrt{2}} = \frac{|\Pi^X; \Pi^X\rangle + |\Pi^Y; \Pi^Y\rangle}{\sqrt{2}} * |\hbar\omega_X; \hbar\omega_{XX}\rangle \equiv \frac{|11\rangle + |00\rangle}{\sqrt{2}} \tag{1.2}$$

In a real QD several effects may influence the Hamiltonian symmetry. It is commonly recognized that the piezoelectric field (eventually introduced by strain in the crystal structure) and geometrical asymmetries of the QD, break the exciton Hamiltonian introducing an $e-h$ fine interaction (anisotropic exchange interaction) of the X level [42]. The polarization splitting, usually indicated as fine structure splitting (FSS), of the XX emission is identical to that of the X complex because the XX is a spin-singlet state. The two electrons (holes) in conduction (valence) bands have a zero total spin and even in an asymmetric potential there is not fine interaction. The XX exhibits neither exchange nor Zeeman interaction splitting [41, 43, 44], therefore, in the optical spectra any FSS of the emission is fully determined by the FSS of the X complex in the final state of the electron-hole recombination. Within this energy scheme of the XX $\rightarrow$X $\rightarrow$ gs cascade (see panel (b) of Fig.1.2) the two allowed XX recombination paths are energetically distinguishable.

$$|\psi_f\rangle = \frac{|\Pi^Y, \hbar\omega_1; \Pi^Y, \hbar\omega_2\rangle + |\Pi^X, \hbar\omega_3; \Pi^X, \hbar\omega_4\rangle}{\sqrt{2}} \tag{1.3}$$

The final state of the two emitted photons (Eq.1.3) has not the same entanglement scheme of Eq.1.2: the energy state is now completely mixed with the photon polarization state and the wavefunction cannot be factorized in the two degrees of freedom. Even if several theoretical and experimental proposal have been made in order to recover the polarization entanglement scheme [29, 45, 46], the Hamiltonian

asymmetry forbids an easy exploitation of the QD emission.

Finally we mention how the charged exciton T does not show any FSS. Since the charge displacement in the QD determines a zero total spin of the conduction or valence band in the initial and final state of the recombination the T complex is never influenced by the exchange interaction.

Chapter 2

Experimental

*In this chapter the $GaAs/AlGaAs$ nanostructures and the experimental techniques related to this thesis are presented. In the first part the features of the modified droplet epitaxy (*MDE*) growth method are shortly described. The overview of the band structure of the $Al_xGa_{1-x}As$ compounds and the exciton formation in the $GaAs/AlGaAs$ quantum dot system overcomes the aim of the present work and we refer to literature for a detailed description [47, 48, 49, 50, 51, 52]. In the second part the most important properties and performances of the experimental apparatuses are described.*

2.1 Modified Droplet Epitaxy

In the last two decades, several fabrication methods have been reported for the efficient growth of quantum dots with high crystallin quality and improved optical quality. The most common technique is self organized nucleation of QDs constituted by lattice mismatched materials, such as $In(Ga)As/GaAs$, which have been

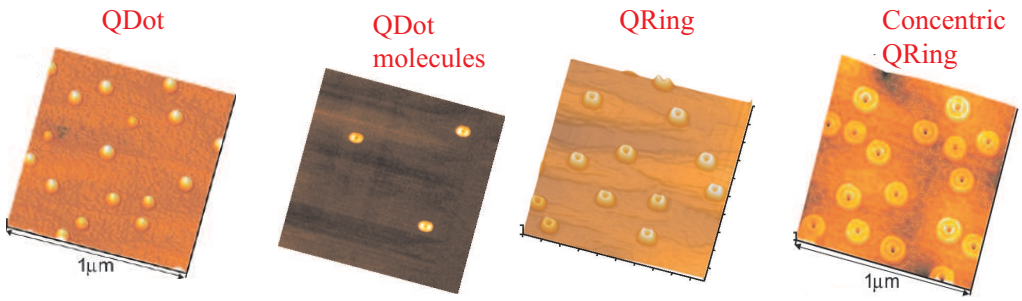

Figure 2.1: Differen type of *GaAs/AlGaAsMDE* nanostructures: AFM images ($1\mu \times 1\mu$) of uncapped samples.

successfully obtained by the Stranski-Krastanov (SK) method in 1993 [35]. A significant amount of lattice strain is a relevant characteristic of SK nanostructures being the lattice mismatch a key point in the QD formation. Further, more in order to obtain good crystalline quality, a wetting layer of the same QD material is usually present on top of the barrier material. The presence of both strain and wetting layer affects the QD electronic and optical properties. To overcome such limitations obtaining self-assembled nanostructures, a different method of fabrication of lattice-matched and lattice-mismatched materials [53] based on molecular beam epitaxy (MBE), is the modified droplet epitaxy (MDE) [54, 55]. MDE is a non conventional growth method for III-V compounds developed by N. Koguchi and coworkers in the NIMS laboratory of Tsukuba, Japan. This method is the evolution of the droplet epitaxy that was tuned-up in the 1991 [34]. The modified droplet epitaxy [34], owing to its intrinsic high designability, allows the growth of a large variety of different materials and structures, ranging form quantum dots [56, 57, 58], quantum dots molecules [37] and quantum rings as shown in Fig.2.1 [36, 59, 60, 61]. Such technique permits also the realization of nanostructures with extremely low areal densities (down to few $10^8 QDs \cdot cm^{-2}$) allowing single nanocrystal spectroscopic characterization with no need of further sample processing. Further, the independent tuning of nanostructure sizes and densities can be ob-

tained. A detailed description of the *MDE* growth method overcomes the aim of this thesis and here I will briefly describe the prominent aspects of the typical *GaAs/AlGaAs* nanostructure growth, giving an example of its versatility.

2.1.1 GaAs/AlGaAs Quantum dot to Concentric Quantum ring transition

Making use of *MDE* it is possible to realize a series of different *GaAs/AlGaAs* nanostructures, starting from the same initial *Ga* droplet configuration, in which the nanostructure (*NS*) morphology is progressively changed, from *GaAs/AlGaAs* lens shaped *QD*, to single quantum ring (*QR*) and, eventually, to concentric quantum ring (*CQR*) structures.

The investigated samples are grown by *MDE* in a conventional *MBE* reactor. The growth scheme is as follows. After the growth of 300 nm *GaAs* buffer layer and 400 nm $Al_{0.3}Ga_{0.7}$As barrier layer at 580 °C by MBE, the substrate temperature is lowered to 200 °C, the *As* valve closed and the *As* pressure in the growth chamber depleted. Supplying only *Ga* cation atoms at this temperature and in absence of *As*, the initially deposited *Ga* atoms are incorporated into the *As* terminated surface resulting in a *Ga* stabilized surface. Subsequent *Ga* deposition allows to the formation of tiny *Ga* droplets on the substrate with high circular symmetry. In the present example the samples are prepared by supplying a total amount of *Ga* of 3.75 monolayers (MLs) (at 0.5 ML/s rate), where we indicate as 1 ML of *Ga* the amount of cations necessary to obtain 1 ML of *GaAs* in presence of *As*. Following the deposition of the droplets, and maintaining the substrate temperature at 200 °C, an As_4 molecular beam with fluxes in the range 2×10^{-4} – 5×10^{-6} Torr beam equivalent pressure (BEP) is irradiated on the surface. This growth step causes the complete arsenization of the *Ga* contained in the droplets into nanometer size crystals. By choosing the appropriate *As* flux during the latter

step the control of the NS shape is obtained, in fact the NS morphology shows a marked dependence on the As flux [54, 36, 59, 60] (as shown in the three bottom panels of Fig. 2.2). When the As flux is 2×10^{-4} Torr BEP, the droplet are frozen in their initial configuration, thus permitting the formation of lens shaped QDs, with an average height of ≈ 7 nm and a base of ≈ 30 nm . As the Arsenic pressure decreases, the shape of the NS develops a well defined hole in the middle, thus changing toward a ring structure [36]. When the As flux is 4×10^{-5} Torr BEP, the shape of NSs is ring–like, with an average base size which does not strongly differ from those of the QDs (≈ 40 nm) but with a noticeable reduction in the maximum height, now ≈ 2 nm (see the second panel in Fig. 2.2). Further reduction in the As flux down to 1×10^{-5} Torr BEP does not induce strong changes in the NS shape: the NSs remain ring–like, assuming a more regular shape. Decreasing the As pressure below 5×10^{-6} Torr BEP induces major changes in the NS shape. A second annular structure now encircles a small internal ring, producing a double concentric ring structure (third panel in Fig. 2.2). The inner ring radius is around $\sim$15 nm, while the outer ring radius reaches the $\sim$50 nm value. The height of both rings is reduced to 1.5 nm. It is worth mentioning that the two structures are not well defined in all the directions, as shown in Fig. 2.2 by the AFM profile of a single $CQR\ MDE - NS$, where the two rings tend to merge along the $[0\bar{1}1]$ direction. Better definition of the two rings can be obtained by a further decrease of the As flux (down to 2×10^{-6} Torr BEP) during the arsenization step as reported in ref. [59] (see also Section 7.1.

After the complete arsenization of the Ga droplets, a growth interruption of 10 min at 350 °C at constant As flux is performed. Then, an $Al_{0.3}Ga_{0.7}As$ barrier layer of 50 nm was grown by migration enhanced epitaxy (MEE) [62] at the same temperature of 350 °C. Finally, the samples are annealed (10 min at 650 °C under As flux) in the chamber. A second set of samples is grown without capping in the

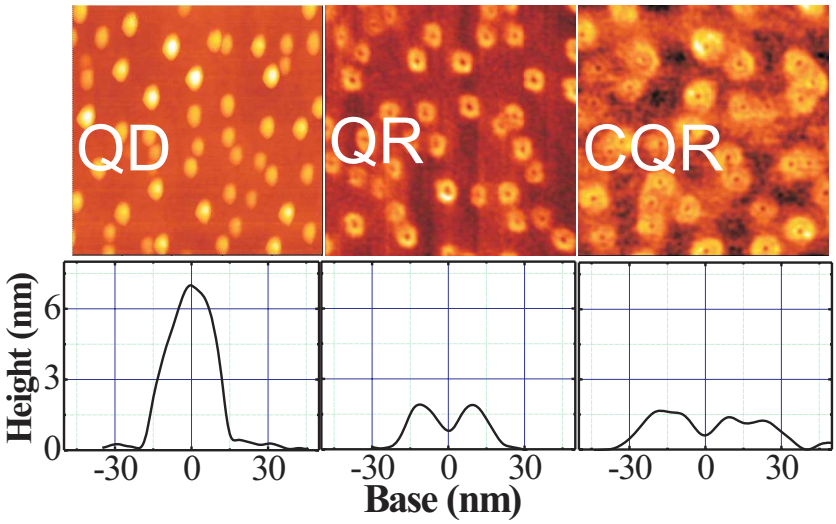

Figure 2.2: AFM images (500 nm$\times$ 500nm) of the uncapped samples.

same conditions for morphologic characterization.

The surface of the uncapped samples was observed via Atomic Force Microscope (AFM). Typical example of AFM images of uncapped samples are shown in Fig. 2.2. The areal density of the NSs, irrespective whether they are QDs, QRs or CQRs, is similar: $\approx 1 \times 10^{10}$ cm^{-2} [lower ($\approx 6 \times 10^{8}$ cm^{-2}) when the growth conditions are optimized for CQR]. The density is determined by the initial droplet density which, in turn, shows a marked dependence on the substrate temperature [63]. It's worth noting that MDE growth allows an independent tuning of NS size and density.

The optical characterization was performed by macro–photoluminescence spectra measured at 15 K using a closed cycle cold finger cryostat. The PL was excited with an $Nd:YAG$ duplicated laser ($\lambda_{\text{exc}} = 532$ nm). The excitation power density was 10 W/cm^2. The spectra were measured by a grating monochromator operating with a Peltier cooled CCD camera.

The PL spectra of the as grown samples at $T = 15$ K are reported in Fig. 2.3 a). All the samples show a PL characterized by a broad emission band located

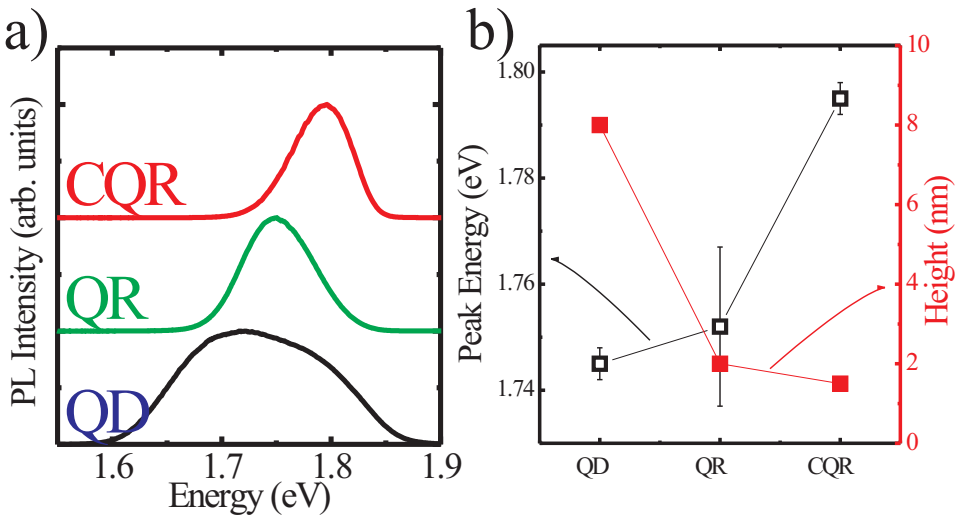

Figure 2.3: a): normalized PL spectra of QDs, QRs and CQRs (as grown) samples at T= 15 K and 10W/cm^2 laser power density (the spectra are vertically shifted for clarity). b)Peak energy (left scale, open squares) and nanostructure height (right scale, full squares) for QDs, QRs and CQRs (as grown).

between the $GaAs$ and the $Al_{0.3}Ga_{0.7}As$ energy gaps. The emission of QDs is peaked at $E_{\text{peak}} = 1.738$ eV with a Full Width at Half Maximum ($FWHM$) of 110 meV. QRs emission is characterized by a narrower ($FWHM = 75$ meV) and slightly blue-shifted ($E_{\text{peak}} = 1.74$ eV) band, respect to that of QDs. As shown in Fig. 2.3 b) the anticorrelation of the PL shift and the NS maximum height is an indirect proof of the morphology effect on the carrier confinement. A common feature of all the ring structures, when compared to the standard QDs sample is a reduction of the PL yield. In the present case the emission from QRs is $\sim$30 times smaller than QDs. PL emission, with intensity comparable to that of QDs (only a factor four), is observed in the case of the CQRs sample. The PL band is, on the other side, strongly blue-shifted ($E_{\text{peak}} = 1.792$ eV) and narrower ($FWHM = 60$ meV) with respect to QDs. The observed changes in the PL yield are related to the growth conditions. In fact the MDE nucleation mechanism

relies on growth kinetic at low-T in order to obtain high structure flexibility, even if low T implies more defective as-grown material. Two steps can be considered critical in determining both the structural flexibility of the growth technique and the material defectivity: (i) the droplet arsenization step, conducted at low–T and high beam flux; (ii) the initial 10 nm of $AlGaAs$ barrier, grown by migration enhanced epitaxy (MEE) at an extremely low–T. The correct choice of As flux and substrate T, through the control of the $GaAs$ formation kinetic, allows to determine the NS shape. On the other side, the incomplete diffusion of As inside the Ga droplets is one of the major problems affecting the crystalline quality in the MDE–NS. Also the first layers of the barrier must be grown at low–T, in order to freeze the NSs in the achieved form and prevent them from reaching the $GaAs$ thermodynamical equilibrium state, that is a flat epilayer. MEE growth procedure is used in this process step, that is a growth method which permits to obtain good quality layers even at substantially low growth–T [62]. Nevertheless the temperatures used in MDE are by far lower than the one used in ordinary MEE, thus producing a defected $AlGaAs$ layer in the region just above the NSs. For that reason a post growth annealing is usually necessary [64].

2.2 Single nanostructure spectroscopy

Even though important information can be extracted from the study of an ensemble of nanoparticles using conventional PL techniques, it is well known that the possibility of performing experiments with a microprobe allows to retrieve information on a single QD. In fact, it is established that structural disorder plays a major role in determining the spectral features of the nanoobjects, as a consequence of the inhomogeneous broadening that may represent a limitation for some application, as for example low threshold lasers.

Within the typical inhomogeneous PL line (broadening of tens of meV) it is not possible to discriminate on the local properties of the dot such as different exciton complexes, single photon emission, spin effects, etc.. . Moreover, measurements on an ensemble of QDs cannot resolve between biexcitons, trions and p-state recombination, which are expected to have very different features. Finally, variations of the QD size can produce a spread in the oscillator strength which is somehow averaged when the PL from the ensemble is studied. It is therefore clear that a great help can be given by microprobe techniques, which, providing high spatial resolution, give information on the properties of the single emitters. Among the several techniques, microphotoluminescence (μPL) and scanning near-field optical spectroscopy (NSOM) are probably the most widely used, since they can be implemented in a wide spectral range (UV to IR) and different experimental setups have been realized to combine spatial and temporal resolution to explore the dynamical properties of the nanoobjects [10, 65, 66, 67, 68, 69]. While microPL spatial resolution is substantially limited by the diffraction of the lightwave, NSOM spectroscopy is in principle limited only by the aperture of the probe (50-100 nm). The price to be paid is usually a strong reduction in sensitivity. Moreover the implementation of a NSOM apparatus for temperature-dependent measurements is not an easy task, so that, most of the recent experiments on single quantum dots has been performed by μPL experiments.

2.2.1 Experimental apparatus

The general scheme of the experimental apparatus is summarized in Fig. 2.4. The main building blocks are four: the laser sources, the cryogenic apparatus (ultra-low vibration cryostat), the confocal microscope, the spectroscopy apparatus for the PL analysis. The different parts are evidenced in Fig.2.4 by dashed rectangles.

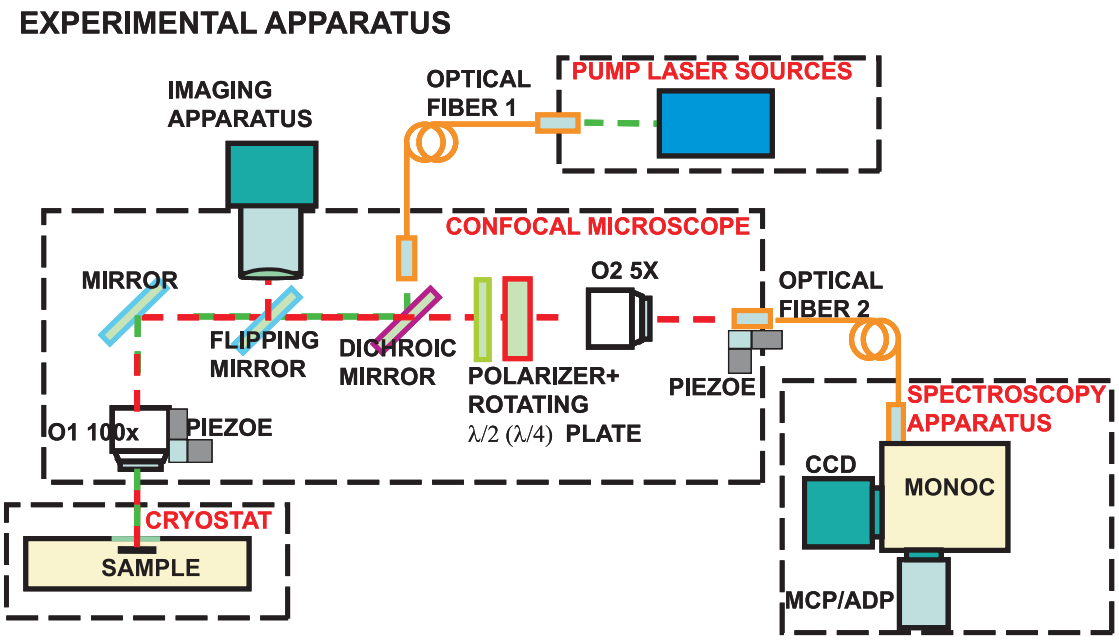

Figure 2.4: Scheme of the experimental apparatus. The main building blocks are evidenced by dashed rectangles.

Cryogenic apparatus

We used an ultra low vibration cold finger cryostat (Janis ST 500), working with either liquid Helium or Nitrogen, which allows a fine tuning of the sample temperature between 4.4 K to room temperature. Its peculiar feature is the possibility to work with no help of pumps but just with the pressure formed in the dewar containing the cooling liquid. For magneto photoluminescence measurements we used an Oxford cryostat modified for the insertion of a superconductive magnetic coil.

Laser sources

The CW sources are a frequency doubled $Nd:YAG$ laser emitting at 532 nm, $HeNe$ lasers emitting at 633 nm and 534 nm. The pulsed sources are a dye laser at 600 nm (pumped by the second harmonic of a $Nd:Yag$ laser) emitting 2 ps pulses

with a repetition rate of 76 MHz and the second harmonic of a $Ti:Sapphire$ laser emitting 100 fs pulses with a repetition rate of 82 MHz at 400 nm.

Microscopy apparatus

The PL collection is performed by a high numerical aperture microscopy objective working in confocal configuration with a second microscopy objective. In all the experiments the lateral spatial resolution ($\sim$1 μm) of the confocal microscope is always determined by the diffraction limit of the main objective O_1 (the diameter dimension of the confocal fiber is usually 3.5 μm and it is selected in order to exploit that resolution limit).

The control of the microscope position in the horizontal plane, parallel to the optical table, is controlled by mechanical stages with a spatial resolution of 25 μm. Either the main objective O_1 and the confocal optical fiber are mounted on mechanical translation stages with a resolution of 5 μm. The focusing of O_1 in the z vertical direction and the lateral $x-y$ adjustments of the confocal optical fiber are finely tuned by piezo stages. Finally the position of the excitation/collection on the sample can be finely tuned adjusting the position of the mirror on the top of O_1 with micrometer screws.

The microscope is equipped with an imaging apparatus formed by a 200mm-focal length photographic objective, a commercial silicon-based CCD camera and a white lamp light (not shown in the figure) for the sample illumination.

The excitation laser beam is focused on the sample using the main objective O_1. The laser beam is aligned on the PL optical path by using an optical fiber, achromatic collimating lens (not shown) and a dichroic mirror. The dichroic mirror allows the separation of the collected PL and the excitation beam. The excited area on the sample is determined by the fiber core diameter, the focal length of the collimation lens and of O_1 and is usually of the order of 10 μm. Alternatively

the PL excitation can be realized through the cryostat window focusing the laser beam on the sample with a lens. In this case the spot size is about 50 μm diameter. In both cases the excitation spot dimension is much larger than the microscope resolution thus allowing almost uniform excitation of the PL over a large portion of the sample.

Finally it is worth noticing that the reached spatial resolution joined to the areal density of the *MDE* nanostructures allows an easy distinction of PL emission from different nanostructures. In fact, we can usually collect the PL from a few nanoemitters that are spectrally separated due to the size dispersion.

Spectroscopy apparatus

The collected photoluminescence is dispersed by a grating spectrometer in which is fed through the confocal optical fiber. The use of the optical fiber allows to easily interchange the monochromator for different experiments. In fact we can use an high resolution setup for CW measurements with a silicon based CCD camera or a lower resolution setup for time resolved investigation with fast detectors.

Typically the PL emission from excitons in a QD is characterized by a series of sharp lines. Both the line broadening and the fine splitting of the energy levels could be as small as $\sim$10 μeV. Therefore a detailed spectral analysis of the single QD photoluminescence needs high resolution measurements, in order to carefully determine line shape and broadening. For high resolution PL we used a U1000 Jobin-Yvon, 1 m-focal length, double grating monochromator obtaining a spectral resolution better than 25 μeV. We also equipped the confocal apparatus with a polarizer and a rotating half (quarter) wave plate for linear (circular) polarization detection. The selection of the detected PL polarization was performed before the collection in the confocal optical fiber as shown in Fig.2.4.

For time resolved measurements, where a high spectral resolution is not re-

quired, the implemented setup was equipped with a Czerny-Turner, 0.3 m focal length, single grating spectrometer Acton Spectra Pro 2300i. In one of the two spectrometer exits the PL is detected by using a silicon based CCD camera. The second exit of the spectrometer allows the selection of a sharp portion of the spectrum through the use of a slit. This selection makes possible the investigation of the temporal dynamics of carriers-complexes inside the nanostructure by a time correlated single photon counting setup ($TCSPC$) as discussed later. The spectral resolution of the stup for time resolved experiments is of the order of 250 μeV (expressed as full width at half maximum, or $FWHM$, of a sharp HeNe laser line).

Magneto-photoluminescence

The study of the fine structure of energy levels is also performed in presence of an external applied magnetic field. The used setup, developed in the *Quantum Dot research center* in the NIMS laboratory in Tsukuba (Japan), is conceptually identical to that shown in Fig.2.4 and in addition is equipped of a superconductive magnetic coil providing a variable magnetic field finely tunable between 0 and 5 Tesla. All the measurements are performed in Faraday configuration, where the applied magnetic field is parallel to the z sample growth direction (the vertical symmetry axis of the nanostructures). This allows to study either the Zeeman splitting and the diamagnetic shift providing information about the spin configuration of the carries involved in the recombination process.

Further details of this kind of measurements will be discussed in the specific Section 5.1.

Time-resolved and time-correlated spectroscopy

The time resolved and time correlated experiments are of the utmost importance in this work since they represent a powerful tool to investigate the confined car-

riers dynamics. Besides, this investigation can provide information on the single photon emission properties of single nanostructures, allowing a deep insight into the electronic structure and the state filling.

The radiative transitions from QD excitonic levels usually present radiative lifetimes as short as $\approx$ 1ns, while the charge capture is typically shorter ($\approx 10 - 100$ ps). Therefore the charge dynamics investigation is performed by using fast detectors. We used two detectors: a micro channel plate phototube (MCPT Hamamatsu R3809U51) for time resolved analysis and two avalanche photodiodes (APD Perkin Elmer SPCM-AQR) for time correlated experiments. The estimation of the time resolution is performed by selecting the pulsed laser line through the spectrometer exit slit and adjusting the detected laser intensity to a count rate similar to the typical PL intensity. In the first case the MCPT temporal resolution is about 70 ps while in the second case, for the APD detector, is about 600 ps (expressed as $FWHM$ of the time response of the pulsed laser source). For lifetime measurements we used a time correlated single photon counting ($TCSPC$) method. The photon arrival statistics on a single-photon detector is measured by a Time to Amplitude Converter (TAC) triggered by the laser pulses. The START signal is provided by the detection of a PL photon and the STOP by the laser trigger. The time delay Δ from START and STOP generates output of the TAC with amplitude proportional to Δ. The analog signal is converted by an ADC. In this way is possible to build a histogram of the time delay events and to reconstruct the photon statistics.

Intensity time correlated measurements are made with an Hanbury-Brown and Twiss (HBT) interferometer, providing further information on the photon statistic. The HBT interferometer is a useful tool to study the $g^{(2)}$ function that allows to test the single photon emission and to investigate the correlations in the PL emission of single nanostructures.

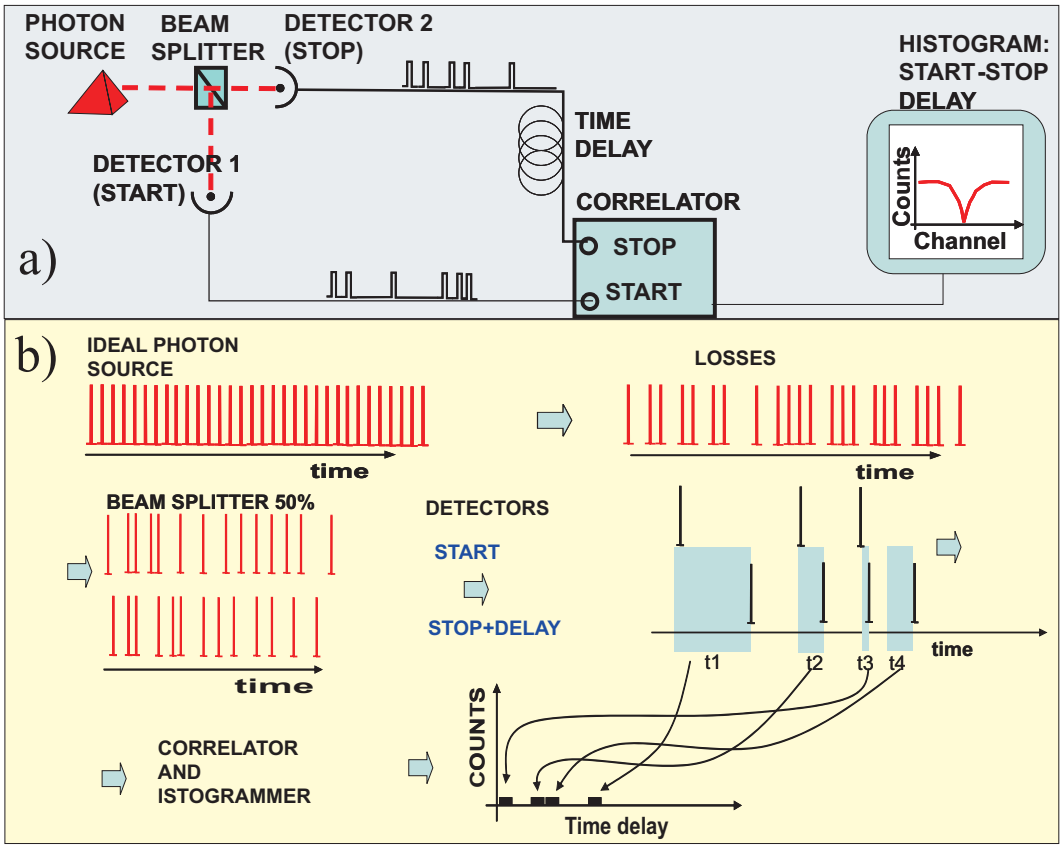

Figure 2.5: In the top panel (a) is represented the conceptual scheme of an HBT setup. The collected light emitted by a photon source is fed into the interferometer which is composed by two identical single photon detectors acting as *START* and *STOP* events. The measured time delay between a *START* and a *STOP* is processed and reported as an histogram. In panel (b) the histogram of the photon arrival statistics is schematically described. After the collection and detection of a *START*-*STOP* event the time delay is measured and converted by an ADC in a channel number. The histogram of the *START*-*STOP* events consists in the statistical distribution of the time delays of the emitted photons.

For a detailed discussion on the theory of the $g^{(2)}$ we remind to the literature [27] and in the appropriate appendix 8. Here we limit the discussion to the description of the experimental apparatus.

The simplified scheme of this setup is shown in panel a) of Fig. 2.5. The *PL* radiation is collected by the confocal microscope. The collected light is collimated at the output of the optical fiber and sent to a 50% beam splitter. The two beams are fed into two low resolution spectroscopic apparatuses as described before (the two arms of the *HBT* interferometer). The spectral filtering, acted by the spectrometer exit slits, allows to isolate the contribution of a single line in the spectrum and consequently to register the photon arrival through the avalanche photodiode (this is possible both in CW or pulsed excitation). In Fig. 2.5 the two arms of the interferometer are represented by the two detectors 1 and 2. The two APD produces logic pulses transmitted to the fast electronic for the elaboration. Through the same apparatus for $TCSPC$, represented by the correlator in Fig. 2.5, is possible to measure the time delay between the arrival of one photon on detector 1 and the following photon on detector 2 (the time delay between two APD logic pulses). Note that in the *STOP* arm of the interferometer a time delay is introduced by an electric cable. The histogram builded reporting the *START-STOP* event time distribution is proportional to the $g^{(2)}$ function [27, 70]. In the panel (b) of Fig.2.5 is schematically shown how the histogram is builded.

Chapter 3

Continuous wave excitation of quantum dot photoluminescence: line broadening and dephasing mechanisms

In the following section the main features that typically characterize the single QDs spectra are presented. In the first part the different excitonic recombination components, such as neutral exciton (X), charged exciton (T), neutral bi-exciton (XX) and multi-exciton (MX) lines are studied by changing the excitation laser power density. The analysis concerning the line shape and broadening is divided into two parts: firstly the quantum confined Stark shift induced by charged trap defects (studied by high resolution-low temperature measurements) and secondly the effect of phonon interaction on the line shape (analyzed by temperature resolved measurements).

3.1 Exciton complexes is *GaAs/AlGaAs* quantum dots

We will start presenting CW measurements performed on a single $GaAs/AlGaAs$ quantum dot as a function of the excitation power by using the micro–photoluminescence (μPL) setup previously described in 2.2.

This QDs sample presents a relatively low nanostructures density ($\sim 10^9 QDs \cdot cm^{-2}$) and a broad size dispersion. More details on the growth procedure and annealing effects can be found in Refs. [55, 36, 71] and [59]. μPL experiments were performed using a 100× (50×), high numerical aperture NA = 0.7 (NA = 0.4) microscopy objective and a single mode optical fiber acting as confocal pinhole, leading to a lateral resolution of ∼0.5 μm (∼1 μm). The sample was cooled down at T=10 K in a cold finger cryostat. With a 1 m (0.5 m) focal length double (single) grating monochromator, we could reach a spectral resolution better than 25 μeV (200 μeV). The excitation is provided by the second harmonic of a $Nd:YAG$ laser emitting at a wavelength of 532 nm, to excite the continuum states of the $AlGaAs$ barrier.

Typical PL spectra of a single $GaAs$ QD are shown in Fig. 3.1(a) and (c). In the low excitation regime the spectrum shows a single sharp (graph (a)) line labeled as X and eventually a lower energy peak T (graph (c)). In this excitation condition we can expect the formation of an $e-h$ pair in the quantum dot and interpret this line as the radiative recombination from a neutral exciton. Nevertheless it is well known that charged complexes can be obtained as a drawback of the growth (as spurious donors and acceptors dopant atoms) or as a consequence of extrinsic charges capture. In a higher excitation regime another line labeled XX emerges on the low energy side of the spectrum. A further increase in the pumping power causes the appearance of several additional lines and broad bands (MX) along

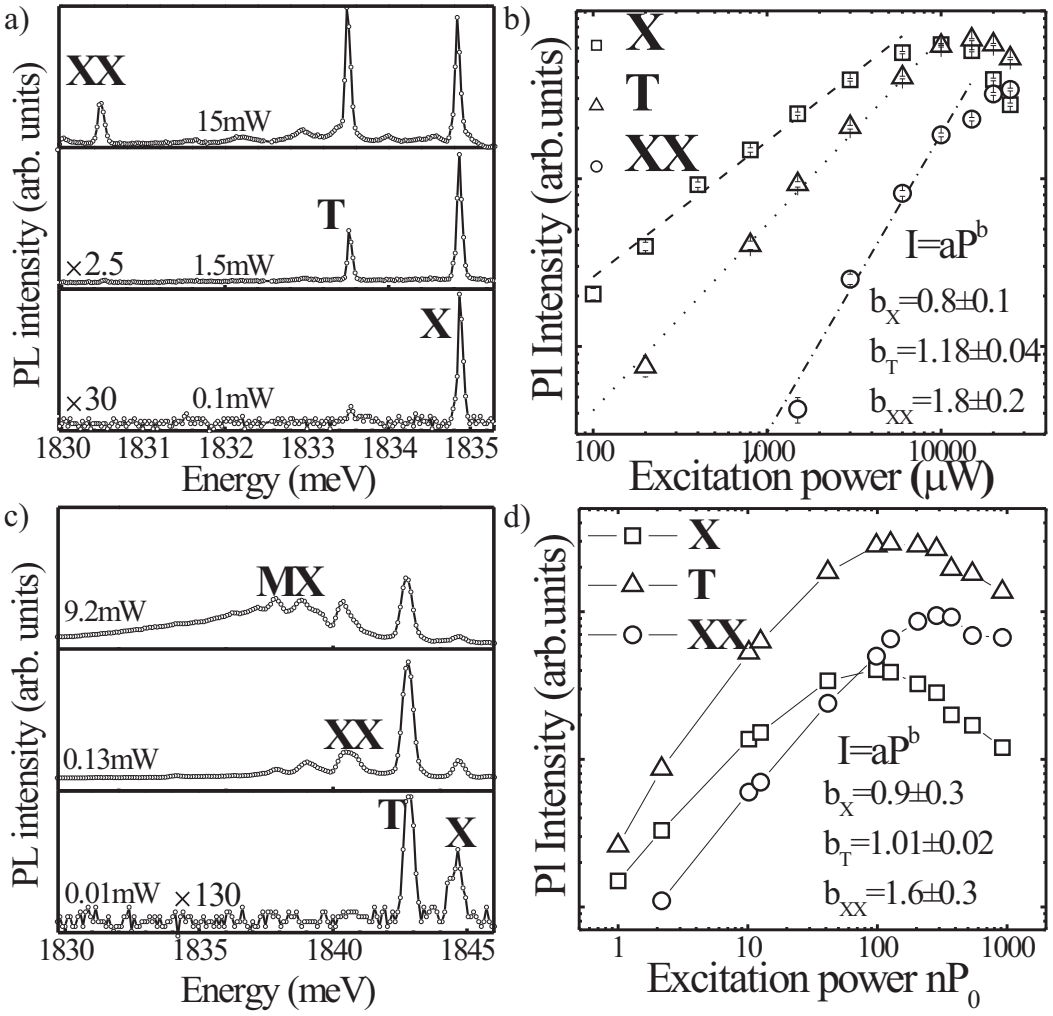

Figure 3.1: (a) high resolution spectra of a *GaAs/AlGaAs* QD for increasing power. (b) integrated PL intensity of X, T and XX lines of the QD of (a) as a function of the incident power. The power law which rules the intensity growth and the specific parameters are reported in the figure. (c) low resolution spectrum of a different QD. In this case, for high excitation, the multiexciton components MX are indicated in the low energy side of the spectrum. (d) same analysis made in (c) but for QD represented in (c). It is evident how each line progressively increases its intensity, reaching a maximum and then starting to quench.

with the quenching of X, T and XX lines (see graph (c)) [40].

The power dependence of lines X, T and XX peaks is presented in Fig. 3.1(b) and (d): for each line the intensity increases with power until a maximum and then starts to quench. Note that the X and T lines reach their maximum at smaller power density with respect to the XX. A fit to a power law of the experimental data at low P, where the saturation effect are negligible, indicates a superlinear behavior for both T and XX respect to the X case; note that XX increases almost quadratically with respect to X. Similar spectral features have been frequently observed in our *GaAs QD*s [57]. We interpret the lines X, T and XX as the neutral exciton, the charged exciton (or trion) and the biexciton radiative recombination, respectively. This attribution has been confirmed by other kind of investigations as discussed in Chap. 6). This interpretation qualitatively accounts for the saturation effect observed in the high excitation regime [40, 72]. In the low pumping regime only one exciton can be formed. In the first stages the X line linearly increases its intensity with power P. The saturation effect, as a consequence of the increasing P, results in a reduced probability to find only one exciton in the quantum dot determining a smaller intensity of the corresponding X line. On the other side the probability to create more than one exciton augments and several other lines can be observed in the spectrum. These lines are attributed to the radiative recombination of excitonic complexes such as XX and MX. Finally, for very high excitation, all the sharp lines quenche and a broad band dominates the spectrum. We measured several *QD*s emitting at different energies finding a binding energy for XX and T usually varying in the 3–5 meV and 0.7–2 meV intervals, respectively. The line broadening, reflecting spectral diffusion due to the presence of charged defects in the *QD* environment, is widely discussed in the specific section 3.2.

In all the following chapters we will refer to neutral exciton, trion and neutral biexciton using the aforementioned notation X, T and XX, respectively.

3.2 Quantum confined Stark shift: spectral diffusion

We experimentally and theoretically investigate the photoluminescence broadening of different excitonic complexes in single self-assembled $GaAs/AlGaAs$ quantum dots. We demonstrate that the excitonic fine-structure splitting leads to a sizeable line broadening whenever the detection is not resolved in polarization. The residual broadening in polarized measurements is systematically larger for the exciton with respect to both the trion and the biexciton recombination. The experimental data agree with calculations of the quantum confined Stark effect induced by charge defects in the QD environment, denoting the role of the QD spectator carrier rearrangement in reducing the perturbation of the fluctuating environment.

A typical evidence of the QD environment fluctuations is the inhomogeneous broadening of the photoluminescence (PL) lines of a *single QD*. It is well established that the radiative linewidth of the fundamental excitonic transition in single self assembled QDs is of a few μeV at cryogenic temperature, while in micro-PL (μPL) experiments values up to hundreds of μeV are observed. The origin of the broadening is known as *spectral diffusion* (SD) and is commonly attributed to the charging and discharging of trap defects on time scales shorter than the long integration time required for a μPL measurement, which results in a time-fluctuating quantum-confined Stark effect [73, 74, 75, 76]. Moreover, in presence of SD, one can observe conterintuitive effects, such as the onset of a motional-narrowing regime at low temperature and excitation power [77].

Most experimental studies addressing spectral broadening are performed with unpolarized light. However, in self-assembled QDs excitonic emission typically shows a fine structure splitting (FSS)[78, 41, 79] (see 5.2 for details on the fine structure splitting), coming from partial polarization anisotropy. Since the split-

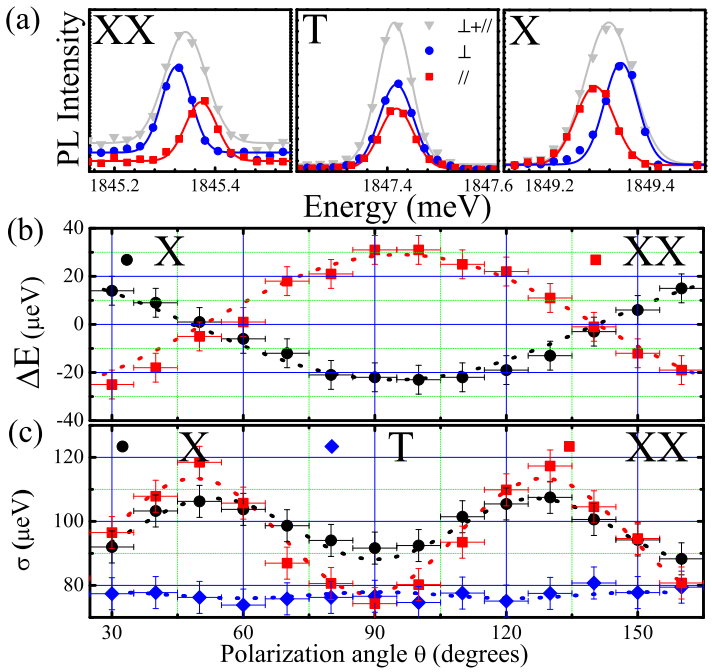

Figure 3.2: (a) PL lines arising from the X, T and XX recombination. Red squares (blue circles) represent the linearly-polarized PL emission along the $[110]$ ($[1\bar{1}0]$), gray triangles represent the sum of the two. Symbols: experimental data. Lines: gaussian fit. (b) Black circles and red squares give the positions of the X and XX peaks as a function of the linear polarization. Dotted lines: the sinusoidal fit of the data. (c) Black circles, blue diamonds and red squares are the line broadenings σ_{X}, σ_{T}, and σ_{XX}. Dotted lines: sinusoidal fit of the data.

ting ($\sim$100 μeV) is typically comparable to the line broadening , *the intrinsic SD contribution to the linewidth of excitonic recombination can only be isolated with polarization-sensitive detection.*

Here high-resolution, polarization-resolved spectroscopy is employed to characterize the excitons (X), biexcitons (XX), and trions (T) linewidth of *GaAs/AlGaAs QDs* [55, 36]. Their respective linewidths (reported as full width at half maximum), σ_{X}, σ_{XX}, and σ_{T}, show a systematic relationship, with σ_{X} typically larger than σ_{XX},

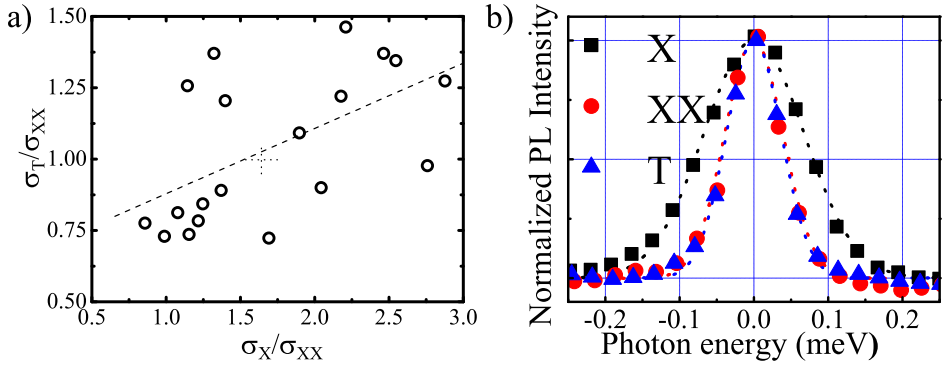

Figure 3.3: Distribution of the ratios σ_T/σ_{XX} as a function of σ_X/σ_{XX}. The dashed line is a linear fit of the points and the cross represents the averaged value. Inset: comparison between typical X (black squares), T (blue triangles) and XX (red circles) lines. The peaks are shifted in frequency and renormalized in intensity in order to make the comparison clearer.

and $\sigma_{XX} \simeq \sigma_T$.

All the measurement are performed at T=20 K by using the same confocal setup for the PL collection and a spectral resolution better than 25 μeV [see the devoted section 2.2.1]; it allows to measure line shift as small as 5 μeV. The polarization-dependent FSS is measured by using a linear polarizer and a rotating half-wave plate (see Fig. 2.4).

The QD PL spectra are generally characterized by the presence of three main peaks, which are associated to X, T and XX recombinations, on the ground of intensity-correlation measurements (see Section 6 and ref. [38]) and of the FSS analysis. We attribute T to positively charged trions (X^+) due to the slight residual p-doping of the structure. Three typical emission lines are shown in Fig. 3.2(a). The PL linearly polarized along the asymmetry axis of the QDs is denoted by the symbol $\perp$ (blue circles) and $\parallel$ (red squares) while the sum of the two as $\perp + \parallel$ (gray

triangles). The X and XX lines clearly show symmetric polarization splittings, while the T emission is polarization independent.

It is clear from Fig. 3.2(a) that the broadening of the total PL ($\perp + \parallel$) of X and XX lines is almost twice than that observed when selecting the polarization along one of the asymmetry axes. In order to precisely evaluate this effect, we have studied the FSS of X, T and XX as a function of the polarization angle. As expected, the linewidths of XX and X show a clear sinusoidal dependence on the polarization angle (θ), with a periodicity which is twice that of the corresponding FSS. This demonstrates that, besides SD, the presence of FSS in the excitonic emission gives rise to a sizeable broadening of the unpolarized QD emission spectra. In the following we analyze the linewidth corresponding to linear polarization along one of the asymmetry axes of the QD which corresponds to the smaller line broadening.

We have measured several QDs, emitting at different energies in the spectral interval $1.7 - 1.9\,\mathrm{eV}$. We find no correlation between linewidth and dot size (*i.e.*, the emission energy), which suggests the extrinsic origin of the line broadening. Analyzing each QD, we find instead a clear correlation between the line broadening and the number of carriers in the dot [see Fig. 3.3 (a)]. In particular, we find that σ_{X} is systematically larger than σ_{XX}, σ_{T}, which are instead very similar to each other: $\sigma_{\mathrm{X}} > \sigma_{\mathrm{T}} \simeq \sigma_{\mathrm{XX}}$. A typical example is shown in Fig. 3.3 (b), where the three lines are shifted in frequency and renormalized in intensity so as to allow a direct comparison of their broadenings. The average values of the broadening are $\overline{\sigma}_{\mathrm{X}} = 140\,\mu\mathrm{eV}$, $\overline{\sigma}_{\mathrm{T}} = 92\,\mu\mathrm{eV}$, and $\overline{\sigma}_{\mathrm{XX}} = 87\,\mu\mathrm{eV}$. According to previous findings [73, 74, 75, 76] we attribute the PL line broadening to SD related to the population of extrinsic levels in the barrier region around the QDs, likely associated to crystalline defects.

The presented phenomenology can be nicely accounted by theoretical models

developed by F. Troiani (University of Modena, Italy). In order to understand the observed correlation between the σ values, we calculate the X, XX, and T energy shifts induced by charged traps in the surroundings of the dot. For a given trap position, we first calculate the single-particle states by solving the three-dimensional Schrödinger equation within a single-band effective mass approximation. In our model, the confinement potential $V_{BO}^{(\chi)}(\mathbf{r})$ [$\chi = e, h$ identifies the electron (e) and hole (h) states in the QD] is provided by the band offset between the disk-shaped $GaAs$ region and a surrounding $Al_{0.3}Ga_{0.7}As$ barrier: $V_{BO}^{(\chi)}(\rho, z) = 0$ for $0 < \rho < r$ and $0 < |z| < h/2$, and $V_{BO}^{(\chi)}(\rho, z) = V_0^{(\chi)} > 0$ elsewhere. The presence of a trapped charge in the surroundings of the dot results in an additional contribution to the potential $V^{(\chi)}(\mathbf{r}) = V_{BO}^{(\chi)}(\mathbf{r}) + q/\epsilon|\mathbf{r} - \mathbf{R}|$, ϵ being the bulk dielectric constant. We then compute the energy of X, XX and positively or negatively charged trions, $T{=}X^{\pm}$, by diagonalizing the few-particle Hamiltonian $H = \sum_{\chi} H_{SP}^{(\chi)} + \sum_{\chi,\chi'} H_C^{(\chi\chi')}$, where $H_{SP}^{(\chi)}$ and $H_C^{(\chi\chi')}$ are the single-particle and (intradot) Coulomb interaction terms, respectively [80]. Finally, we identify the optical transitions between the $i-$th eigenstate $|\Psi_i^{\alpha}\rangle$ of the electron-hole complex $\alpha = X, X^+, X^-, XX$ and the $j-$th eigenstate $|\Psi_j^{\beta}\rangle$ of $\beta(\alpha) = vac, h, e, X$, respectively. In the following, we focus on transitions between ground states ($i = j = 0$), whose transition energy is ϵ^{α}. The quantity to be compared with the inhomogeneous broadening σ is the shift of the optical transitions induced by a charge q trapped at different positions $\mathbf{R}$ from the QD. These are given by the difference between the Stark shifts of the initial and final states $\Delta\epsilon^{\alpha}(\mathbf{R}) = \Delta E_0^{\alpha}(\mathbf{R}) - \Delta E_0^{\beta(\alpha)}(\mathbf{R})$. Assuming traps occupied by single carrier, we have calculated the spectral shifts for four possible scenarios, with positive/negative charge $q = \pm|e|$, and traps localized in the plane of the QD or along the growth direction.

The results are shown in Fig. 3.6 for a disk-shaped model QD, with dimensions and interlevel spacings corresponding to a typical observed dot (see caption).

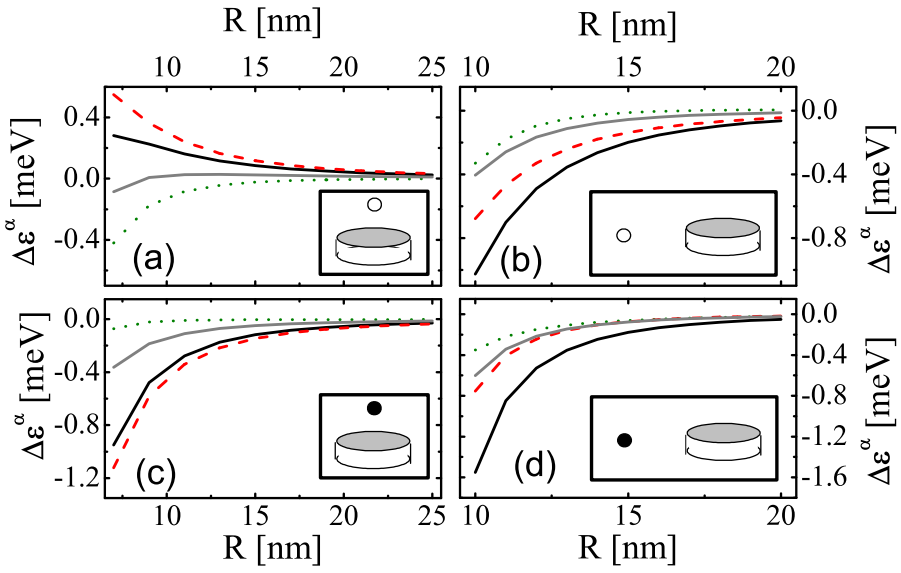

Figure 3.4: Calculated energy shift of the optical transitions of X, XX, and T=$X^{\pm}$ of a model QD, resulting from the presence of holes [$q = +|e|$, panels (a,b)] or electrons [$q = -|e|$, (c,d)] trapped in its surroundings. The dot height and radius are given by $r = 5\,$nm and $h = 8\,$nm. The trapped carrier is positioned at a distance **R** from the disk center, either along its symmetry axis [$\mathbf{R} \parallel \hat{z}$, panels (a,c)] or in the plane [$\mathbf{R} \perp \hat{z}$, panels (b,d)], as indicated in the insets. The initial electron-hole complex α corresponds to: X (solid black lines), X^+ (dotted green), X^- (dashed red), and XX (solid gray).

Quite remarkably, different charge sign and positions of the traps give rise to qualitatively different behaviors, which are found to be rather robust with respect to the QD shape and size (not shown here). Quite generally, the QD shifts corresponding to $\mathbf{R} \perp \hat{z}$ are larger than those for $\mathbf{R} \parallel \hat{z}$, for the in-plane confinement is here weaker that the one in the growth direction. The generally obtained negative shifts of the optical transition correspond to the electron-hole complexes α being more redshifted (less blueshifted) than the corresponding β. More specifically, we find that the ratios $\Delta\epsilon^{\alpha}/\Delta\epsilon^{\alpha'}$ are incompatible with the observed ratios between the corresponding broadenings, $\sigma_{\alpha}/\sigma_{\alpha'}$, if the trapped carriers are holes localized

on top of the dot [panel (a)]. Qualitative agreement between theory and experiment is found for panels b), c) and d). In particular, the calculated ratios are in good agreement with the average ratios when the quantum confined Stark shift is induced by electrons in the plane [panel (d)]. We finally note that the dependence of the shifts $\Delta\epsilon_i^{\alpha}$ on the field induced by the trap is cubic for all the considered optical transitions from trion states, $\Delta\epsilon^{X^{\pm}}$.

Therefore appears that the SD-induced broadening we measured on different single QDs originates, as theoretically supported, by traps located nearby the dot. We find systematic relationships of the line broadening, with the X linewidth typically larger than the XX and T linewidths, reflecting the different degree of polarizability of X, XX, and T states. Theoretical investigation shows that the spectral shift of the different excitonic complexes are specific of the sign/localization of the traps. Therefore, the SD-induced linewidth of μPL contains detailed information on the nature and localization of the traps.

3.3 Exciton phonon interaction

Here we present a detailed study of the temperature dependence of the single quantum dot emission lineshape. In particular, we analyze the emission lineshape in terms of linewidth, peak energy and sidebands. These quantities are all connected with the nature of the electron-phonon interaction. We conclude that the line broadening in quantum dots is due to pure dephasing processes driven by $GaAs - LO$ phonons. In addition, there is a lack of quantum size effect on the excitonic energy renormalization with the temperature.

The electron-phonon interaction in quantum dots (QDs) manifests itself in the thermal homogeneous broadening and in the temperature variation of the excitonic transition energy. Despite intense research there are still important open points in

these topics: on one side the QD transition energy shrinking is not well understood, also because it has been mainly studied on large QD ensembles [81, 82, 83]. On the other side, the thermal homogeneous broadening has been so far attributed either to scattering with bulk–localized alloy LO phonons or to promotion of excitons into higher lying energy states [84, 85, 86, 87, 88]. Moreover the majority of the studies of QD dephasing has been performed in $In(Ga)As/GaAs$ Stranski-Krastanow (SK) QDs, where the possible relevance of the strain may obscure pure electron-phonon interaction.

We performed PL experiments on our $GaAs/AlGaAs$ QD sample and in this paragraph an analysis of emission spectra as function of temperature is shown to get insight in the nature of the electron–phonon interaction.

We performed temperature-dependent photoluminescence measurements for several single QDs under nonresonant excitation in the $AlGaAs$ barrier.

In Fig.3.5 the μPL spectra of a QD is reported at different temperatures. The narrow line clearly visible in the low temperature spectra is attributed to the zero phonon line (ZPL) emission from the QDs. As the temperature increases, the ZPL emission shifts to low energy and quenches. We compensated the thermal quenching by increasing the excitation power density, thus working at nearly constant emission intensity. We always checked that the increase of the excitation power density did not affect the PL line shape. Up to 65 K, the PL band consists in a single line, which broadens with the temperature. Around 65 K prominent and slightly asymmetric sidebands appears and their relative intensity increases with the temperature. Finally, above 100 K, the QD emission is dominated by the sideband contribution. Similar results have been found in QDs of different size and we found that the relevance of the sideband contributions increases with decreasing the QD size. The analysis of the sidebands contribution will be discussed in Section 3.3. Here we concentrate on the ZPL.

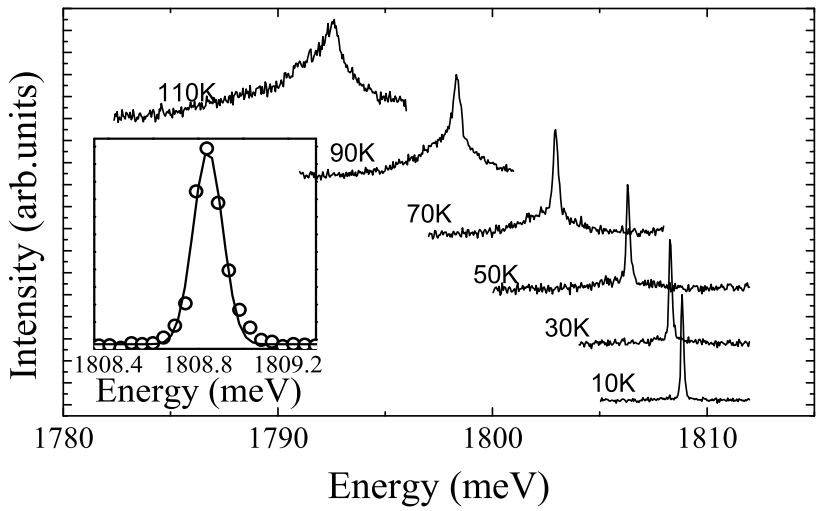

Figure 3.5: μPL spectra at different temperatures of QDA. In the inset the PL spectrum at T=10 K is shown within its Gaussian fit

The independent-boson model reproduces the broadening of the ZPL only by means of a phenomenological decay rate [84], even if a solution of this problem has been recently proposed by including a quadratic electron-phonon coupling [89]. The analysis of the broadening and of the peak position of the ZPL is therefore of the utmost interest. We have used a thermally activated fit [84] and the results shows that the activation energy is 34±2 meV, independently of different size, in good agreement with the $GaAs$ LO phonon. Our results support the interpretation of exciton decoherence as due to pure dephasing with the activation of elastic scattering of carriers into virtual states by phonons [89]. The temperature dependence of the emission energy and the lorentzian broadening γ of the ZPL for three measured QDs (QDA, QDB and QDC) is reported in Fig.3.6 (a) and (b) , respectively. Strikingly, the data of the three QDs agree within the experimental errors. For the sake of comparison, in the same figure are also reported

the original data of a high precision experimental study on the thermal shrinkage of the bulk $GaAs$ gap; all the data show the same trend. We must conclude that no quantum size effect is observed. Recently the T dependence of the excitonic emission in $InGaAs/GaAs$ $SK-QD$s has been reported [83]. Small deviations of peak position of the ZPL from the band gap shrinkage of the nominal $InGaAs$ bulk material have been observed and attributed to the different coupling of QDs with long wavelength phonons. In our samples, despite the accuracy of both the QDs and $GaAs$ bulk data, we cannot observe such deviations. We guess that the discrepancies found in Ref. [83] have to be attributed to strain-related phenomena in $SK-QD$s. It is important to note that, $GaAs/Al_{0.3}Ga_{0.7}As$ $MDE-QD$s

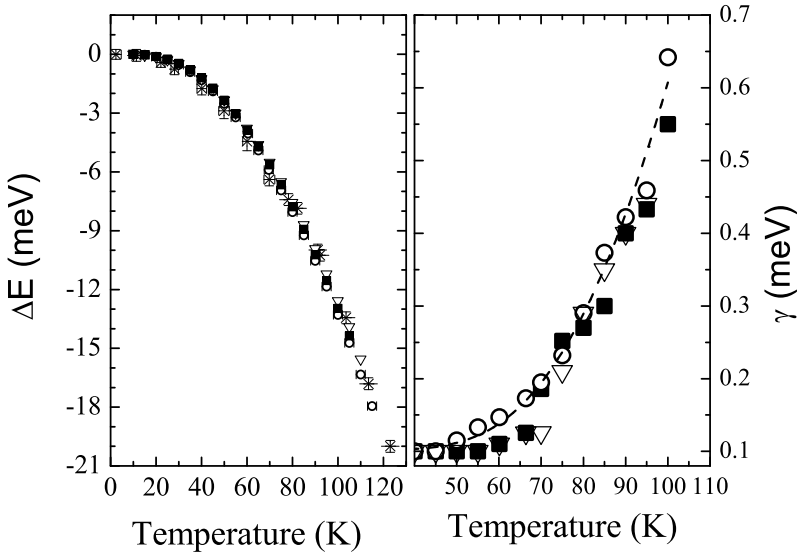

Figure 3.6: (a) Temperature dependence of the ZPL energy of QDA (diamonds), QDB (stars), and QDC (triangles). The bulk $GaAs$ gap (circles) is also reported for comparison. (b) temperature dependence of the ZPL Lorentzian broadening of QDA (circles), QDB (squares) and QDC(triangles) together with the fit (dashed line) obtained by using a phenomenological phonon activated broadening

give us some main advantages with respect to the $In(Ga)As/GaAs\ SK-QD$s. Firstly, the MDE possibility to tune and control the QD density allows for samples with low QD density but large size dispersion, therefore the selection of individual QDs with strongly different sizes is possible within a single sample. Secondly, the $GaAs/AlGaAs\ QD$s can be considered almost strain-free in all the investigated temperature range due to the negligible lattice and thermal expansion mismatch between the barrier and the QD. Finally, the composition of the QD is known, while segregation effects play a major role in determining the In content of the $In(Ga)As\ QD$. We conclude that 1) effects of pure dephasing induced by carrier-acoustic phonon elastic interaction dominate the QD emission linewidth and 2) the excitonic energy renormalization with the temperature is not strongly affected by electron confinement.

Chapter 4

Time resolved measurements on single quantum dots

In the following chapter the major results of time resolved measurements on GaAs/AlGaAs *quantum dots are presented. In the first part we concentrated on the study of the recombination dynamics of the three main photoluminescence lines X, T and XX. Further the polaronic effect and its influence on the exciton lineshape is studied in detail. Finally, in the second part, by studying the exciton lifetime, we are able to extract information about the quantum size effect on the recombination mechanism at low temperature.*

4.1 Exciton dynamic

In this section the time resolved investigation of a *GaAs/AlGaAs QD* is presented. This analysis confirms a cascade-type relaxation of multiexcitons [57, 72, 90] in agreement with the previous attribution shown in 3.1.

For excitation, second-harmonic output of an optical parametric oscillator pumped by a mode-locked Ti-sapphire laser was employed. The laser produced picosecond pulses of 550 nm in wavelength and 76.0 MHz in repetition rate. A confocal microPL setup with an objective lens of 0.42 numerical aperture was used to capture individual QDs (see Section 2.2.1). The photoluminescence (PL) was dispersed by grating monochromator equipped with a silicon based avalanche photodiode. In this setup electric pulses from the APD and the laser trigger were sent to a time-correlated coincidence counter (PicoQuant PicoHarp300). PL spectra were characterized using a cooled charge-coupled-device. All experiments were performed at 6K.

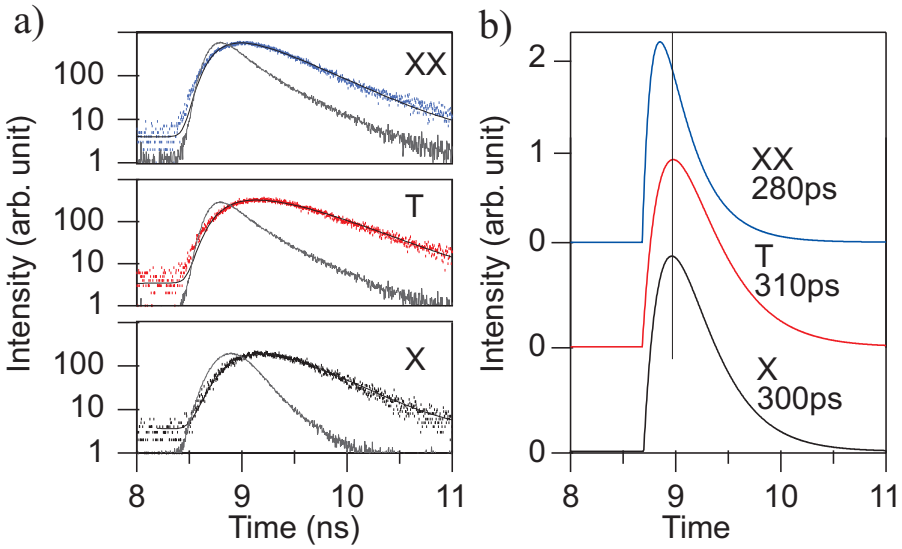

Figure 4.1: (a) Comparison between the instrumental response functions (gray lines) and time-resolved measurement of lines X, T, and XX (dot). The solid lines show fits to the convolution of IRF and growing exponential functions. All signals are observed at 10 W/cm2. (b) Results of deconvolution for the emission decays of lines X, T, and XX.

To confirm the above assignment of recombination from neutral exciton X, charged exciton T and neutral biexciton XX we took time-resolved measurements

of the three emission peaks. Time development of the X, T, and XX emission is shown in Fig. 4.1(a), together with instrumental response functions ($IRFs$) for the used APD [see Fig.6.2 for the time integrated PL spectra of the QD under analysis]. The IRF, is measured by the time response of the elastic diffusion of lase light, after adjusting the laser wavelength and the count rate of APD to be similar to those of PL. We fit the temporal data to a convolution of IRF and the difference of two exponential decays function, in order to reproduce the PL rise and decay times.The result of this analysis gives $\tau_X = 300(\pm 20)$ps and shows good agreement with the data. This decay time is equivalent to the value determined by time-resolved measurement using a detector with better resolution (see Section 4.3). Following the same procedure, we could reproduce the deconvoluted responses of the X, T, and XX emissions, as shown in 4.1(b). We found that the curve for X showed almost the same time evolution of the curve for T ($\tau_T = 310(\pm 20)$ps), while the curve for XX showed shorter decay ($\tau_{XX} = 280(\pm 20)$ps) and rise times. Besides, the deconvolution in 4.1(b) points out a significant time delay of the X and T emission respect to the XX, as evidenced by the vertical line. These are signatures for the biexciton cascade relaxation: Peak XX appears and decays in the initial stage of the emission, then peak X appears and eventually decays [57].

4.2 Phonon sidebands and polaron dynamic: lifetime investigation

More insights concerning the exciton–phonon interaction can be obtained by time resolved PL experiments to investigate if the recombination dynamics has a common origin or not. Our results validate the interpretation of the broad pedestal band appearing when increasing the temperature as originated from phonon replica. Moreover we find that the relative weight of the phonon replicas depends both on

temperature and on the QD size in agreement with theoretical predictions.

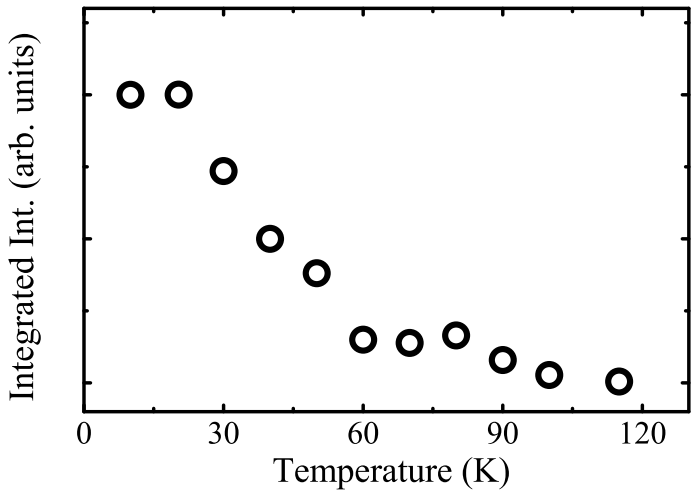

Figure 4.2: Integrated intensity, in a semi-logarithmic scale and normalized at T=10 K, of the single QD band as a function of the temperature.

The influence of the nanostructures environment which strongly interacts with the carriers localized in the QDs, is known to be at the basis of efficient dephasing mechanisms [84, 87, 91, 92, 93]. In particular, the emission of single electron-hole pair from individual QD is strongly influenced by the external environment showing a composite lineshape: a sharp line plus pronounced and asymmetrical sidebands [84, 87], which strongly varies with increasing temperature. This feature has been interpreted in terms of electron-acoustic phonon interaction (see Section 3.3).

Previously we have investigated the sharp component of the single QD emission assigned to the zero phonon line (ZPL), while the sidebands are commonly attributed to a superposition of acoustic phonon replicas in the framework of the Huang-Rhys formalism [87, 89, 94, 95, 96] (see section 3.3). Despite the relevance of the topic, this attribution has not yet been validated by complementary

experiments, such as time resolved measurements which allow to discriminate between contributions of different nature even in the case of strong spectral overlap. We have in fact already seen that the exciton, biexciton and multiexciton recombination in individual QDs under high excitation power determine an emission spectrum with sharp lines (eventually overlapped to a broad pedestal attributed to multiexciton emission). Nevertheless the cascade nature of the different contribution clearly emerges in the recombination kinetics [57]. At the same time, a well recognized fingerprint of excitonic phonon satellites can be obtained by time resolved measurements due to the common recombination kinetics of the ZPL and the associated phonon replica [97].

The experimental setup for time resolved μPL has been previously described. Her it's only worth mentioning that the excitation was provided by a ps dye-laser at 600 nm (pulse duration 5 ps, repetition rate 76 MHz). The spectral resolution was of 0.2 meV and the time resolution was 30 ps (expressed as $FWHM$ of the instrumental response).

Since we are interest in studying the exciton dynamics we choose an excitation power density low enough to avoid biexciton and multiexciton emission. In Fig. 3.5 of Section 3.3 typical μPL spectra of an individual QD are reported at different temperature. Up to 50 K, the PL band consists of a single line, which broadens with temperature. A detailed study of this emission contribution can be found in Section 3.3. For higher temperature, broad and slightly asymmetric sidebands appear and their relative intensity, with respect to the sharp central line, increases with increasing the temperature. Finally, above 100 K, the QD emission is dominated by the sideband contribution. In Fig. 4.2 (b) the QD PL integrated intensity (normalized at T=10 K) as a function of the temperature is shown, denoting a relevant emission quenching and, as described in Section 3.3 the PL lineshape strongly depends on T. From these data it emerges that the best

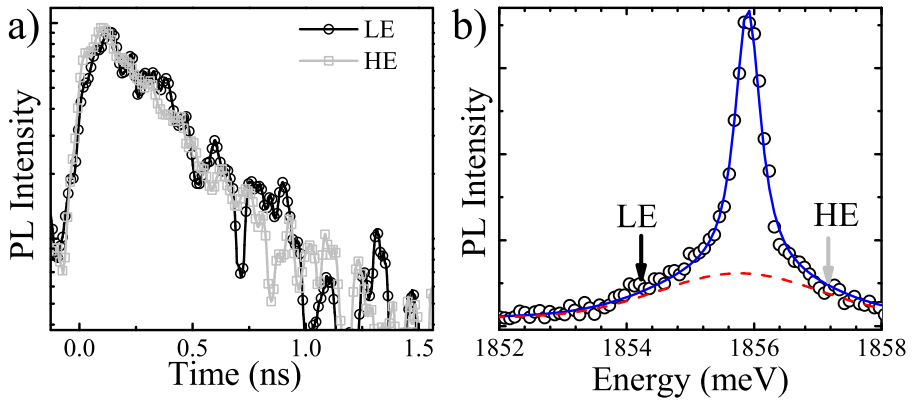

Figure 4.3: (a)Comparison of the PL decays at the low energy (LE) and high energy (HE) PL sidebands at T=70 K, in a semi-logarithmic scale. (b) PL spectrum, together with the fit (solid line) following Eq. (4.1). The dashed line is the acoustic–phonon sideband contribution to the single QD PL.

temperature for investigating the recombination kinetics of the composite PL band of the individual QDs is around 70 K, where both the narrow line and the two sidebands are clearly resolved and the PL intensity is not drastically quenched.

Let us now discuss the recombination kinetics of the individual QDs emission. The comparison between the decay time of the high and the low energy sidebands is reported in Fig.4.3 (a). Figure Fig.4.3 (b) shows the time integrated emission band with arrows indicating the detection energy in the time resolved measurements. We take advantage from the mechanical stability of our experimental setup which allows to perform time resolved experiments over many hours with non need of realignment. The decay times of the two spectral sidebands are identical within the signal fluctuations and they correspond to a monoexponential decay of ≈ 400 ps. The indistinguishable recombination kinetics of the high and low energy sidebands strongly suggests that the two spectral contributions have a common nature.

The next step is to compare the time evolution of the central narrow line with

that of the sidebands. This is shown in Fig.4.4 (a), for a slightly different QD with respect to Fig.4.3 (b). Fig.4.4 (b) reports the time integrated PL spectra with the indication of the energy at which the two time evolutions have been measured. Within the signal fluctuations, the time evolution of the two spectral contributions are identical and, in this case, they correspond to a monoexponential decay of ≈ 600 ps. It is worth stressing that the PL lifetime in this QD is significantly larger with respect to the findings of the QD reported in Fig.4.3, where the PL peak decays with the same lifetime (≈ 400 ps) of the two sidebands (not reported here). The difference in the QD lifetimes can be attributed to either a variation of the radiative or of the non radiative rate. Anyway, for our purpose, the striking point is that the PL sidebands and the PL peak have the same recombination kinetics, even if the QDs exhibit different lifetimes. As discussed above, we can conclude that the two asymmetric sidebands and the sharp central emission line have identical recombination kinetics, therefore unambiguously demonstrating a common nature. Similar results have been obtained in the quantum dots we investigated, with emission energies spanning from 1.670 eV to 1.855 eV.

Our experimental proof of the common nature for the sharp line and the broad pedestal band of individual QDs, validates the assumptions commonly made in literature: the sharp emission line is associated to the zero phonon line emission (ZPL), the high energy sideband is attributed to optical transitions assisted by phonon absorption while the low energy contribution derives from optical transitions assisted by phonon emission, thus determining their asymmetry. In this framework the sideband PL intensity depends on the thermal distribution of the phonons and therefore on the lattice temperature. However, we may expect differences in the relevance of the phonon replicas in our strain free $GaAs$ QDs, with respect to the more commonly studied cases of Stransky Krastanov $In(Ga)As$ QDs where strain and piezoelectric effects are present. It is then interesting to

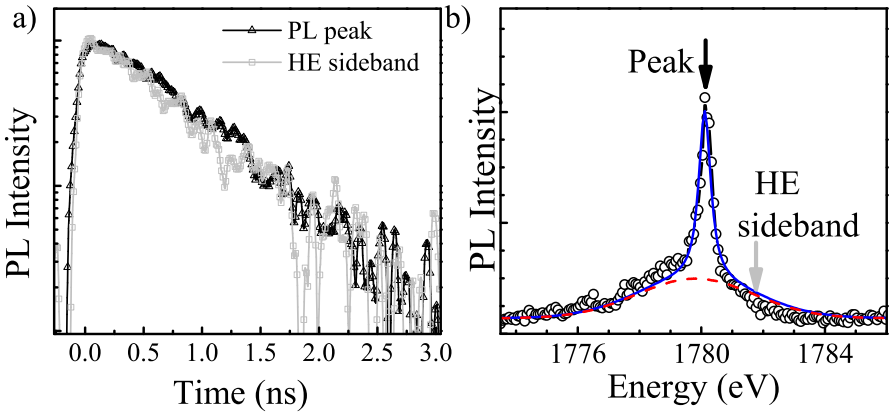

Figure 4.4: (a)Comparison of the PL decays at the central PL peak and at the high energy PL sideband for T=70 K, in a semilogarithmic scale. (b) PL spectrum together with the fit (solid line) following Eq. 4.1. The dashed line is the acoustic-phonon sideband contribution to the single QD PL.

study the temperature dependence of phonon sidebands in the $GaAs$ QDs. In order to determine the relative contributions in the PL spectrum as a function of the temperature, we use the simple fitting function proposed in Ref. [98]:

$$\begin{aligned} I(E) &= S_0|E-E_c|\exp\left(\frac{E-E_c}{\gamma_{\rm ph}}\right)^2\left(\theta(E_c-E)+\frac{1}{\exp\left(\frac{|E-E_c|}{k_BT}\right)-1}\right) \\ &+ \frac{2\ln 2}{\pi^{3/2}}\frac{\gamma_L}{\gamma_G^2}\int_{-\infty}^{\infty}\frac{\exp(-t^2)}{\left(\sqrt{\ln 2}\frac{\gamma_L}{\gamma_G}\right)^2+\left(\sqrt{4\ln 2}\frac{E-E_c}{\gamma_G}-t\right)^2}{\rm d}t, \end{aligned} \tag{4.1}$$

The ZPL, whose width is γ_L, is described by a Voigt function centered in E_c convoluted with the line broadening due to an inhomogeneous contribution γ_G, typically spectral diffusion [99]. The acoustic–phonon sideband, modeled through a weighted Gaussian with $\gamma_{\rm ph}$ width, is coupled to the ZPL through the empirical constant S_0, finally θ is the step function. This fit function gives a nice reproduction

of the single QD spectra, as shown in Fig. 4.5 (a), even if the data systematically show a more pronounced asymmetry with respect to the model. Nevertheless the quality of the fits permits the quantitative determination of the weight of the acoustic–phonon sidebands within the single QD spectrum.

The inset of Fig.4.5 reports the integrated intensity of the phonon sidebands, normalized to the total integrated intensity, as a function of T for two different QDs emitting at 1.808 eV (QDA) and 1.745 eV (QDB), respectively. In the fit ZPL broadening γ_L increases with T, as discussed in [58], the parameter $\gamma_{\rm ph}$ is 2.3 meV and 3.6 meV for QDA and QDB, respectively. It is possible to relate, by means of a simple model based on the effective mass approximation [71, 100, 101], the single QD emission energy with the QD size. In particular, QDA emission corresponds to a QD with a base size of ≈14 nm and QDB ≈20 nm [71]. Our measurements thus span a factor three in the single QD volume. As expected [87, 89, 94], we find that the relevance of the acoustic–phonon sidebands is increasing with the temperature, in agreement with the increase of the acoustic–phonon population with T. More striking it is the observation that the relative spectral weight of the acoustic sidebands shows a well defined quantum size effect: the smaller the QD, the larger the acoustic–phonon sidebands.

According to the independent-boson theory [94], the electron–phonon strength separates into two factors. The first depends on the specific electron–phonon coupling mechanism. The second, named form factor, is related to the spatial extension of the electronic wave functions and determines the extension, in the wave vector space, of the phonons involved in the dephasing mechanism. With decreasing dot size the form factor extends to higher phonon wave vector values thus increasing the relevance of the acoustic–phonon sidebands on the single QD emission spectrum. Independent-boson theory thus predicts a substantial quantum size effect, with the acoustic–phonon sidebands which decrease for increasing QD

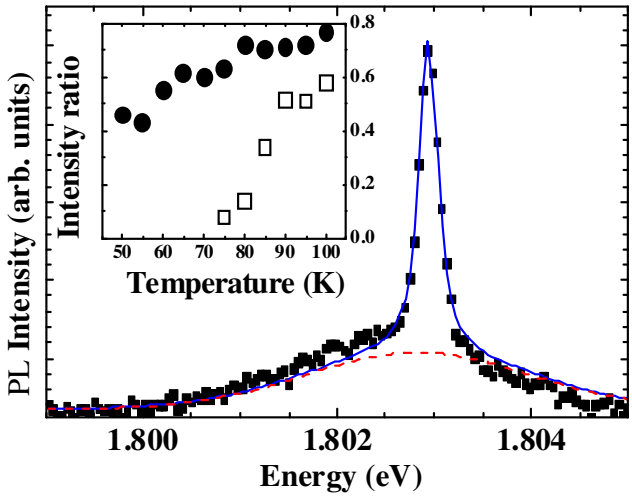

Figure 4.5: PL spectrum at T = 75 K and its fit (solid line) following Eq. (4.1). The dashed line is the acoustic–phonon sideband contribution to the single QD PL. Inset: intensity of the phonon sidebands, in a semilogarithmic scale and normalized to the total integrated intensity, as a function of T for QDA (dots) and QDB (squares).

dimensions. This prediction agrees with our experimental findings.

Therefore we have solved the question to validate or to dispute the commonly assumed attribution of acoustic phonon replica of the composite PL band from individual strain free semiconductor QDs. The different bands of the composite emission line show identical recombination dynamics, demonstrating the common origin of all contributions and according to the phonon replica assignement for the broad pedestal appearing when increasing the temperature. Finally, we show that the relative weight of the phonon replicas depends both on temperature and on the QD size, in agreement with the theoretical predictions.

4.3 Quantum size effect: exciton lifetime investigation

The broad size dispersion of MDE quantum dots within the same sample makes possible to extract size dependence of intrinsic features. With no change of extrinsic effects we performed time resolved experiments to investigate the dependence of the exciton lifetime on the QD size. We experimentally demonstrate that the exciton lifetime is reduced when decreasing the dot size. The analysis of the recombination kinetics as a function of the excitation power allows us to resolve the exciton and biexciton contribution, leading to a clear interpretation of the experimental data.

One of the key parameter in the optimization of the design of QD–based optoelectronic devices is the radiative lifetime of the electron-hole pairs inside the single nanostructure. From the theoretical point of view, a distinction has been made depending on the radius R of the QDs with respect to the exciton Bohr radius a_B [102]. In the case of no lateral confinement ($R > a_B$) the quantum well limit is expected to be found, with very short ($10 - 20$ ps) radiative lifetime of the free exciton [102]. In the intermediate case of weak confinement ($R \sim a_B$) the radiative lifetime decreases with increasing the QD size according to the so-called coherence volume effect [103]. In the strong confinement regime ($R < a_B$)) the radiative lifetime is generally expected to be independent of the QD size, due to the strong electron-hole overlap [104]. However a decrease of the radiative lifetime with decreasing the QD size has been predicted with $K \cdot P$ theory [105] and the opposite trend has been found with atomistic pseudopotential methods [106]. From the experimental side, the photoluminescence (PL) lifetimes reported in the literature for $InGaAs$ QDs show a quite large spread of values, likely due to variation of the $e - h$ overlap induced by different QD morphology and by piezoelectric effects

[107]. Moreover some experimental works have reported that the PL decay time increases with increasing the QD size [108], other experimental evidences showed that exactly the opposite occurs [109, 110].

It's worth noting that so far most of the experimental studies have been performed on Stranski Krastanov (SK) $In(Ga)As$ QDs with macroPL experiments on QDs ensembles and this raises some difficulties for the data interpretation.

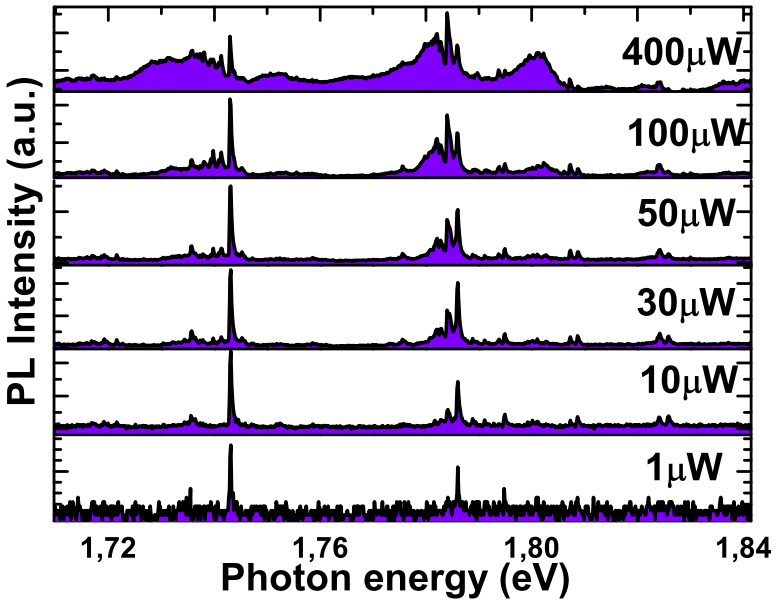

Figure 4.6: μPL spectra at different excitation power. In each spectrum the contributions of two different QDs are resolved .

Firstly, the strain induced piezoelectric field in $SK - QD$s may lead to a separation of electron-hole pairs, then producing a variation of the radiative lifetime. Secondly, measurements on ensemble QDs cannot discriminate between biexcitons, trions and p-state recombination which are expected to have very different lifetimes with respect to the fundamental $e - h$ optical transition. Thirdly, comparison between different samples have been often used to measure the lifetime dependence

on the QD size. Here we address the problem of the dependence of the radiative lifetime on the QD size in single strain-free $GaAs$ QDs, within the same sample. This allows us to exclude electron-hole separation both due to In segregation and to strain fields. Since we have measured the PL decay time of single $GaAs$ QDs by means of time resolved μPL, we rule out the possible relevance of excited state emission. The analysis of the recombination kinetics as a function of the excitation power allows us to resolve different excitonic contributions, leading to a clear interpretation of the experimental data. The broad inhomogeneous size distribution of QDs grown by droplet epitaxy is used to investigate QD of different size in a single sample, with a clear advantage of homogeneity in the possible structural disorder inside the sample.

We performed time resolved PL measurements for several single QDs under non-resonant excitation in the $AlGaAs$ barrier. The experimental apparatus was previously described in Section 3.3 and 2,

In Fig. 4.6 the μPL spectra at different excitation power are reported. At the lowest excitation power only two sharp lines are observed related to the exciton recombination (X) in the QD. They evolve in a multiplet structures when increasing the excitation power, due to charged exciton (T) biexciton (XX) and multi exciton (MX) recombinations [57]. The analysis of the recombination kinetics as a function of the excitation power allows us to resolve the exciton and biexciton contribution, leading to a clear interpretation of the experimental data (see Section 3.1). In Fig. 4.7 (a) we report the comparison between the exciton and biexciton time evolution after the pulse excitation. Clearly the XX decays faster than the X line, in agreement with recent theoretical predictions [106]. Since it is almost impossible to isolate the exciton from biexciton recombinations when performing macro-PL measurements with thousands or more QDs within the detection area, our results show that extreme care as to be used when interpreting the decay time

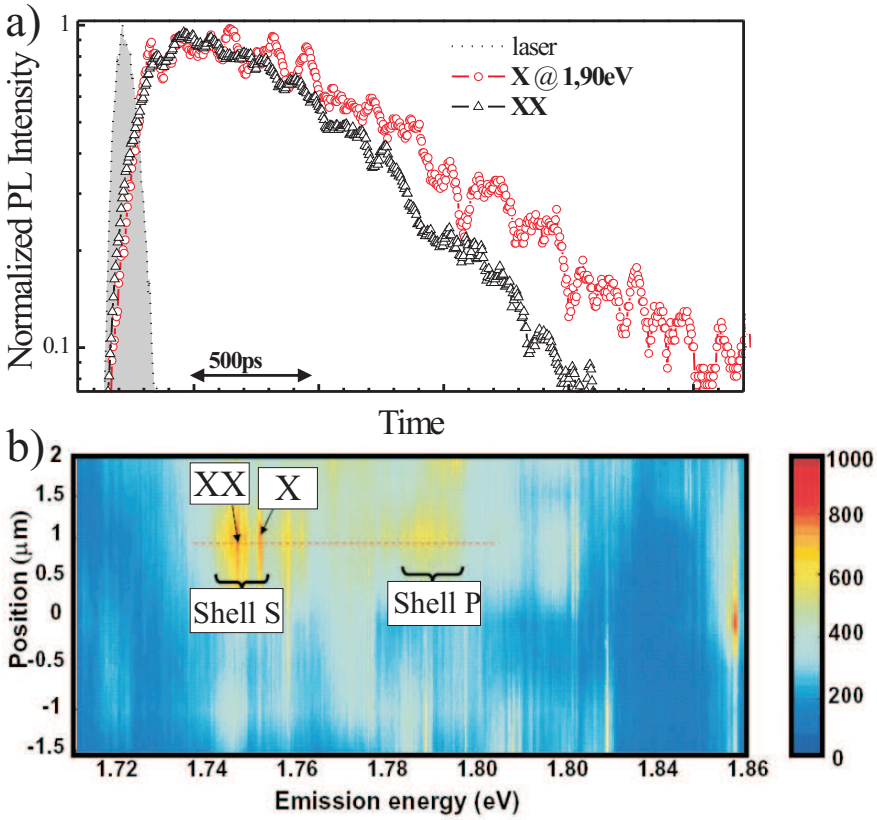

Figure 4.7: PL decay of exciton and biexciton line. b) Spatial resolved PL emission.

extracted form measurements on large ensemble of QDs. The spatial extension of each single emission line, which reflects our spatial resolution is reported in Fig. 4.7 (b). By acquiring the PL spectra through an emitting sample region we can spatially correlate different emission lines and therefore attribute them to the same or to different QDs, in the case that many emission lines are observed in the same spectral window. This is particularly important in the high energy part of the inhomogeneously broadened PL band, where the presence of recombination from higher excited states from large QDs may overlap to the fundamental excitonic recombination of small QDs. After the power dependence and spatial analysis of

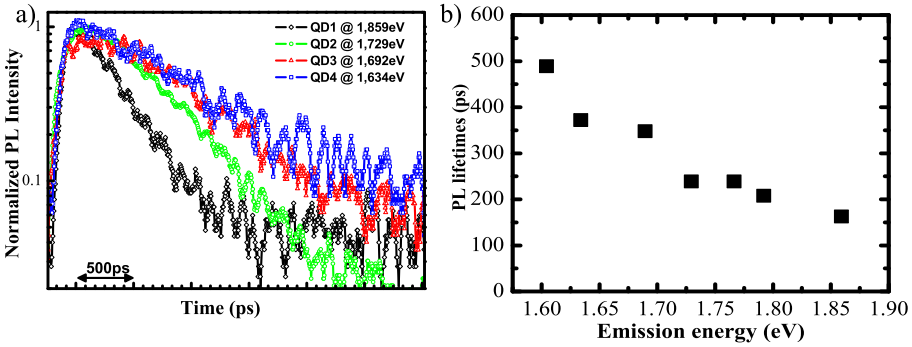

Figure 4.8: a) PL decay curves of exciton line from different QDs. b) Exciton PL lifetime as a function of the QD emission energy.

each emission line we are quite confident in attributing the fundamental excitonic emission from QDs of very different size. This is reported in Fig. 4.8 (a) where the time evolution of the excitonic PL lines for different QDs is reported. Clearly a fastening of the recombination kinetics is observed when increasing the emission energy, that is when decreasing the QDs size. The values of the decay time obtained with best fits with a monoexponential decay are reported in Fig. 4.8 (b) as a function of the QD emission energy. Note that the investigated range of QD emission energy spans over 250 meV. The QD size can be evaluated by following the results of Ref.[55], which also take care of the Ga and Al diffusion during the annealing procedure. We find that the QDs can be approximated by a cone with ratio, between height h and radius r, of $h/r \cong 1.5$. The typical dimensions of the $GaAs$ QD are ($h = 20$ nm, $r = 13$ nm) for emission at 1.6 eV and ($h = 7$ nm, $r = 5$ nm) for emission at 1.85 eV, respectively. The results of Fig.4.8 (b) shows a monotonic reduction of the PL decay time when decreasing the QD size, in agreement with previous finding by macro-PL experiments in a set of annealed

$InAs$ QDs [109] and of $InAs$ QDs grown on different misoriented subtrated [110]. Finally, it should be noted that the PL intensity of different QDs does not follow a similar monotonic reduction. This suggests that non radiative channels should play a minor role and therefore we experimentally demonstrate that the recombination lifetime of the QDs is reduced when decreasing the QD size.

Chapter 5

Polarization resolved measurements on quantum dots: spin effects

In the following chapter the main results of polarization resolved measurement on single quantum dots are presented. In the first part the magneto-optical properties are taken into account addressing intrinsic properties such as Landè g factor and diamagnetic shift coefficient γ_2. In the second part high resolution measurements provide information about the QD *symmetry and anisotropic-exchange interaction in the case of zero external magnetic field.*

5.1 Magneto photoluminescence measurements

Modified droplet epitaxy *GaAs/AlGaAs* single quantum dots have been studied by low-temperature magneto-photoluminescence spectroscopy. We observe Zeeman

splitting and diamagnetic shift of the neutral exciton line. The Landè g factor of different quantum dots has been measured in a wide range of emission energies (i.e. quantum dot size). The measured g factors and diamagnetic shifts are compared with conventional quantum dots grown by the Stranski-Krastanov (SK) method, as well as $GaAs/AlGaAs$ quantum wells and fluctuation-induced dots.

Spin properties of confined electrons and holes in quantum dots (QDs) have been the subject of many studies and single-shot readout in single electron spins has been successfully demonstrated by a conductance approach. For an optical, non-contact approach, the spin states of photocarriers are determined by analyzing the polarization of the emitted signal whose spectral lines are split by applying a magnetic field. The most important quantity ruling the charge interaction with a magnetic field is the Landè g factor. The g factors of electrons, holes, and excitons in QDs have been intensively studied in various types of bulks, quantum wells (QWs), and QDs and it turns out that g is determined by a complex interplay of the electronic level structure. As far as the QD case is concerned, the effect of size, shape and strain on the g factor has not been completely understood [111, 112] and data in the literature are scattered over a wide range of values. It should be stressed that so far most of the attention has been devoted to strained Stransky Krastanov $InGaAs/GaAs$ QDs. This has motivated our study, since the determination of g factors in strain free $GaAs/AlGaAs$ QDs is expected to be of great importance in fact, the lack of strain field, and then of piezoelectric charge distributions, excludes the presence of electron-hole separation and wavefunction distortions.

We analyzed the photoluminescence of single $GaAs/Al_{0.3}Ga_{0.7}As$ QDs as a function of a magnetic field. The magnetic field was applied along the direction normal to the sample surface and parallel to the excitation/emission beam (Faraday geometry) and tuned between 0 and 5 T. The PL was collected with a confocal microscope working with a $50\times$, $0.55NA$ microscopy objective providing a lateral

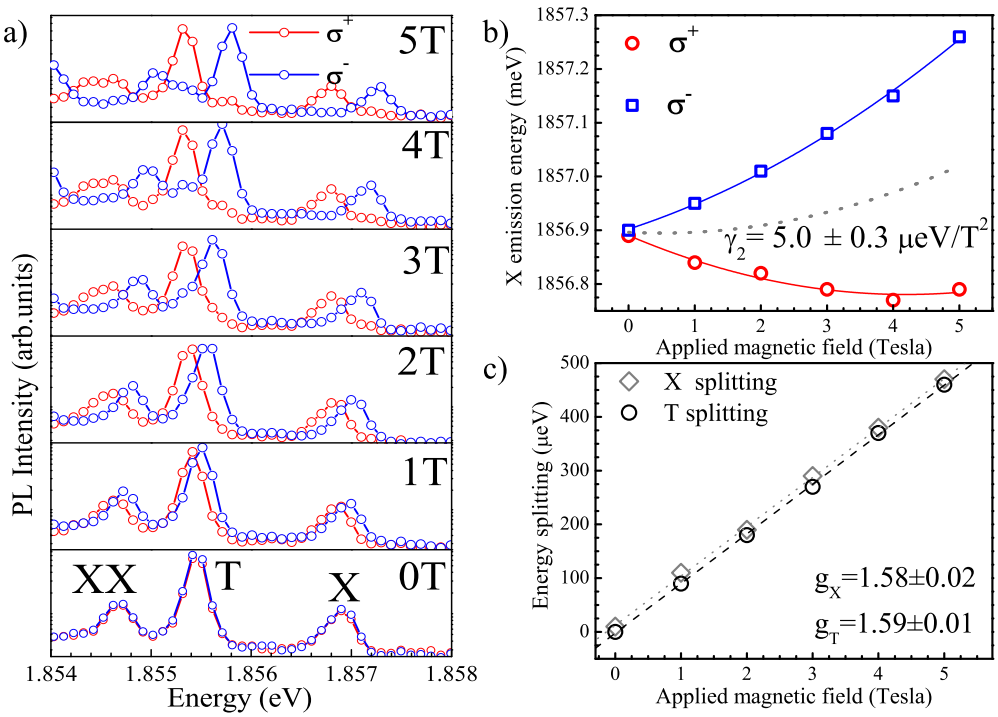

Figure 5.1: (a) Spectra of a single $GaAs/AlGaAs\ QD$ under the effect of magnetic field. (Anti)Clockwise polarization (σ^-) σ^+ is plotted with a (red) blue line. (b) X peak position for σ^- and σ^+ polarized PL as obtained from gaussian fit of the experimental data in graph a), as a function of the applied magnetic field. Continuous lines are parabolic fit to data used to determine the diamagnetic shift γ_2 which is represented as a dotted line. (c) X and T splitting (E(σ^-)-E(σ^+)) after diamagnetic shift subtraction as a function of the applied magnetic field. The dotted (dashed) line is a linear fit to the experimental data for (T) X and are used to determine the Landé g factor.

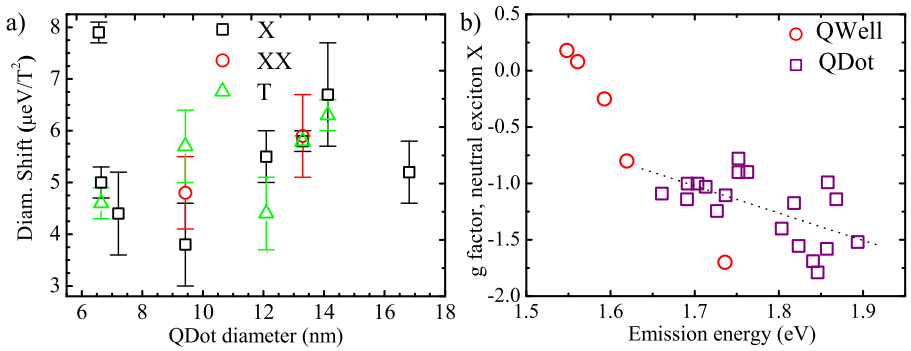

Figure 5.2: (a) X, T and XX measured diamagnetic shift γ_2 as a function of the QD diameter. (b)Emission energy dependence of g factor of *GaAs/AlGaAs* QWs (circles) of ref [113] and the measured QDs (squares). The black line is a linear fit to our data.

resolution of $\sim 1\mu$m. The μPL collected in the optical fiber was dispersed and analyzed by a single grating, 50 cm spectrometer and a cooled charge coupled device, allowing a resolution of $150\mu eV$ $(FWHM)$. By using a Glan prism and a quarter-wave plate we distinguished QD emission with σ^+ and σ^- (clockwise and anti-clockwise) polarization. The sample was cooled down to $5K$ in a cold finger, low vibration cryostat and the excitation was performed by a CW $HeNe$ laser emitting at $534nm$. The excitation power was about 20 W cm^{-2}.

An example of QD emission energy as a function of the magnetic field B is shown in the Fig. 5.1 (a). In the case of zero magnetic field we can resolve in the PL spectrum three lines arising from the same individual QD assigned to X, T and XX, as described in Section 3.1 These PL lines, at least within our experimental resolution, does not show a linearly polarized fine structure without the presence of magnetic field. When applying a magnetic field a spectral splitting arises with a (blue) red shift to (higher) lower energy of the (anti-) clockwise (σ^-) σ^+ polarized line. The field dependence of the energy peak of the main lines is well described by

the superposition of the quadratic diamagnetic shift (Fig. 5.1 b)) and the linear Zeeman splitting (Fig. 5.1 c)). The diamagnetic constant γ_2 and the g factor are obtained with parabolic and linear fit.

The diamagnetic constant γ_2 for the QD in Fig.5.1 is estimated to be 5.0 ± 0.3 μeV/T^2. The results of our measurements on several QDs are summarized in Fig.5.2 (a) where the measured diamagnetic shift γ_2 for X, T and XX are reported as a function of the QD base diameter (for the QD size determination we followed [71]). The scattered behavior of the measured data highlights the role of the disorder in the QDs environment. However the averaged value of the diamagnetic coefficient for neutral excitons is $\gamma_2 \simeq 5$ μeV/T^2. Quite remarkably this value is 5 times smaller than that reported in the $GaAs$ QDs arising from interface fluctuation in $GaAs$ quantum wells (QW) [114]. The reduction in the diamagnetic shift is likely due to the higher lateral confinement of carriers present in our self-assembled QDs. In other words we expect that the effective potential shape in fluctuation-induced $GaAs$ QDs would have a smaller aspect ratio h/d (height/diameter). The role of the aspect ratio in determining the diamagnetic shift is confirmed by previous findings in $MOCVD$-grown $InGaAs/GaAs$ systems where a diamagnetic shift of 10μeV/T^2 is found for aspect ratio of 0.35 or smaller [112, 115].

The Landè g factor is estimated by using the formula $g = |E(\sigma^+) - E(\sigma^-)|/\mu_B B$ where $E(\sigma^{+/-})$ is the emission energy of the exciton with (anti)clockwise polarized line, μ_B is the Bohr magneton and B is the applied magnetic field. For the QD of the Fig.5.1 g is estimated to be 1.58 (± 0.02), while we can find strong variations depending on QD emission energy. In Fig.5.2 (b) we report the comparison of measured g factor for $MDE\,QD$s and $GaAs$ QWs [113]. Note that we calculated the emission energies of QWs following Ref.s [116, 117]. Typical values of g for MDE QDs are about -1.2, in good agreement with the value -1.3 found for lattice-

matched fluctuation-induced $GaAs$ QDs [55]. On the contrary typical values of g in $MOCVD$ $In(Ga)As/GaAs$ QDs are between -2 and 3 [112]. Finally, despite large fluctuations of g (likely due to disorder around the MDE QDs) we observe a decreasing trend of g when increasing the emission energy. The similar trend is found in $GaAs$ QWs, as shown in Fig.5.2, while we can identify a significant discrepancy in the dependence for QDs and QWs, possibly due to the effect of heavy-hole and light hole mixing present in these QDs.

In conclusions we observed photoluminescence spectra of single self-assembled $GaAs/AlGaAs$ QDs grown by MDE, and their dependence on magnetic field. Diamagnetic coefficients were found to be 1/5 of the value reported in fluctuation induced $GaAs$ QDs, reflecting higher lateral confinement present in our QDs. The g factor has been evaluated to be -1.2 on average, which is similar to the value for $GaAs$ fluctuation induced QDs. Significant dependence of g factor on QD size was confirmed.

5.2 Fine structure splitting

Since $GaAs/Al_{0.3}Ga_{0.7}As$ quantum dot are designed and realized in order to reduce as much as possible strain and segregation they represent an ideal system to investigate fine structure splitting (FSS), avoiding all the strain-related effects present in previous experiments. Here we will show that photoluminescence from isolated quantum dots exhibits a linearly–polarized FSS. Moreover FSS clearly shows a quantum–size effect, monotonically decreasing from 90 μeV to 20 μeV with decreasing the quantum dot size (increasing emission energy). While these findings are similar to that observed in strained $In(Ga)As/GaAs$ quantum dots, clearly they require a different explanation, being our quantum dots not affected by strain–induced piezoelectricity. We ascribe the observed FSS to a size depen-

dent reduction of dot shape anisotropy as evidenced by structural data analysis. Moreover the linear polarization in dots with shape close to cylindrical symmetry is not along the [110] crystallographic axis but it results randomly distributed, highlighting the role of extrinsic effects.

From fundamental point of view QDs provide a unique system to investigate carrier–carrier interactions in precise manner. In particular, the fine structure splitting, that is the degeneracy lift of the bright excitonic states induced by asymmetries in the QD confining potential [33] holds an extremely high importance (see Section 1.2). In fact the understanding and control of FSS in QDs is a relevant issue for quantum information applications [118] because triggered polarization–entangled photon pairs could be obtained by the radiative decay of biexcitons in QDs provided that FSS is tuned to zero [18].

Since the first observation of FSS for excitons localized in three–dimensions by monolayer fluctuations in $GaAs/AlGaAs$ quantum wells [33], FSS is a common feature of the excitonic emission from epitaxially grown QDs [41, 44]. FSS shows an extremely wide range of values depending on the specific measured QD system [42], ranging from 8 μeV in $InGaAs/GaAs\ SK-QD$s [119] up to the giant value of 1 meV in $InAs/AlGaAs\ SK-QD$s [120].

The major contribution to the lifting of the bright exciton degeneracy in QDs comes from asymmetries in the QD confinement potential which induce a splitting of the exciton states via the exchange interaction [33, 121, 122]. As a matter of fact, the confinement potential anisotropy in epitaxially grown QDs arises from several sources, like shape [52, 121, 122], strain [42, 79, 123], piezoelectricity [42, 124] and crystal symmetry [79]. Several theoretical and experimental works tried to assess the role of each of the aforementioned anisotropy sources in determining the QD exciton FSS. However, the majority of the papers report about FSS in SK–QDs, where a number of not–well determined and interconnected QD structural

parameters, like actual shape [124], average composition [125] and composition profile [126], make the quantitative comparison with theoretical prediction rather difficult. In addition, it must be mentioned that all the theoretical predictions [42, 79, 123, 127] fail to justify the observed large FSS observed in SK–QDs (where FSS larger than 100 μeV are often observed [42]) when realistic QD structural characteristics are used in the calculations. It clearly appears that for a deep understanding of the FSS it is necessary to experimentally clarify the influence of strain, piezoelectricity, geometry and composition separately.

In this Section we present a high–resolution, polarization–dependent photoluminescence (PL) study in single epitaxial $GaAs/AlGaAs$ strain free QDs as a function of the QD size/emission energy. The exclusion of the strain related piezoelectric effect, whose relative importance in determining the FSS in SK–QDs is still matter of strong debate [42, 79, 123, 124], allows us to obtain a nice correlation between the observed FSS and structural data. Our QD PL lines exhibit FSS which monotonically decreases from 90 μeV to 20 μeV when decreasing the quantum dot size. The FSS decrease closely follows the reduction in $[110]/[1\bar{1}0]$ shape anisotropy that takes place in our QDs as the size is reduced. When the structural asymmetry in our QDs is close to zero we find that the QD linear polarization axis results significantly distributed along random oriented directions. These findings, together with the observed cylindrical symmetry of the QD shape, highlights the role of extrinsic effects as significant contribution in determining the QD potential anisotropy.

The sample studied consists of MDE $GaAs$ QDs embedded in an $Al_{0.3}Ga_{0.7}As$ barrier. Particular care was taken in order to avoid modifications of the structural properties of the QDs during the capping step, which has been realized using mobility enhanced epitaxy [62] at an extremely low temperature (200 °C). The last step of the growth, is an annealing procedure in As atmosphere. This allows

for a substantial reduction of the defectivity of the material at the expenses of a relatively small (around 1 nm) group III interdiffusion at the interfaces [55, 128]. More details on the growth procedure and annealing effects can be found in Refs. [55] and [36].

Micro PL experiments were performed with the setup previously described and high resolution spectra (25 μeV spectral resolution) were acquired. With a fitting procedure we are able to identify PL line shift as small as $\sim$5 μeV. For illumination we used a continuous-wave solid state laser emitting at a wavelength of 532 nm, to excite the continuum states of the $Al_{0.3}Ga_{0.7}As$ barrier. The excitation spot size was 5 μm. The excitation polarization was set to be linear to avoid Overhauser effects [114, 129]. The linear polarization detection was controlled by rotating an half-wave plate, inserted in front of a linear polarizer.

A typical PL spectrum of a single $GaAs$ QD is shown in Fig. 5.3(a). This attribution has been confirmed by single photon correlation experiments [57], showing antibunching (bunching) in the cross correlation X–T (X–XX) measurement (see Chap. 6). The linewidths are found to vary between tens to hundreds of μeV reflecting spectral diffusion due to the presence of charged defects in the QD environment. In Fig. 5.3(c) we report the orthogonally-polarized PL spectra of two different QDs. A mirror-symmetric fine structure is evidenced for X and XX, while no splitting is observed for T, being consistent with the attribution of these lines. The measured FSS Δ defined as the maximum splitting of two orthogonally polarized lines is: $\Delta_X = 62$ μeV and $\Delta_{XX} = 60$ μeV (top panel); Δ_X=18 μeV and $\Delta_{XX} = 20$ μeV (bottom panel) with an error of $\pm 5\mu$eV. As expected we find that $\Delta_X = \Delta_{XX}$ within the experimental error. Therefore to extract the dependence on the QD size we report the mean value $(\Delta X + \Delta XX)/2$ as a function of the X emission energy. We measured the FSS magnitude for several QDs. The summary is presented in Fig. 5.4, where Δ is reported as a function of the X energy.

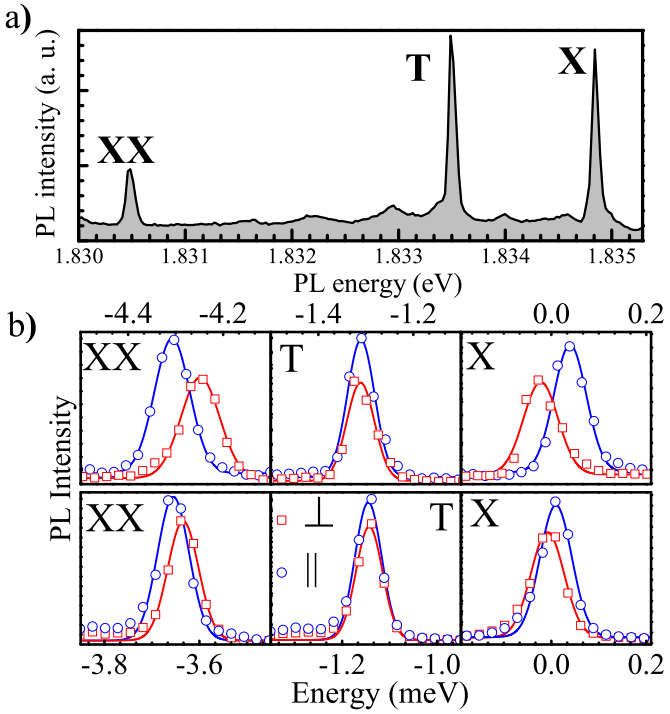

Figure 5.3: (a) PL spectrum of a single $GaAs/AlGaAs$ QD in the high excitation regime. The three line X, T and XX are interpreted as neutral exciton, trion and biexciton emission. (b) Polarized PL spectra of two different QDs. The top panel refers to the QD of (a). Blue circles and red squares indicate the spectra of two orthogonal polarization, of which relative angle is shown in the legend. Lines are gaussian fits. The horizontal axis is shifted by the energy of X (1834.9 meV and 1875.7 meV for top and bottom panel, respectively).

Spanning an interval of $\sim$ 200 μeV, the FSS Δ clearly monotonically decreases with increasing the X energy. When the X line is at low energy, the FSS is found to be approximately 90 μeV while for smaller QDs corresponding to emission at 1.89 eV the value of Δ is as small as 18 μeV.

Comparing the values of FSS of our QDs with those of SK $In(Ga)As/GaAs$ QDs, we observe that both the FSS absolute values and the FSS behavior with the QD size are similar [42] despite the absence of strain–related piezoelectricity

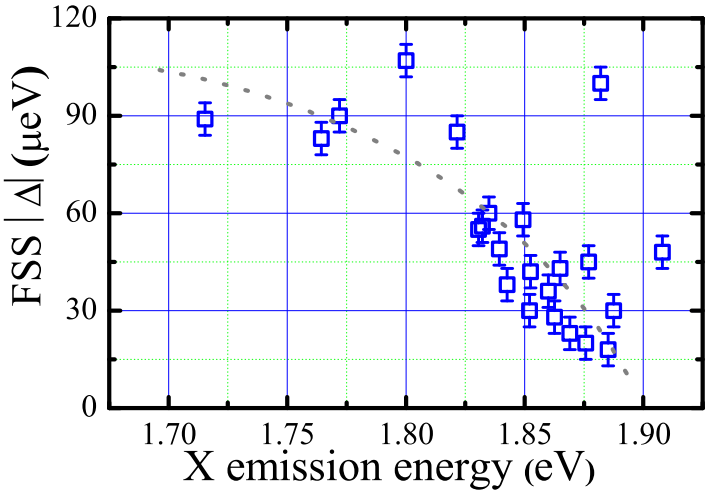

Figure 5.4: FSS of QDs emitting at different energy. The reported values are the average value of FSS's for X and XX. The dotted line is a guide to eye.

in the present case. In fact the relatively high value of FSS in SK–QDs and its reduction with the size has been attributed to potential anisotropies caused by the piezoelectric field [42]. Clearly the assignment to piezoelectric effect cannot be applied to the case of strain free $GaAs/AlGaAs$ QDs and then our findings rise doubts also in the attribution to piezoelectric effect for SK–QDs. As a matter of fact, amongst the possible origins of FSS, the effect of the piezoelectric field is the more controversial one [79, 123, 124, 130]. Due to high value of the strain in the $InAs/GaAs$ SK–QDs, linear and non–linear terms in the piezoelectric tensor can be of comparable intensities [130] and, depending on the QD shape and composition profiles, the non–linear terms may effectively balance out the linear ones [124, 130].

To understand the role of geometry in the QD asymmetry we measured size and shape of several $GaAs/AlGaAs$ QDs on the same but uncapped sample. Typical atomic force microscope (AFM) images of the lens–shaped $MDE-QD$, in the case

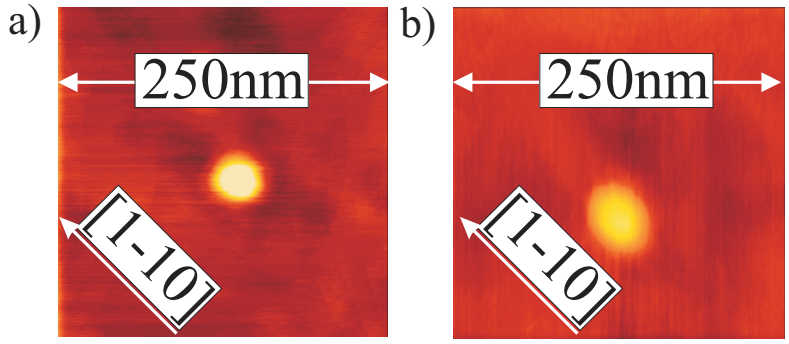

Figure 5.5: a) and b): 2D representation of the AFM analysis of a "small" QD (h=3.9nm) and a large QD (h=11.8nm) respectively.

of a large and a small QD, are shown in Fig.5.5. Extensive AFM measurements show relevant dispersion of size and shape. This analysis points out that QDs with small height h show a small elongation in $[1\bar{1}0]$ direction while for large value of h, the QDs show a larger elongation in the same direction (respectively $\sim$8% and $\sim$20% in the case of graph (a) and (b) of Fig.5.5). The relative error in the diameter measurement is assumed to be 5%. The observed dependence of the $MDE-QD$ shape anisotropy with size was expected considering the kinetics of the $MDE-QD$ formation [36]. We expect that the $MDE-QD$s retain their shape also after capping (being realized at extremely low T) and annealing (only interdiffusion at the interfaces is expected). From AFM data a simple and likely explanation of the dependence of the FSS on the QD emission energy emerges. The in plane asymmetry augments when increasing the QD size leading to a larger splitting of the exciton recombination line along the crystallographic axis $[1\bar{1}0]$ and [110] for large QDs. It's worth noticing that even a relatively small elongation gives rise to FSS of 90 μeV, thus showing that geometrical anisotropies play a much larger role than expected from theoretical predictions [52, 79, 121, 123, 124].

In order to get further information on the origin of FSS and to obtain an accurate characterization of the polarization splitting, we measured a series of

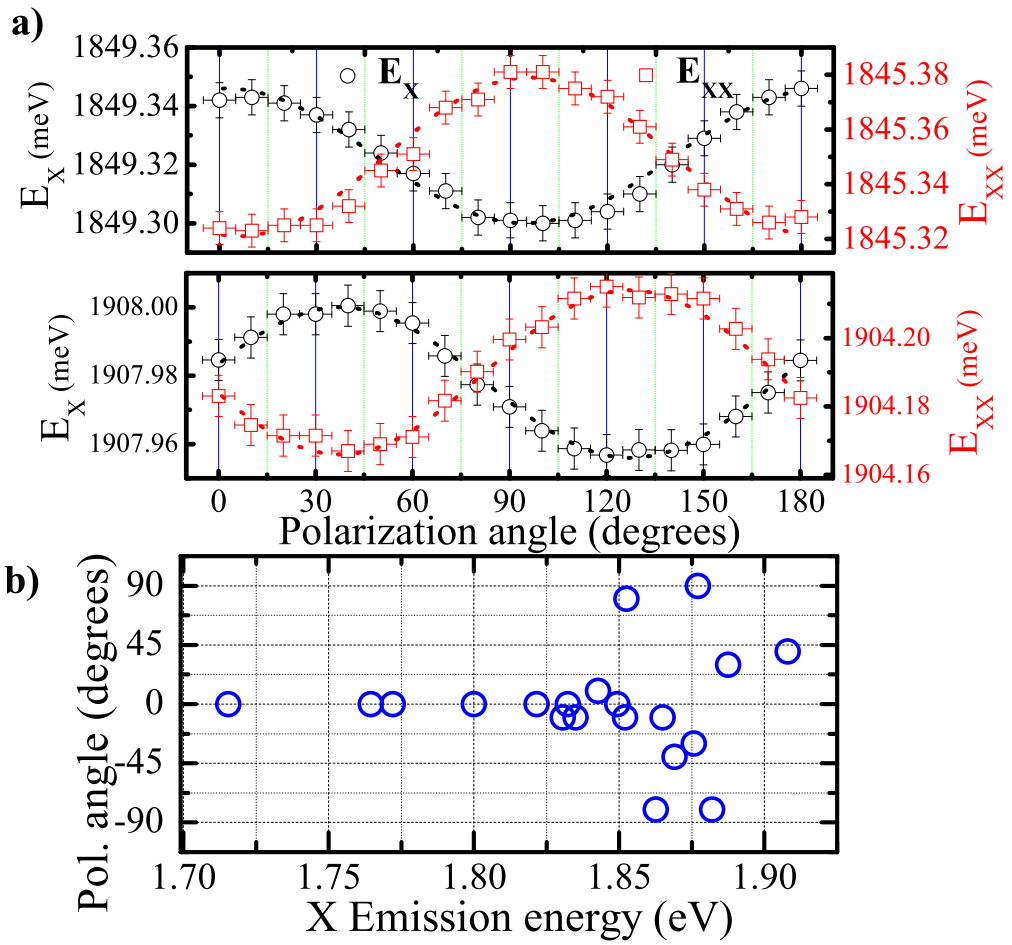

Figure 5.6: a) in top and bottom panels black circles (red squares) show the energy evolution of X (XX) with polarization angle for two different QDs. Left and right vertical axes are referred to X and XX case respectively. The PL peaks evolutions are fitted with sine functions as evidenced by black and red dotted lines thus determining amplitude (the FSS) and the phase shift (the main polarization axis). b) one polarization axis plotted versus X emission energy.)

spectra varying the polarization angle. Following the evolution of the centroid of PL lines with polarization angle, we obtain a clear sinusoidal behavior as shown in Fig. 5.6(a) for two different QDs. Fitting the experimental data to a sine function, we can measure the amplitude (the FSS shown in Fig.5.4) and phase, thus determining the polarization axis of each QD. Not all the QDs show anisotropy along the crystallographic axis [110] (corresponding to the polarization angle in the direction 90°), the measured asymmetry axis of the $MDE - QD$s. On the contrary we found that there are several QDs showing the maximum FSS at angles different from 0° and 90°. The summary of this study is shown in Fig. 5.6(b) where the plot of the polarization axis angle versus the X emission energy is reported. It clearly follows that large QDs show the expected anisotropy along 90° and that the stronger deviations for the expected polarization axis are mainly associated to smaller QDs. In fact for emission between 1.70 eV and 1.86 eV the polarization axis is close to 90° while for higher emission energy, where the FSS is smaller, the deviations from this value become more important. Deviations of the polarization direction of the FSS from the crystallographic axes can be found in $SK - QD$s [127, 131, 132] but this effect has not been attributed to a definite origin.

Therefore our data point out that higher symmetric QDs showing smaller FSS are influenced in their internal symmetry by a factor different from the geometrical anisotropy. This is likely due to the fact that small, extrinsic, QD potential symmetry reduction effects can be present in addition to intrinsic ones. We believe that a tentative explanation may rely on the presence of charged defects in the environment nearby the QDs. Besides the fluctuating quantum confinement Stark shift, which is well known to induce spectral diffusion in the emission of the QDs, the averaged Coulomb interaction also defines an asymmetric potential for charges confined in the QDs, therefore leading to a FSS. The random relative position of the charged defects and the QDs then results in a random orienta-

tion of the observed polarization axes, thus explaining our findings. This picture agrees with recent findings on the random oscillatory dependence of the FSS on an externally applied electric field [131]. Under the action of the electric field, charging/decharging of traps located randomly in the vicinity of the QD, should cause fluctuations of the axis as well of the magnitude of the QD anisotropic potential. A theoretical discussion of this effect can be found in Ref. [133]. Alternatively the FSS may be related to $AlGaAs$ composition fluctuations nearby the QDs.

Therefore the observations concerning FSS and the polarization axes orientation in small QDs highlights the role of extrinsic effects in the attribution of the FSS in semiconductor QDs so far neglected.

Chapter 6

Time correlated measurements: bunching-antibunching experiments

This chapter is devoted to the study of the intensity correlation properties of single GaAs/AlGaAs *QDs. At low excitation, we observed nearly perfect single photon emission from an isolated QD. For higher excitation, multiple PL lines appeared on the spectra, reflecting the formation of exciton complexes. Cross-correlation functions between different lines showed either bunching or antibunching behavior, allowing a clear identification of the different excitonic complexes.*

6.1 Single photon emission from *GaAs/AlGaAs* quantum dots

The quantum nature of light emitted from single semiconductor quantum dots (QDs) has attracted much attention because it can enable the practical processing of quantum information [118]. Production of single photons on demand was demonstrated in a variety of QDs [70, 134] and QDs embedded in optical cavities [15, 135, 136, 137, 138]. Furthermore, the generation of entangled photon pairs associated with a biexciton-exciton cascade was proposed [17] and experimentally verified [18]. In this context, cascade relaxation in exciton complexes is a key for acquiring a correlated photon source with high efficiency. Many studies for the generation of single and correlated photons have focused on Stranski Krastanov grown $In(Ga)As$ QDs in an effort to develop a nonclassical photon source operating at near-infrared telecommunication wavelengths [139, 140, 141]. For practical application, however, it would also be desirable to work in wavelengths around 700 nm where commercial silicon-based single photon detectors reach their maximum quantum efficiency (up to 70%). So far, photon correlation studies in InP QDs (640÷ 690 nm)[142] and $InAlAs$ QDs (770÷780 nm) [143] have been reported. Another advantage of exploiting QDs with shorter wavelengths is their enhanced radiative probability according to the expression of the Einstein A coefficient [144]. This feature may produce Fourier-transform limited single photon pulses with a high-repetition rate, which are useful for various applications such as linear optics quantum computation and free-space quantum cryptography. In this section we report on auto-correlation measurements on a single $GaAs/AlGaAs$ QD excited by a pulsed laser. For excitation, second-harmonic output of mode-locked Ti-sapphire laser was employed. The laser produced picosecond pulses of 400 nm in wavelength and 76.0MHz in repetition rate. The experimental apparatus for the

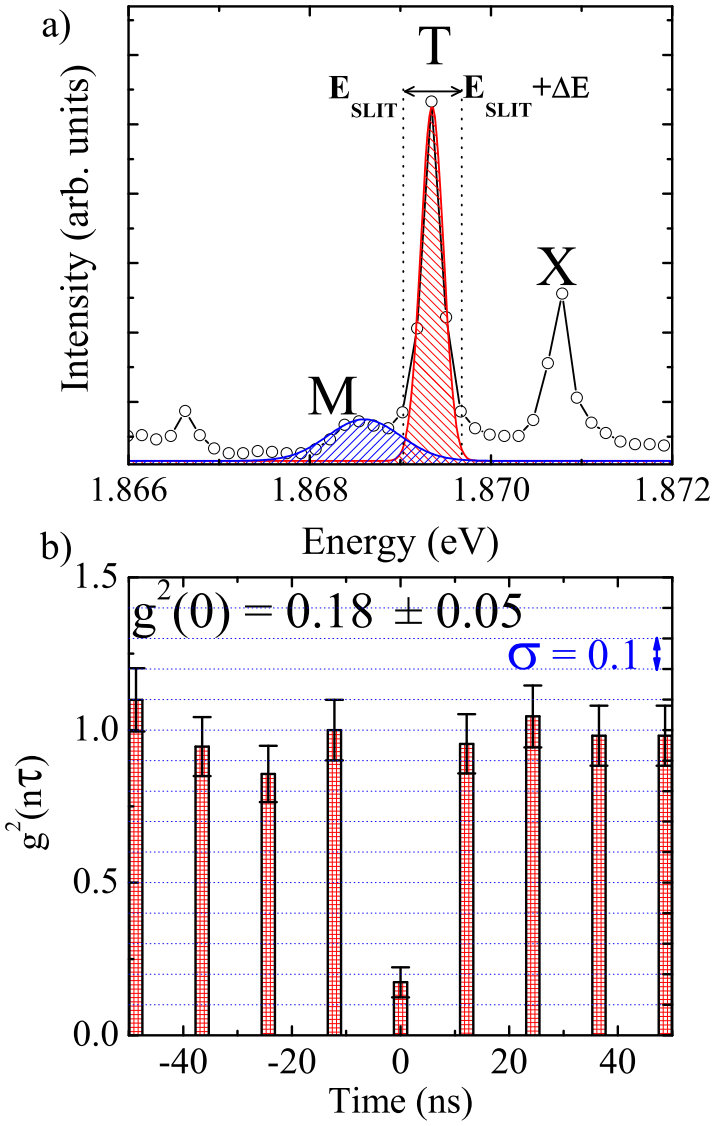

Figure 6.1: (a) Photoluminescence spectrum of a single *GaAs/AlGaAs* quantum dot under pulsed excitation. The shaded areas under the gaussian fit of the T and XX lines are used for the determination of the background contribution in the anti-bunching experiment. The vertical dotted lines labeled as E_{SLIT} and $E_{SLIT} + \Delta E$ indicate the spectral window selected by the exit slits of the two spectrometer in the HBT arms (ΔE = 640 μeV). (b) Normalized $g^{(2)}(\tau)$ measured for the T line in the spectrum of graph (a). The vertical error bar is proportional to the square root of counts in each bunching peak.

PL collection and for the correlation measurement has been previously described in Chapter 2.2.1. PL spectra were acquired using a cooled charge-coupled-device. All experiments were performed at cryogenic temperature.

We refer to Appendix 8 for details on the $g^{(2)}(\tau)$ correlation function. Here we concentrate on the experimental details and the extraction of the $g^{(2)}(0)$ value. The analysis of the measured $g^{(2)}(0)$ by a precise estimation of the background contribution allows us to demonstrate a perfect antibunching feature of the spectrally filtered QD emission. This demonstrates the nature of single photon emitter of the *GaAs/AlGaAs* QD system.

The typical photoluminescence spectrum from a single *GaAs/AlGaAs* QD under pulsed excitation is shown in Fig. 6.1 (a). Two prominent contributions to the PL spectrum, indicated as X and T, are attributed to the neutral exciton and charged exciton (for the line attribution see Sect. 3.1 and in the following 6.2). Besides, in the intermediate and high excitation regime, the spectrum is composed by several other lines (M in Fig. 6.1 (a)) that, due to the low dispersion and spectral resolution (see Sect. 2.2.1), may show a relevant overlap with the main contribution. As an example of this we evidenced the T and M line in Fig. 6.1 (a) with a shaded area under the gaussian fit of the two lines.

A typical result of the correlation experiment measured with the Hanbury Brown and Twiss (HBT) interferometer (see Section 2.2.1), is presented in Fig. 6.1 (b). The histogram represents the autocorrelation function $g^{(2)}$ of the charged exciton emission T measured under pulsed excitation. The spectral window selected by the exit slit for the autocorrelation measurement was 640μeV (as evidenced by the vertical dotted lines in Fig. 6.1 (a)) while the chosen time bin of the histogram was 3 ns, thus integrating over the instrumental response of the interferometer ($\sim$ 1 ns $FWHM$ in the present case). In the histogram the contribution due to the uncorrelated background PL and to the APD dark counts were evaluated and

subtracted. The effect of the background was estimated calculating the average counts per channel in a window of 3 ns between each bunching peak. The obtained histogram has been normalized to the average counts of the bunching peaks excluding the 0 time delay. The corresponding standard deviation is 0.1. The error associated to the bunching peaks is the square root of the counts contained in each peak suitably normalized as represented by the error bars in graph (b) of Fig.6.1. We obtain antibunching deep at zero delay of $g^{(2)}(0) = 0.18 \pm 0.05$ which is 8 standard deviation far from the average value of the other peaks. The anticorrelation feature of the emitted photons denotes a small probability to have two photons in the same excitation cycle. Since an ideal single photon source would show a $g^{(2)}(0) = 0$ we interpret our result as affected by spurious counts due to the presence of uncorrelated photons in the chosen spectral window. The contribution of the line M to the $g^{(2)}(0)$ can be evaluated by integrating the corresponding gaussian profile over the 640 μeV of the selected spectral window centered around the T peak. The presence of two photon sources M and T within the detection window, which intensity are I^M and I^T respectively, modifies the value of the $g^{(2)}(0)$ which becomes:

$$g^{(2)}_{M+T}(0) = g^{(2)}_M(0) + g^{(2)}_T(0) + \frac{2I^M I^T}{(I^M + I^T)^2} \simeq g^{(2)}_T(0) + \frac{2I^M I^T}{(I^M + I^T)^2} \tag{6.1}$$

We then evaluate from the spectrum:

$$\frac{2I^M I^T}{(I^M + I^T)^2} = 0.11 \tag{6.2}$$

This expression allows to extrapolate the real value of the autocorrelation function for the T line: $g^{(2)}_T(0) = 0.07 \pm 0.07$ which is consistent with an ideal photon source within the experimental error.

6.2 Cross-correlation measurement

As previously shown for the T contribution, the Hanbury Brown and Twiss setup can be used for the investigation of the triggered single photon emission through the measurement of the auto-correlation function $g^{(2)}(0)$. Besides, the same setup provides information about the emission of correlated photons emitted by two distinct light sources. In fact the study of the cross–correlation function allows a clear–cut attribution of the spectral components in the $QD\ PL$. In this Section we show auto- and cross–correlation measurements for the attribution of the main lines in the spectrum to the recombination of neutral exciton X, charged exciton T and biexciton XX. This study has been carried on under pulsed and CW excitation in order to fulfill our results.

6.2.1 Pulsed excitation measurement

In Fig. 6.2 (a) are reported typical photoluminescence spectra of a single quantum dot under pulsed excitation. Second-order autocorrelation function for the X emission, measured at $10W/cm^2$, is shown in Fig. 6.2 (b) panel (i). The number of coincidence events for the two APDs are summarized in a histogram with 512 ps time bin, thus integrating over all the HBT time response which is, in this case, $\sim$ 350 ps. The spectral window for the photon integration selected by the spectrometers exit slits was 500 μeV in $FWHM$. For this condition the mean number of photon events for each APD was 600 counts/s (cps). The periodic peaks appearing at regular intervals of 13.2 ns indicate that photons were emitted synchronously with pulsed excitation of 76.0 MHz and the lack of a peak at zero time delay indicates that there is almost no probability of finding two or more photons inside each emitted pulse (as previously discussed in Section 6.1 for the T line). In our QD, the correlation function at zero time delay, $g_X^{(2)}(0)$, is estimated to be 0.18

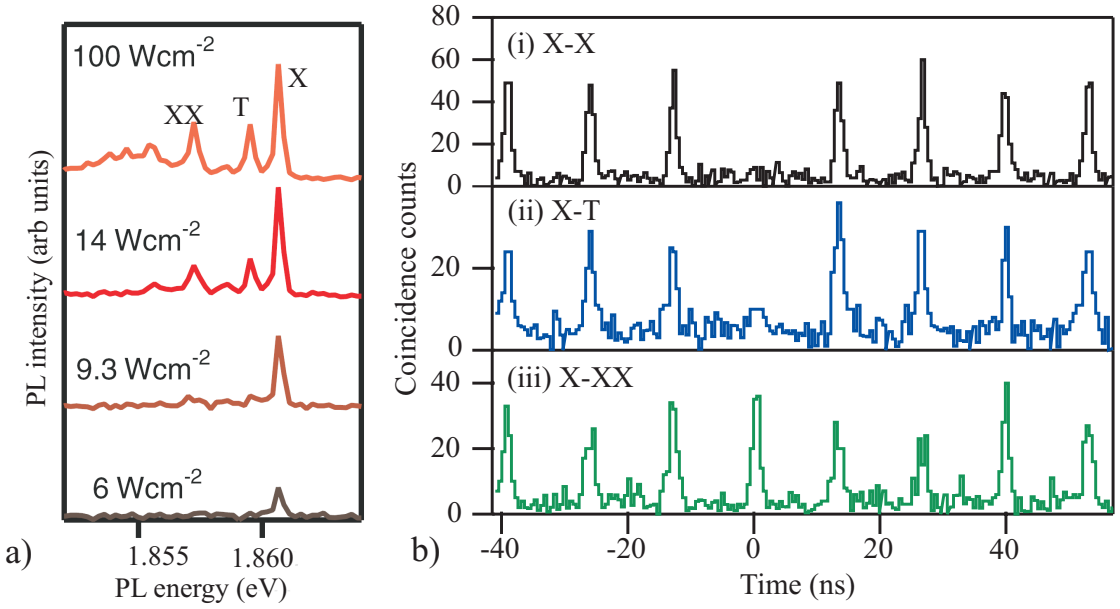

Figure 6.2: (a) Photoluminescence spectra of a single $GaAs$ quantum dot excited by a pulsed laser source. The spectra are shifted for clarity. (b) Second-order correlation functions of light emitted from a single $GaAs$ QD under pulsed excitation of 76.0 MHz repetition rate. The results of the autocorrelation for peak X is shown in (i), and those of the cross-correlation between X and T, and between X and XX, are shown in (ii) and (iii), respectively. In all histograms, the number of coincidence is temporally binned with 512 ps. The signals were integrated for 12 h in (a), and 6 h in (b) and (c).

(± 0.2). A value larger than zero would likely reflect the over-counting of coincidence, possibly due to the influence of stray light entering APDs and uncorrelated background. The results of cross-correlation measurement between peaks X and T are presented in Fig.6.2 (b) panel (ii), and those between peaks X and XX are shown in Fig.6.2(c). The excitation power in these measurements was increased to $50 W/cm^2$, in order to obtain high counting rates for peaks T and XX (400 cps for T and XX, 800 cps for X). The $X-T$ correlation shows the lack of a zero-time peak, similar to the $X-X$ autocorrelation. The value of $g^{(2)}_{X-T}(0)$ is estimated to be 0.3 (± 0.1). In contrast, the $X-XX$ correlation (see Fig.6.2 (b) panel (iii)) shows the emergence of a zero-time peak. The value of $g^{(2)}_{XX-X}(0)$ in this case is

nearly one, resembling a correlation function for Poissonian distributed photons. The observation of an antibunching feature in the $X-T$ correlation demonstrates that the T and X photons are not emitted simultaneously. This is a further proof of the charged exciton emission for the T line and line X from neutral excitons. Since the transition between a charged exciton and a neutral exciton requires the injection or extraction of a carrier, the relevant process is much slower than the recombination. As a result, either the X photon or the T photon is generated during a single emission cycle, leading to the observation of the antibunching dip. The emergence of the zero-time peak in the $X-XX$ correlation confirm that line XX is originated from biexcitons recombination. When a biexciton is inside a QD, the first photon is emitted at the biexciton energy, then the second photon is emitted at the single exciton energy. Since the process does not happen in reverse order, the cross-correlation function would exhibit asymmetric bunching ($\tau > 0$) and antibunching ($\tau < 0$) features, where a positive value of $g^{(2)}(\tau)$ corresponds to a time delay from the arrival of a biexciton-induced photon to that of an exciton-induced photon [145]. For pulsed excitation, we expect that $g^{(2)}(+0) > 1$ and $g^{(2)}(-0) = 0$, where the value of $g^{(2)}(+0)$ depends on the mean number of excitons, $\overline{N}$. The height of $g^{(2)}(+0)$ should be expressed by $[1 - exp(-\overline{N})]^{-1}$, when the number of $\overline{N}$ follows the Poissonian distribution [146]. Note that we increased the excitation power to $50W/cm^2$, suggesting that $\overline{N} \gg 2$ (see Fig.6.2). Thus, we find that $g^{(2)}(+0) < 0.16$, the value being smaller than the standard deviation of mean coincidence counts. This is why we did not resolve a significant bunching peak in the X–XX correlation [145, 146, 147].

6.2.2 Continuous wave excitation measurement

For a deeper insight in the photon correlation we performed the same kind of experiment presented in Section 6.2.1 under CW excitation. In fact, if the pulsed

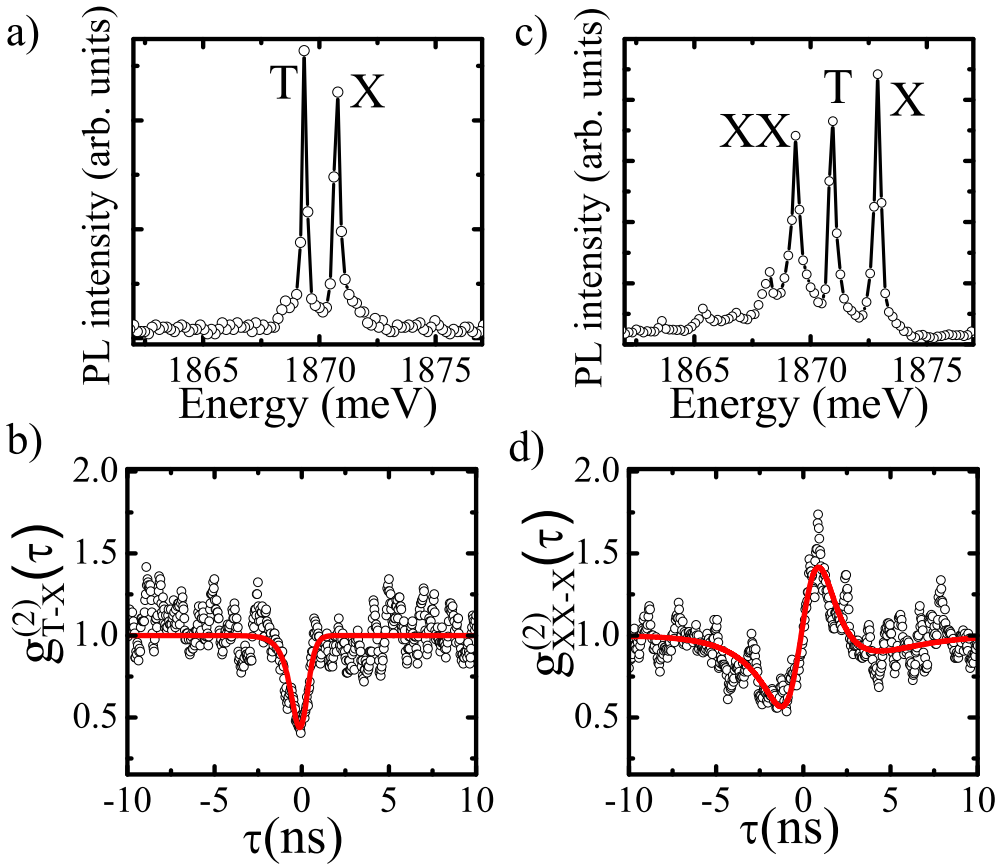

Figure 6.3: (a) PL spectrum of a QD (same of Fig. 6.1) under CW excitation. (b) Cross-correlation measurement $g^{(2)}_{T-X}(\tau)$ between T (START), and X (STOP). The data shown in this graph are normalized to the asymptotic value of the measured $g^{(2)}_{T-X}(\tau)$. The red line is a fit to the experimental data. (c) PL spectrum of a different QD under CW excitation showing a relevant biexcitonic emission. (d) Cross-correlation measurement $g^{(2)}_{XX-X}(\tau)$ between XX (START), and X (STOP). The red line is a fit to the experimental data normalized to the asymptotic value.

excitation measurement constitutes a sampling of the correlation function which provides direct information on the $g^{(2)}(0)$, the CW regime allows for a complete reconstruction of the $g^{(2)}(\tau)$.

The experimental setup is the same previously described in Section 6.1 but in this case the excitation was provided by a solid state CW laser emitting at 532 nm.

In Fig. 6.3 (a) and (b) the CW PL spectrum of the QD of Fig. 6.1 (a) and the corresponding normalized CW cross–correlation function $g^{(2)}_{T-X}(\tau)$ are respectively shown. In this experiment the START and STOP signals were provided by T and X photons, respectively. The second order cross–correlation function has been averaged over a 320 ps bin, which is smaller than our time resolution. As expected from the previous attribution of X and T lines the $g^{(2)}_{T-X}(\tau)$ shows a clear anticorrelated behavior. The red line in Fig. 6.3 (b) is a fit to the experimental data which takes into account the finite time response of the HBT interferometer with a deconvolution procedure.

In analogy with the previously shown investigation we measured the cross–correlation function for the $XX - X$ emission . The PL spectrum of the investigate QD is shown in Fig. 6.3 (c). The typical triplet structure present in our *GaAs/AlGaAs QD*s is labeled, as usual, by X, T and XX. In Fig. 6.3 (d) the corresponding cross-correlation function $g^{(2)}_{XX-X}(\tau)$ is displaced. In this case the START and STOP signals were provided by XX and X photons, respectively. A prominent bunching behavior for $g^{(2)}(\tau > 0)$ is found and it is interpreted as a signature of the high probability of observing an X photon after the detection of an XX photon. The antibunching dip of $g^{(2)}(\tau < 0)$ denotes the small probability of the reverse order of the emissions [145, 147]. The experimental data is deconvoluted from the instrumental response and fitted as shown by the red line in Fig. 6.3 (d). This result is in agreement with the previous attribution and is a clear

signature of the quantum cascade in the $XX \rightarrow X$ recombination.

We mention again that saturation effects are known to play a relevant role in the photon statistics of the QD emission and strongly affect the shape of the $g^{(2)}$ function [148]. In our measurements we interpret small bunching peak in the $g^{(2)}_{XX-X}(\tau > 0)$ as a saturation effect (about this problem see also Appendix 8).

We can therefore safely assign line XX to biexcitons, being consistent with the results of cross-correlation measurements between X and XX. In conclusion, we observed second-order correlation functions between emissions from exciton complexes in a single self-assembled $GaAs$ QD. Generation of single photons at a wavelength of 660 nm was confirmed. Both bunching and antibunching features were identified in intensity cross-correlation functions, revealing the origin of specific PL lines.

Chapter 7

Concentric quantum rings

In the following Chapter photoluminescence experiments on single concentric quantum rings are presented. In the first part some morphological details and their influence in the exciton level arrangement are described. In the following sections the concentric quantum ring excitonic dynamics is analyzed by time resolved and time correlated experiments providing information about the state filling, the single photon emission properties and the inhomogeneous line broadening affecting the CQR emission.

7.1 Level structure and optical properties

In this section the main electronic and optical properties of concentric quantum rings are shortly introduced [60]. Two kinds of samples are studied: a single-wall ring and a concentric double-ring (see images (a) in Fig. 7.1 and 7.2). From the comparison of the emitted photoluminescence (PL) of single and concentric double rings (QR and CQR respectively) and with the theoretical simulations we can account for the main lines composing the spectra.

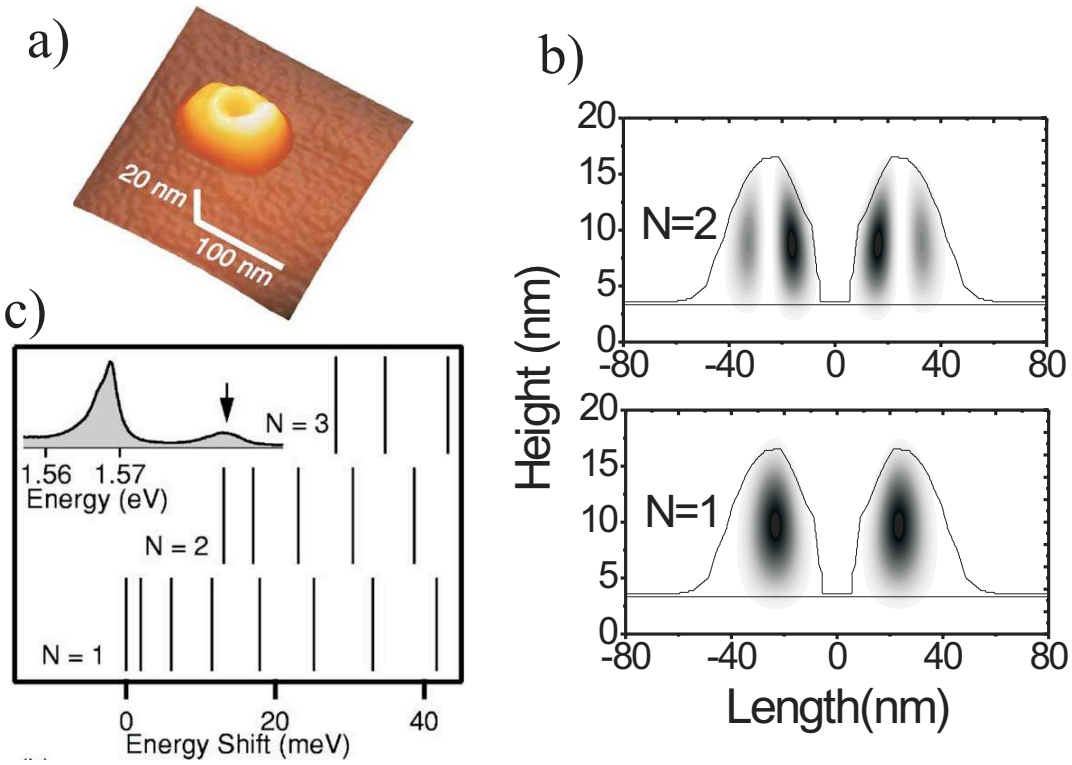

Figure 7.1: (a) atomic force microscope images in 250×250 nm^2 area for a single $GaAs$ quantum ring grown by droplet epitaxy. (b) cross-sectional imaging of electronic probability density in QR for N = 1 and 2 with $L = 0$. The line represents the potential of confinement used for calculation and is deduced from the AFM profile. (c) a series of optical transition energies in QR, obtained by the calculation. The PL spectrum of QR is shown in the inset.

For both samples the spectra show discrete resonance lines, which reflect the quantized nature of the ring-type electronic states. The PL spectrum of a QR typically shows two major contributions: a first line in the low excitation regime and a satellite line in the high energy side (see inset of Fig.7.1 (c)). Further increase in excitation density causes saturation in the intensity of the original line along with a nonlinear increase in the new line. Superlinear dependence of the emission intensity suggests that the satellite line comes from the electron-hole recombination of an excited level of the ring [60]. Typically, the energy difference between the ground and the excited state in the QR is ≈10 meV.

Analogous investigation was made for CQR (see Fig. 7.2 and 7.3). Typically the CQRs show a good circular symmetry, whereas small elongation is found along the $(01\bar{1})$ direction ($\sim$5% for the inner ring and $\sim$8% for the outer ring; see Fig. 7.3). Similarly to the case of QR, the spectra consist of discrete lines, i.e., a main peak following a satellite one, which is at the high energy side of the main peak. The former is associated with recombination of carriers in the ground state, whereas the latter is from the excited states. The energy difference between the ground-state line and the excited-state one varies between 5 and 10 meV. We point out that, in contrast to the QR case, we observe the satellite peak even at the lowest excitation [60] and, the power dependence of the two components IR and OR is usually very similar. At high excitation, we find that several additional lines ($M1$ and $M2$ in Fig. 7.9) are superimposed on the spectra. We interpret these lines as the radiative recombination from multiexcitonic states, in fact their power dependence is usually superlinear with respect to the low lying states.

The line broadening associated to the main peaks of both QR and CQR is usually hundreds of μeV and will be widely discussed in the following sections.

We theoretically evaluate the energy levels of the ring nanostructures in the framework of a single-band effective-mass envelope model following Ref.[101]. The actual shape measured by AFM is used as quantum confinement potential; for simplicity, the ring is assumed to hold a cylindrical symmetry. Note that, in our lattice-matched $GaAs/AlGaAs$ rings, strain effects are negligible. Therefore, the simple effective-mass approach is expected to provide accurate energy levels. We also notice that the present calculation neglects Coulomb interaction between an electron and a hole. Because our rings are sufficiently small that confinement effects are dominant, the Coulomb interaction can be treated as a constant shift in the transition energies, independent of the choice of an electron and hole state. We restrict ourselves to calculate the single-carrier energy levels, discarding Coulomb

correlation effects. A detailed review of the calculations can be found in Ref.[60].

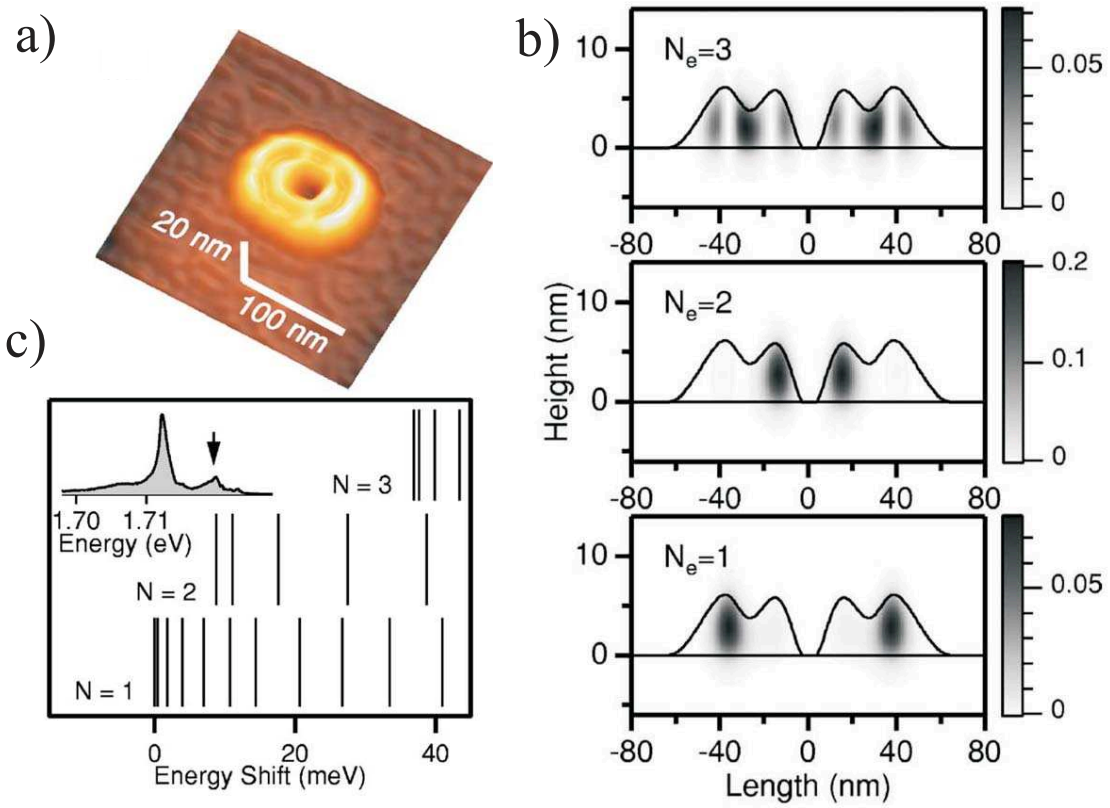

Figure 7.2: (a) atomic force microscope images in 250×250 nm^2 area fora single $GaAs$ concentric quantum ring grown by droplet epitaxy. (b) cross-sectional imaging of electronic probability density in CQR for N = 1, 2, and 3 with $L = 0$. The line represents the potential of confinement used for calculation deduced from the AFM profile. (c) the energies of optical transitions in CQR, together with the PL spectrum of CQR for comparison.

A series of single-carrier levels of QR is shown in Fig. 7.1 (b). Because the system has cylindrical symmetry, each level is specified by the principal *radial* quantum number $N = 1, 2, ..n$, and an azimuthal quantum number L, corresponding to the angular momentum. Two levels with $\pm L$ are degenerated at zero magnetic field. The carrier levels belonging to each radial quantum number are aligned vertically with those of a different angular momentum. We find that a vertical $L - dependent$ sequence of quantized levels shows a typical signature of ring-type

confinement. The comparison of the calculations and the μPL spectrum is shown in Fig. 7.1 (c). Further, the wavefunction displaced in Fig.7.1 (b) of $N = 1, 2, 3$.

The energy levels in CQR are shown in Fig. 7.2 (c) and they are compared to the measured CQR spectrum. As a result of the smaller height, the quantization energies are larger than those of a QR. The level sequence of $N = 1$ is more dense than that of $N = 2$. This situation corresponds to the large effective value of the ring radius R for $N = 1$. The split between the two transitions agrees with the energy shift obtained by experiments [60]. From the AFM investigation (see

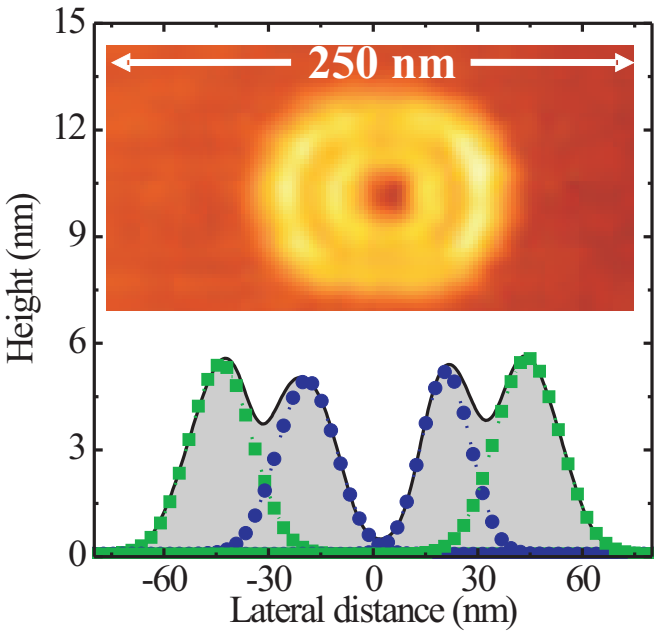

Figure 7.3: (Color online) Cross section of the AFM image of inset. Inset: typical AFM image of a $GaAs$ CQR. The CQRs show good circular symmetry, whereas a small elongation is found along the [1$\bar{1}$0]. The inner ring dimensions are 40 nm diameter with 5.2 nm height, and the outer ring dimensions are 90 nm diameter with 5.6 nm height, respectively. The green squares and the blue circles represent the gaussian fit to the section profiles of the outer and inner rings respectively. The full width at half maximum (FWHM) of OR and IR are 21 and 18 nm respectively.

Fig.7.3) emerges that the OR has not only a larger diameter but also shows a broader width (the amplitude of the cross section) and a larger height with respect to the IR. This is shown by the gaussian fit of the CQR cross section shown in Fig.7.3. The energy separation of the two lines varies depending on the CQR considered being dependent on the specific width of the IR and of the OR.

We show the comparison between the experimental spectra of CQR and the results of calculation in Fig. 7.2 (c). 7.2 (b) illustrates the envelope wave function of an electron for various values of N and zero angular momentum. We find that the electron of $N = 1$ is confined mainly in the outer ring. The wave function associated to $N = 2$ is confined in the inner ring, and that of $N = 3$ is situated in both rings. The amount of penetration for the electron of $N = 1$ to the inner ring is found to be ~ 0.1, whereas that of $N = 2$ to the outer ring is ~ 0.05. Thus, the two peaks in the observed spectra come from the two rings, which consist of a CQR. Note that the excited state emission in our experiment appears even when the carrier population is less than 1. The presence of this emission constitutes direct evidence for the carrier confinement into the two rings.

Finally, because of cylindrical symmetry, optical transition is not allowed for an electron and a hole with different angular momentum. Moreover, we have determined the transition strengths for the e-h pair with different Ns as less than 1/10 smaller than that with the same Ns. We can therefore infer that the electron, specified by a pair of N and L, recombines only with the hole of the same N and L.

7.2 Exciton dynamics in concentric quantum ring

We present a detailed analysis of the emission of individual $GaAs/AlGaAs$ concentric quantum rings. Time resolved and excitation power density dependence of

the photoluminescence have been used in order to determine the carrier dynamics in concentric quantum rings. Despite the small spatial separation between the two rings the exciton dynamics of the inner (IR) and outer ring (OR) is completely decoupled. A significant increase of the emission width and risetime, respect to the quantum dot case, characterize the emission of the rings. We attribute such phenomenology to the exciton center of mass localization induced by ring height fluctuations in quantum wire like fashion.

In this section we report detailed measurements of time resolved photoluminescence of individual CQRs as function of the excitation power density P_{exc}. We clearly find that the recombination kinetics of carriers in the inner and outer rings are decoupled. This is verified also at high carrier injection, when the PL of each ring evolves in independent multiplets, clear signature of multiexcitonic emission. We conclude that exciton localization effects dominate the radiative recombination rate in CQRs.

We performed time resolved measurements for four different single CQRs (labeled as CQR1,2,3 and 4) under non–resonant excitation in the $AlGaAs$ barrier. The sample was investigated with the same μPL setup described in Chap.2, the excitation was provided by a dye at a wavelength of 600 nm; the pulse duration was 5 ps with a repetition rate of 76 MHz and P_{exc} in the range 1 W/cm^2 – 100 W/cm^2. The signal was detected by a Peltier cooled CCD, for time integrated measurements, and by a microchannel photomultiplier with a time correlated single photon counting setup, for time resolved measurements. The spectral resolution was of 0.2 meV and the time resolution, after standard deconvolution procedures, was below 20 ps.

Fig. 7.5 reports the typical photoluminescence spectrum of an individual CQRs. The emission spectrum of individual CQR is always a doublet, whose components are separated by few meV (see Table 7.1). The width of each single

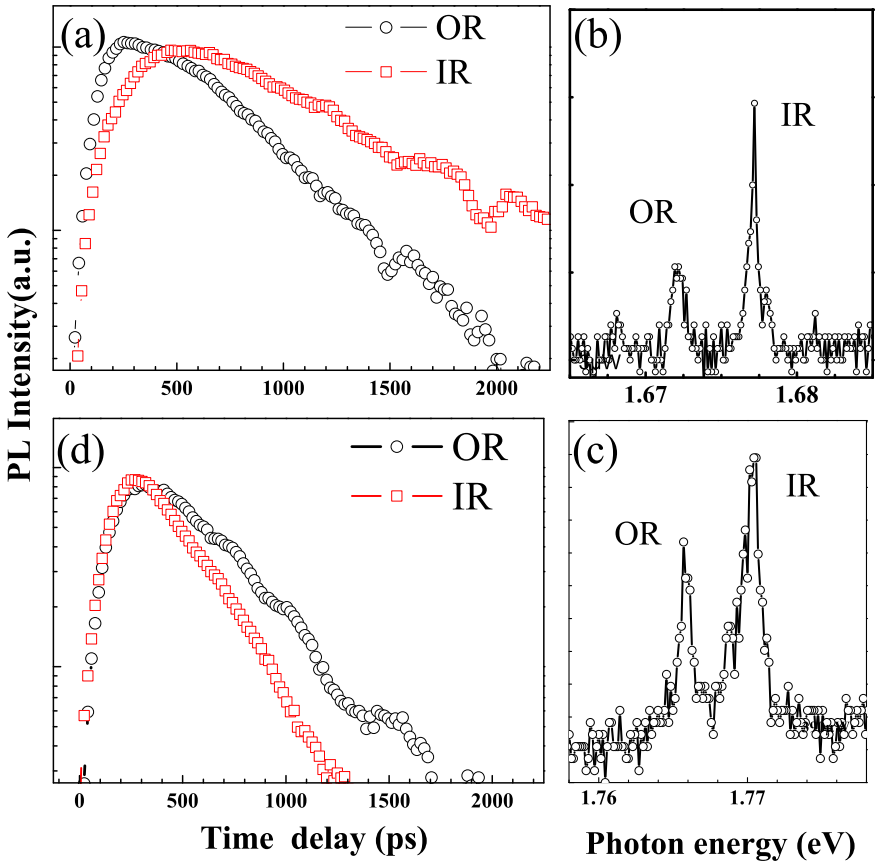

Figure 7.4: Panel (a): Time resolved PL, at T=10K and P_{exc}= 10 W/cm^2, of $CQR2$. Open circles indicates OR emission, full squares IR emission; Panel (b): PL spectrum of $CQR2$ at T=10K and P_{exc}= 10 W/cm^2. Panel (d): Time resolved PL, at T=10K and P_{exc}= 3 W/cm^2, of $CQR3$. Open circles indicates OR emission, full squares IR emission. Panel (c): PL spectrum of $CQR2$ at T=10K and P_{exc}= 1 W/cm^2.

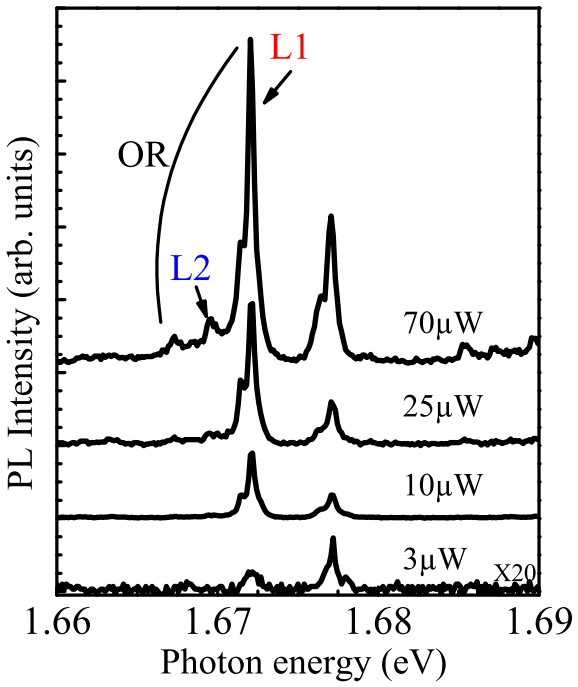

Figure 7.5: Time integrated spectra of $CQR3$ at different excitation power densities at T=10K.

line in the doublet is close to 1 meV, ranging from 1.1 meV of $CQR1$ to 0.8 meV of $CQR3$ although linewidth as small as 300 μeV can be found. This values is very large for individual nanostructures and it has to be attributed to inhomogeneous broadening mechanisms. It is also worth noting that spectral diffusion of PL line associated to chargeable defects nearby the nanostructure, commonly assumed for explaining the single QD broadening in the range of few hundreds μeV, seems hardly the explanation for the observed 1 meV broadening.

Fig. 7.4 also reports the time resolved emission, at low P_{exc}, of the two lines of different CQR doublets. The rise–time of the IR and OR lines of different CQR doublets is almost the same ($\tau_R = 120 \pm 40$ ps) in all the investigated CQRs. This value is about four times larger than the commonly measured τ_R for quantum dot

	IR		OR	
	E_{PL}(eV)	τ_D(ps)	E_{PL}(eV)	τ_D(ps)
$CQR1$	1.709	200±50	1.704	220±60
$CQR2$	1.770	230±50	1.766	350±100
$CQR3$	1.672	900±100	1.667	700±100
$CQR4$	1.795	600±100	1.789	900±200

Table 7.1: Emission energies (E_{PL}) and decay times (τ_D) of the measured IR and OR lines at T=10K and P_{exc}= 3 W/cm^2.

structures, even in the case of $GaAs/AlGaAs$ quantum dots [149]. On the other side, the PL lifetimes τ_D show large variations for the individual ring considered (see table 7.1). The spread of τ_D is possibly due to different shape and size of the CQRs [39] or, more likely, to the presence of non–radiative channels, since there is no clear correlation with the emission energy of the CQR. More important is the fact that, although small differences (within 30%) were observed between IR and OR decay time τ_Ds, the two lifetimes are quite similar for each pairs of rings, even if, as stressed before, the overall lifetime varies by more than a factor 4 for different CQRs. Note also that sometimes the IR decays faster than the OR and sometimes is the opposite.

Further insights on possible coupling mechanisms between CQR excited states may be found by performing state filling experiments. The dependence of the CQR emission on P_{exc} is shown in Fig. 7.5 for $CQR3$. Both IR and OR lines show superlinear dependence of the PL integrated intensity on P_{exc}. Above 10 W/cm^2 both IR and OR lines evolve to multiplets, with new lines, appearing on the low energy side of the fundamental transitions, whose relative intensities grow much faster, with P_{exc}, than the fundamental ones. The energy separation between the lines in the multiplets ranges from ≈ 2 meV (OR case) to ≈ 1 meV (IR case). More information on the nature of the multiplets origin can be gained by means of time resolved PL measurements as a function of P_{exc}, reported in Fig. 7.6.

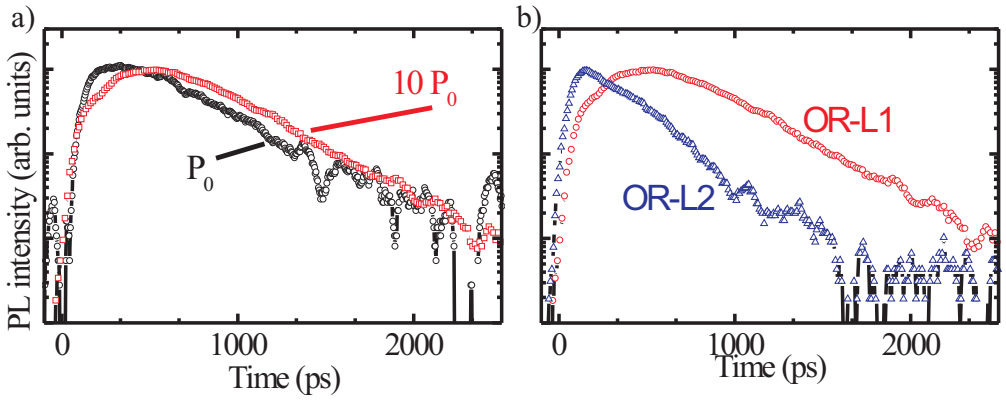

Figure 7.6: (a) time resolved PL of the OR line of $CQR3$ at T=10K and at different P_{exc}. (P_0= 3 W/cm^2). (b) Time resolved PL of the single exciton ($L1$ in Fig. 7.5) and the multiexciton ($L2$ in Fig. 7.5) line of the OR of $CQR3$, respectively. P_{exc}=30 μW and T=10K.

Strong increase of the PL risetime of the fundamental optical transition is found when increasing the power density, as due to state filling condition. At high P_{exc} correlated dynamics is observed between two lines corresponding to the multiplet which originates from the OR line at high P_{exc} (lines $L1$ and $L2$ in Fig. 7.5). The risetime of the line $L1$ corresponds to the decay time of line $L2$, thus demonstrating a link between the carrier population in the two states. Such correlation between decay and risetime indicates the origin from states which are bound in a cascade like behaviour. The observed energy differences, the relative dependencies on P_{exc} and the interlinked carrier dynamics of the lines in the OR multiplet make us to attribute $L1$ and $L2$ emissions to single and multi exciton recombination from the OR ground state, in close resemblance to the QD case [40, 57, 72]. As far as the carrier dynamics is concerned, IR fundamental line shows a similar behavior, denoting an independent state filling mechanism with respect to the OR case, even if the cascade like dynamics in the IR multiplet is partially hidden by the presence

of the OR recombination on the low energy side of the IR line.

Let us now discuss the experimental data in the framework of possible carrier tunneling and/or transfer between the two concentric quantum rings. The overall phenomenology presented here clearly excludes the picture of a carrier transfer between IR and OR, and we then conclude that the recombination kinetics of carriers in the inner and outer rings are decoupled. In fact, whether the carrier dynamics in the two structures were in some way correlated, a hierarchical order in the PL decay should be observed, with the shorter decay time belonging to the higher state, denoting a cascade mechanism associated to the carrier relaxation path. On the contrary, the IR recombination lifetime is always larger than the risetime of the OR emission. Moreover almost the same decay time is observed in IR and OR recombination for each CQR, even if large variations are reported for different CQRs.

Similar conclusions can be obtained by the analysis of carrier dynamics under large optical injection. For both IR and OR emission we observe the increase of risetime, when increasing P_{exc}. This is a clear evidence of saturation effects associated to state filling conditions. Such type of dynamics is illustrated by the lines $L1$ and $L2$ present at high P_{exc} in the emission of the OR of $CQR3$. As we stated before, the $L1$ and $L2$ lines of the OR multiplet are attributed to single and multi exciton recombination. Their emission energy difference stems from a different occupation of the ring which changes the number of spectator excitons from several (line $L2$) to zero (line $L1$), thus making the dynamics of two lines strictly correlated. At the same time, if we compare the time dependence of the IR and OR at P_{exc}= 70 W/cm^2 lines, we cannot find any correlation between rise and decay times of the emission, thus showing that the carrier dynamics in the two rings is decoupled.

Therefore, as already stated before, we have experimentally proved that the

photoinjected carriers follow independent relaxation paths within the electronic level structures of the two CQRs, in agreement with the assumptions made in [60], on the basis of CW–PL measurements. Such decoupling of the carrier kinetics happens despite the proximity of the two rings in a CQR structure. If we suppose that the exciton are free to move over the whole ring, the lack of coupling between the two rings could be traced back to the lack of resonance conditions between states having the same angular momentum values inside the IR and OR. But other effects, as we see in the following, may play a role. As a matter of fact, as far as the energy relaxation efficiency of the electron–hole pairs photogenerated in the quantum rings is concerned, it should be noted that the low P_{exc} measurements show relative large values of τ_R, compared to the QD case. This suggests a less effective relaxation channel in the CQR, compared to the QD case. This happens despite the much closer spacing of the ring states which should prevent the appearance of a phonon–bottleneck effect. These quite controversial considerations, linked with the puzzling large broadening of 1 meV of the PL lines, suggested us to consider a different explanation of the presented phenomena. Quantum rings, due to their rather peculiar annular shape, possess an electronic structure which is a crossover between the dot and the wire cases [60], since the linear extension of a ring of 80 nm diameter is already quite large (250 nm). Thus quantum rings can be considered as a warped analogous of quantum wires (QWi). In QWi, confinement energy fluctuations, whose magnitude is significantly lower than the exciton binding energy [150], due to QWi size disorder, take place. The presence of such disorder principally affects the exciton center of mass (COM) part of the exciton wavefunction, giving rise to states with a spatially localized COM motion. The presence of exciton COM localized states has strong effects on the optical properties of QWi, the more evident is, naturally, the inhomogeneous broadening of the emission lines, which is linked to the exciton energy disorder. In addition

to this the exciton COM localization in QWi induces a significant reduction of the phonon scattering rates [150]. At the same time, the kinetics of excitons in presence of localized states induced by disorder, is well known to produce an increase of the emission risetime associated to the exciton motion toward the state of minimum energy, in agreement with the experimental findings. The effect of the exciton COM localization on the coupling of OR and IR is twofold. On one side, excitonic COM localization partially relaxes the angular momentum conservation in exciton transitions thus making possible the coupling between the two rings. But, on the other side, by increasing the average spatial separation between the exciton states, which are localized in small regions of the rings, it strongly reduces the probability of tunneling between states belonging to OR and IR, in agreement with our experimental results.

In conclusion, we carefully analyzed the time and P_{exc} dependence of the PL emission of individual CQRs. We conclude that, despite the small spatial separation between in the two rings of the CQR complex, the carrier relaxation dynamics and the exciton kinetics in the IR and OR are decoupled. Moreover, significant increase of the emission $FWHM$ and risetime τ_R, respect to the QD case, has been observed. We attribute the observed phenomenology to the exciton COM localization induced by structural disorder along the ring.

7.3 Single photon emission of concentric quantum ring

In this section we address the question whether a quantum ring nanostructure can be considered as a single photon emitter by means of intensity time correlation measurement based on a Hanbury Brown and Twiss interferometer. In concentric quantum rings we find evidence that the inner ring satisfies the requirement of

single photon source while in the outer ring this requirement is relaxed.

Quantum mechanical phenomena in ring geometries have longly fascinated the physics community. Electrons confined in nanometric rings manifest a topological quantum interference phenomenon, known as Aharonov-Bohm effect [151]. The ground-state energy of a charged particle oscillates with the magnetic field, with an oscillation period given in unity of the magnetic quantum-flux h/e. Recently, the ability to fill the ring with few electrons has offered the possibility to experimentally detect such effect by means of the magnetic oscillation in the persistent current carried by single electron states [152]. Exciton Aharonov-Bohm effect has been predicted as well, due to the exciton non zero electric dipole moment [153]. In particular type II quantum rings have been expected to exhibit the effect due to the spatial separation of electrons and holes, as recently observed in ZnSe quantum rings [154]. On the other hand the recent success in self assembled nucleation of concentric double quantum rings (CQRs) [59] has provided suitable nanostructures for exploring the magneto-optical excitations on the basis of the Rashba spin orbit interaction [155]. Quantum ring have a peculiar and useful magnetic field level dispersion: unlike quantum dots the ground state total angular momentum changes from zero to non zero by increasing the magnetic field [156, 157]. This also results in a different energy dispersion of the excitons for different ring radius. Since charge tunneling between states of different angular momentum is strongly suppressed by selection rules, double concentric quantum rings eventually offer the control of effective coupling of direct-indirect excitons [158], which is of the utmost relevance in the research of semiconductor-based quantum computational devices.

All these fascinating phenomena consider the quantum ring as an ideal quantum system. However, to realize semiconductor quantum devices disorder cannot be neglected. Disorder related effects are largely discussed in quantum well and quantum wire literature, leading to the concept of exciton localization [159]. In

quantum dots disorder is extremely relevant in devices operating over a large ensemble of QDs: the size and shape are not fully controllable in the self assembled growth and large size dispersion is found [160]. However for each single quantum dot the carrier confinement occurs over a spatial region much smaller that the exciton Bohr radius. Therefore the disorder does not play a major role and the single QD electronic properties are well described in terms of a two level system. This is clearly demonstrated by antibunching experiments on the excitonic recombination where a $g^{(2)}(\tau = 0) = 0$ has been measured [38, 161]. In the case of quantum rings the length of the circumference is usually larger than the exciton Bohr radius and, as demonstrated for quantum wires, disorder can play a relevant role even for a single nanostructure [61].

Here we precisely address the point whether a quantum ring nanostructure can be considered as a single photon source. The experimental method is the intensity time correlation based on a Hanbury Brown and Twiss interferometer. In fact the second order correlation function $g^{(2)}$ well characterizes the quantum nature of the emitter by the presence or not of photon antibunching [161]. In concentric quantum ring (CQR) we find evidence that the inner ring satisfies the requirement of quantum emitter of single photons while in the outer ring this requirement is not fulfilled.

The experimental setup used for the correlation measurement on our $GaAs$ CQRs is the same previously described for QDs characterization (see Sect. 6.1 6.2.2). For excitation, second-harmonic output of a mode-locked Ti-sapphire laser was employed. All experiments were performed at 15 K.

Figure 7.7 reports the typical photoluminescence spectrum of an individual CQR. As mentioned before significant broadening is often measured for each line of the CQR doublet if compared with excitonic recombination in high quality MDE GaAs quantum dots (as shown in the inset of Fig.7.7). Moreover the larger value

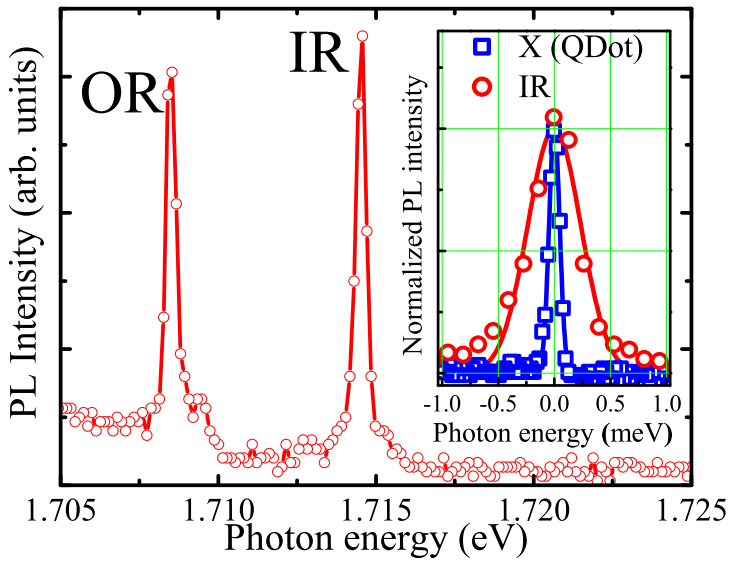

Figure 7.7: Typical PL spectrum of a CQR. The two lines labeled as IR and OR are related to excitonic emission from inner and outer ring respectively. Inset: comparison between the neutral exciton recombination (X, squares) in a GaAs QD and the inner ring exciton (IR, cicles) recombination in a CQR. The two measured linewidth (FWHM) are $110\mu eV$ and $550\mu eV$ for the QD and CQR respectively.

of the linewidth is usually associated to the OR contribution and IR line as sharp as three hundreds μeV have been measured. Let us note that even MDE QDs may sometime shows linewidth of the order of 400 μeV [58].

Typical second-order autocorrelation measurement for both the IR and OR emissions are shown in Fig.7.8 a) and Fig.7.8 b); the antibunching experiment for IR and OR was performed in the same excitation condition avoiding saturation effects or appearance of multiexciton features in the PL spectrum. The chosen spectral window was 0.8 meV to spectrally integrate each line. For each pulse the number of coincidence events for the two APDs is summarized in a histogram with 3 ns time bin, thus integrating over the overall time response of the system. The

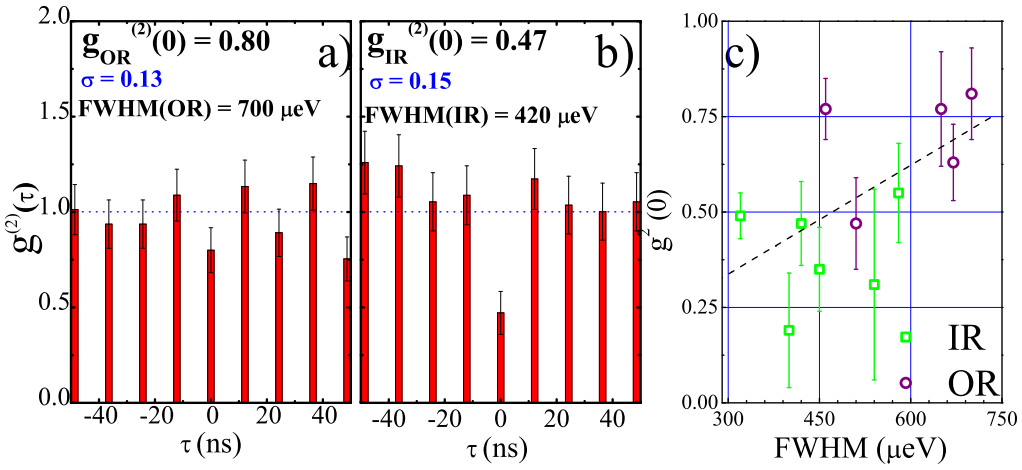

Figure 7.8: (a) and (b): pulsed excitation measurement of $g^{(2)}(\tau)$ for OR and IR respectively. The error bars associated to each peak are the coincidences count square roots normalized to the average value of the peak intensities). The error σ is the standard deviation of the average value of the peak intensity (except for the 0 delay one. c) summary of all the measured $g^{(2)}(0)$ for IR (squares) and OR (circles), the error bars are the measured σ. The black dashed line is a linear fit to data.

periodic peaks appearing at intervals of 12.2 ns indicate that photons were emitted synchronously with the pulsed excitation at 82.0 MHz. In between the PL peaks the autocorrelation value gives a precise estimate of the noise to signal ratio N/S. In particular this gives the $1-\rho^2$ value ($\rho = S/(S+N)$) to be taken into account for a correct estimate of $g^{(2)}(0)$ [161]. This experimental value has been subtracted for the data reported in Fig.7.8 a) and Fig.7.8 b).

The reduced intensity of the peak at zero time delay indicates that there is a small probability of finding more than one photon in each emitted pulse. This is the signature of a single-photon emitter under pulsed excitation. While $g^{(2)}(0) = 0$ is expected for a ideal two levels system, the condition of $g^{(2)}(0) < 0.5$ is required for a single photon emitter and the condition $g^{(2)}(0) < 1$ still denotes the quantum

Table 7.2: Broadening and $g^{(2)}(0)$ value for OR and IR of three different CQRs. Note that the OR FWHM is always larger than the IR case and $1 > g^{(2)}_{OR}(0) > 0.5 > g^{(2)}_{IR}(0)$

	CQRing1		**CQRing2**		**CQRing3**	
	OR	**IR**	**OR**	**IR**	**OR**	**IR**
$FWHM(meV)$	0.65	0.32	0.70	0.42	0.61	0.45
$g^{(2)}(0)$	0.77	0.49	0.80	0.47	0.77	0.35

nature of the emitter [27, 161]. In our case, the correlation function at zero time delay, $g^{(2)}(0)$, is estimated to be 0.47 ($\pm$0.15) for the IR recombination and 0.80 ($\pm$0.13) for the OR recombination. Note that a similar experiment performed on single QD emission provides a $g^{(2)}(0)$ estimated to be 0.18 ($\pm$0.05) without background subtraction, denoting the sensitivity of the experimental set-up. The same analysis performed on several CQRs is summarized in Fig.7.8 c) where the $g^{(2)}(0)$ is reported as a function of the line broadening. As expected the $g^{(2)}(0)$ increases with the increasing linewidth. Further we note how the condition $g^{(2)}(0) < 0.5$ is usually fulfilled by the IR but not by the OR contribution. The details of the measurement on three CQRs for which the complete set of data is available is summarized in Tab.7.2. It follows that the IR recombination systematically shows both a narrower PL lineshape and a smaller $g^{(2)}(0)$ value with respect to the OR. Note that in all cases the $g^{(2)}(0)$ value for the IR (OR) is below (above) the threshold of 0.5, which defines the single photon emitter condition. Finally crosscorrelation intensity measurements between IR and OR have been performed [not shown here] for the investigated CQRs. We always found $g^{(2)}_{IR-OR}(0) = 1$ within the experimental error. These results are not unexpected due to the independent dynamic already reported on these nanostructures [61].

The presented phenomenology poses several doubts on the possibility of using the commonly adopted picture in order to explain the PL inhomogeneous line broadening from single nanostructure.

The QDs inhomogeneous line broadening is usually ascribed to spectral diffusion (see Sect. 3.2) and PL linewidth up to several hundreds of μeV can be observed in single QD emission [58]. However this picture does imply the presence of antibunching: single QDs have been shown to be very good single photon emitters despite of their PL line broadening. The simultaneous presence of large linewidth and $g^{(2)}(0) > 0.5$ suggests that the PL line from single CQRs is an inhomogeneous collection of different individual optical transitions. Given the previously discussed analogy between CQRs and quantum wires we wont to remind that near field measurements with 150 nm resolution in quantum wires usually shows a collection of sharp peaks associated to exciton center of mass localization [160]. In analogy we expect that the disorder may produce exciton localization in different positions along the ring.

An alternative picture to the inhomogeneity of the PL lines may consist in the presence of different excitonic complexes inside the OR PL band. In fact, while trions (T) show antibunching in cross correlation measurements, biexcitons (XX) and/or multiexcitons (MX) are in bunching with the exciton recombination [38]. Therefore the collection, within the 0.8 meV experimental spectral window, of XX and MX recombination would increase the $g^{(2)}(0)$ value. In order to elucidate this point we performed PL spectra at different excitation power reported as color-intensity map in Fig.7.9. Two are the relevant points. Firstly the power dependence of both IR and OR lines is slightly sub-linear. Secondly is the appearance of two new spectral components, labeled as M1 and M2, in the high excitation regime. The two lines present a spectral shift of 3.0 and 2.9 meV from OR and IR line respectively and their power dependence is superlinear respect to the IR and OR case (see the inset reporting the PL lines intensity as a function of the incident power in Fig.7.9). Accordingly with time resolved experiments [61] we attribute M1 and M2 to XX/MX recombination associated to the OR and IR respectively.

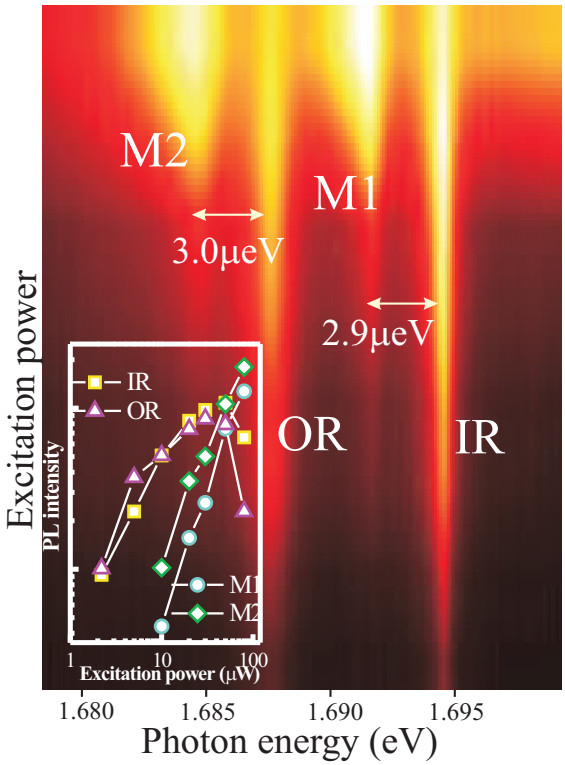

Figure 7.9: Color-intensity map of a CQR power dependence. The PL intensity varies from flat background (black) up to 16000 counts per second (white) of the M1 line. The vertical axis reports the incident power in a logarithmic scale. Inset: power dependence of the PL intensity of the four main peaks in the spectrum.

Similar behavior was reported for $GaAs/Al_{0.33}Ga_{0.67}As$ quantum wires [162]. The state filling experiment in Fig.7.9 and the time resolved analysis [61] show a saturation effect in the PL intensity and a direct transfer of charges from the excited states toward the low lying OR and IR states. These observations exclude the presence of biexciton and exciton recombination within the IR and OR lines.

We conclude that the IR is small enough to contain well separated quantum states and gives rise to an optical transition which exhibits antibunching features. On the contrary the OR is already sufficiently large to be influenced by structural disorder, resulting in an inhomogeneously broadened emission band.

Chapter 8

Final remarks

The aim of this thesis was the characterization of *GaAs/AlGaAs* nanostructures grown by modified droplet epitaxy (MDE) and test of their optical and electronic properties for application in quantum communication. From this analysis several aspects emerge. We unambiguously demonstrated the photoluminescence (PL) emission of neutral exciton X, neutral biexciton XX and charged exciton T. The unambiguous attribution relies on the different features of the intensity correlation function $g^2(\tau)$ measured trough an the Hanbury Brown and Twiss interferometer. The same experimental technique permits to evidence single photon emission from single quantum dots (QDs) [after spectral filtering] thus evidencing its potentiality as single photon emitter for quantum information processing. The time resolved and time correlated characterization point out the quantum cascade relaxation in the $XX \Rightarrow X \Rightarrow$ *ground state* transition in the QD emission which represents a milestone for the realization of a triggered source of entangled photons. Quite surprisingly we showed that, despite the lack of strain–related phenomena, the *GaAs/AlGaAs* QD system presents a relevant fine structure splitting (FSS). This was demonstrated by high resolution, polarization–resolved measurements. The additional fine interaction complicates the possibility to obtain entangled photons.

Nevertheless, the investigation of FSS in strain–free system is a good tool to clarify some aspects hardly achievable with Stranski–Krastanov nanostructures (role of geometrical anisotropy, role of extrinsic effects). Further we precisely addressed the question of the exciton–phonon interaction by CW (measuring the line shape and broadening) and time resolved experiments (measuring the radiative lifetime). We unambiguously demonstrated the common nature of the *zero phonon line* and of the *phonon sidebands* fulfilling the theoretical predictions of the commonly accepted Independent Boson Model of the *polaronic effect*. The other relevant aspect of the line broadening of the QD emission here studied was the spectral diffusion (SD) coming from the charged fluctuating environment. We measured the SD–induced broadening showing that the X linewidth is typically larger than the XX and T linewidths, thus reflecting the different degree of polarizability of X, XX, and T states. The theoretical investigation showed that the spectral shift of the different excitonic complexes can be nicely explained in term of *quantum confined Stark shift* due to charged traps in the QD proximity.

Concentric quantum rings (CQRs) are in principle, very promising nanostructures for exploring coupled electronic states and the investigation of the CQR system presented here by means of time resolved and time correlated measurements, exactly addresses this point. We showed that the exciton dynamics of the two rings are completely decoupled due to the small tunneling probability, as can be evaluated by using an effective mass model. Further we showed that the external ring is more likely a warped analogue of a quantum wire since it's photoluminescence broadening can be nicely explained as originated by a collection of inhomogeneously broadened localized states. On the contrary we found that the inner ring is small enough to contain a single quantum state since we can determine a $g^2(0) < 0.5$. This is particularly important since the ring–shaped nanostructure, in contrast to the QD case, makes possible the investigation, and eventually the

exploitation, of peculiar quantum phenomena such as Aharonov–Bohm effect.

Appendices

Second order correlation function: a theoretical overview

In the following Appendix the major issues related to the second order correlation function are shortly introduced. Some theoretical aspects of the $g^{(2)}$ function are reviewed as a guide for the interpretation of the experimental results presented in Chapter 6 and 7.3 of this). For a complete and exhaustive treatment of this argument we refer to Ref. [27].

8.1 Intensity correlation: second order coherence of quantum field

The coherence properties of an electromagnetic field can be described by the correlation of the field amplitude (first order coherence) or field intensity (second order coherence) and are usually described by the corresponding correlation functions $g^{(1)}$ and $g^{(2)}$ [27]. A striking point of these properties is their behavior in the classical or in the quantum approximation. In the case of the first order coherence the $g^{(1)}$ does not show any difference in the two approximations, while the investigation of the $g^{(2)}$ is a good way to point out the quantum feature of a photon source. Further, the measurement of $g^{(2)}$ function has been recognized as an es-

sential tool for the spectroscopic characterization of semiconductor nanostructure optical properties. In fact the investigation of $g^{(2)}$ function can be exploited in order to test the capability of these nanoemitters as suitable building blocks for the realization of single and entangled photons pairs emitters.

Hereafter a brief theoretical treatment of the second order correlation function $g^{(2)}$ in the quantum approximation for a two and three level atomic-like system is given [27].

The general expression of the electric field instantaneous intensity correlation function is:

$$g^{(2)}(\mathbf{x}, \Delta\mathbf{x}; t, \tau) = \frac{\langle I(\mathbf{x}, t) I(\mathbf{x} + \Delta\mathbf{x}, t + \tau)\rangle}{\langle I(\mathbf{x}, t)\rangle^2} \tag{8.1}$$

where $I(\mathbf{x}, t) = |\mathbf{E}(\mathbf{x}, t)|^2$ represents the field intensity being $\mathbf{E}(\mathbf{x}, t)$ the expression of the electric field at the spatial position $\mathbf{x}$ and time t; $\Delta\mathbf{x}$ and τ represent a spatial shift and a time delay, respectively.

Here we take into account the time dependence of the $g^{(2)}$ function neglecting its dependence on $\mathbf{x}$. Introducing the expression of the electric field in the quantum approximation by using the appropriate operators in the Heisenberg representation, the second order correlation function for a stationary field is given by:

$$g^{(2)}(\tau) = \frac{\langle \hat{\mathbf{E}}^{-}(t)\hat{\mathbf{E}}^{-}(t+\tau)\hat{\mathbf{E}}^{+}(t)\hat{\mathbf{E}}^{+}(t+\tau)\rangle}{\langle \hat{\mathbf{E}}^{-}(t)\hat{\mathbf{E}}^{+}(t)\rangle^2} \tag{8.2}$$

where:

$$\langle \hat{\mathbf{E}}^{-}(t)\hat{\mathbf{E}}^{+}(t)\rangle = Tr(\hat{\rho}\hat{\mathbf{E}}^{-}(t)\hat{\mathbf{E}}^{+}(t)) \tag{8.3}$$

is the expectation value of the observable between parentheses being $\hat{\rho}$ the density matrix operator of the system and Tr the operation of $Trace$. The operators $\hat{\mathbf{E}}^{\pm}(t)$

for an electromagnetic field in vacuum are:

$$\hat{\mathbf{E}}^{-}(t) = -i \sum_{k} \sqrt{\frac{\hbar\omega_k}{2\epsilon_0 V}} \overrightarrow{\varepsilon}_k \hat{a}_k e^{i\omega_k t} \tag{8.4}$$

$$\hat{\mathbf{E}}^{+}(t) = i \sum_{k} \sqrt{\frac{\hbar\omega_k}{2\epsilon_0 V}} \overrightarrow{\varepsilon}_k \hat{a}_k^{\dagger} e^{-i\omega_k t} \tag{8.5}$$

where the k is the index of each mode of the field, V the volume of quantization, ω_k the frequency of the mode, $\overrightarrow{\varepsilon}_k$ the polarization vector, $\hat{a}_k$ and $\hat{a}_k^{\dagger}$ the operators for annihilation and creation of one photon in mode k.

It can be showed that in the classical limit the following relations hold:

$$g^{(2)}(\tau) \leq g^{(2)}(0) \tag{8.6}$$

$$1 \leq g^{(2)}(0) \leq +\infty \tag{8.7}$$

$$g^{(2)}(\tau) = g^{(2)}(-\tau) \tag{8.8}$$

while in the quantum case of Eq. 8.2 the interval of values assumed by $g^{(2)}(0)$

$$0 \leq g^{(2)}(0) < 1 \tag{8.9}$$

is allowed and the inequality in Eq. 8.6 is not still valid.

The shape of the $g^{(2)}(\tau)$ can be obtained both analytically and experimentally for different kind of light sources [27]. For example a classical chaotic photon source shows a $g^{(2)}(\tau)$ that fulfill the inequality in Eq. 8.6 [163]. This behavior is indicated as *photon bunching* and accounts for the tendency of the photons to group themselves in time bunches. Quantum light source may instead present the opposite behavior showing a *photon antibunching* fulfilling the inequality of Eq. 8.9. This is the signature that at short time delays the detected photon number is

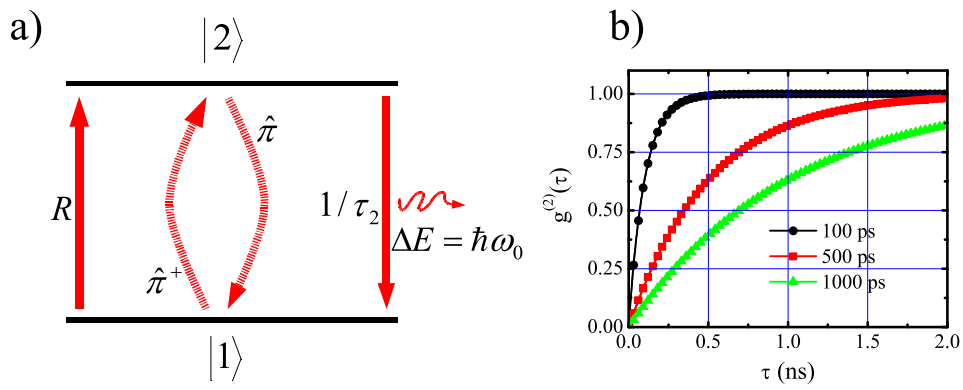

Figure 8.1: (a) Two level system. The excited state $|2\rangle$ is populated by a constant pump **R** and decay toward the low lying level $|1\rangle$ with a lifetime τ_2 emitting a photon with energy $\Delta E = \hbar\omega_0$. The operator $\hat{\pi}^\dagger$ ($\hat{\pi}$) of the transition applied to the state $|1\rangle$ ($|2\rangle$) lead the system in the state $|2\rangle$ ($|1\rangle$). (b) $g^{(2)}(\tau)$ for a two level system with different lifetimes τ_2

smaller than the one measured at longer delay.

8.2 Multimode emission of a two level system

In this section the second order correlation function is studied for an ideal two level system involving an electronic transition (i.e. a single atomic transition [27] or also a QD excitonic transition as shown in Fig. 8.1). The emitted photons have a definite energy determined by the energy difference between the two levels: $\Delta E = \hbar\omega_0$.

Assuming a constant rate R populating the higher energy level $|2\rangle$, under the condition of low excitation regime ($R \ll 1/\tau_2$), the second order correlation function $g^{(2)}(\tau)$ can be obtained by using Eq. 8.2.

The first step is to obtain the time dependence of the creation/annihilation operators $\hat{a}_k^\dagger(t)/\hat{a}_k(t)$ appearing in the field operators defined in Eq.s 8.4 and 8.5. The time evolution of a generic observable $\hat{\mathbf{O}}_H$ of a quantum system in the Heisemberg

representation is described by the commutator:

$$i\hbar\frac{\hat{\mathbf{O}}_H(t)}{dt} = [\hat{\mathbf{O}}_H(t), \hat{H}] \tag{8.10}$$

where $\hat{H}$ is the system hamiltonian described by:

$$\hat{H} = \hbar\omega_0\hat{\pi}^\dagger(t)\hat{\pi}(t) + \sum_k \hbar\omega_k\hat{a}_k^\dagger(t)\hat{a}_k(t) + i\sum_k \hbar\xi_k\{\hat{\pi}^\dagger(t)\hat{a}_k(t)e^{i\mathbf{kR}} - \hat{\pi}(t)\hat{a}_k^\dagger(t)e^{-i\mathbf{kR}}\} \tag{8.11}$$

The first term represents the two level system hamiltonian. In this part the two operators $\hat{\pi}^\dagger(t)$ and $\hat{\pi}(t)$ define the transition $|1\rangle \Leftrightarrow |2\rangle$ with the following rules:

$$\hat{\pi}^\dagger(0) = |2\rangle\langle 1| \tag{8.12}$$

$$\hat{\pi}(0) = |1\rangle\langle 2| \tag{8.13}$$

for these operators also the following properties hold:

$$\hat{\pi}^\dagger\hat{\pi}^\dagger = 0 \tag{8.14}$$

$$\hat{\pi}\hat{\pi} = 0 \tag{8.15}$$

The second term in Eq. 8.11 represents the electromagnetic hamiltonian in free space, while the third term is interaction term between the field and the two level system in the dipole approximation. $\mathbf{R}$ is spatial position and ξ_k is given by:

$$\xi_k = e\frac{\omega_k}{2\epsilon_0\hbar V}\overrightarrow{\varepsilon}_k \cdot \langle 1|\hat{\mathbf{D}}|2\rangle \tag{8.16}$$

where $\hat{\mathbf{D}}$ represents the dipole operator. The time dependence of the different operators in the Heisemberg representation can be obtained through equation 8.10. The presence of the interaction term complicates the time dependence of the op-

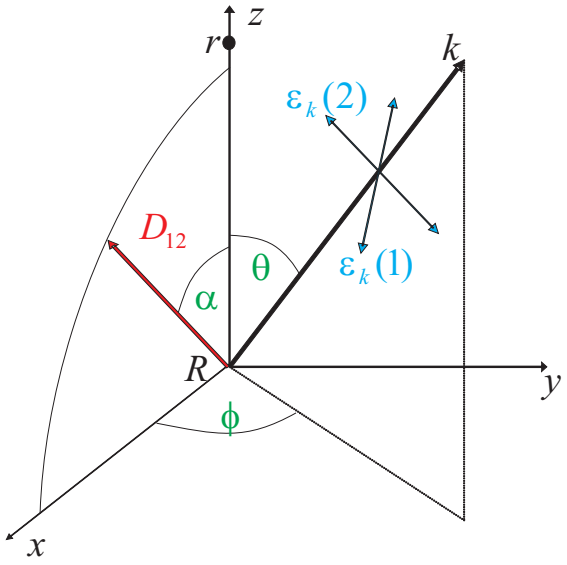

Figure 8.2: Orientation of the vectors used in the evaluation of the electric field at **r** produced by radiation from an atom at **R**

erators $\hat{\pi}(t)$, $\hat{\pi}^{\dagger}(t)$, $\hat{a}_k(t)$ and $\hat{a}_k^{\dagger}(t)$ couple them. The expression for the E^+ (or in analogy for E^-) can be obtained from Eq. 8.5 including the time dependence in $\hat{a}_k$:

$$\hat{\mathbf{E}}^+(\mathbf{r}t) = i\sum_k \sqrt{\frac{\hbar\omega_k}{2\epsilon_0 V}}\overrightarrow{\varepsilon}_k \hat{a}_k(t)e^{i\mathbf{k}\cdot\mathbf{r}} \tag{8.17}$$

In the dipole approximation ($k|\mathbf{r}-\mathbf{R}| \gg 1$), assuming an isotropic emission of the two level system and imposing the energy conservation ($\omega = \omega_0$) it is possible to integrate over all the directions $\mathbf{k}$ of the emitted photons, obtaining:

$$\hat{\mathbf{E}}^+(\mathbf{r},t) = -\frac{e\omega_0 D_{12} sin\alpha}{4\pi\epsilon_0 c^2|\mathbf{r}-\mathbf{R}|}\varepsilon\hat{\pi}(t-\frac{|\mathbf{r}-\mathbf{R}|}{c}) \tag{8.18}$$

This expresses the field at point $\mathbf{r}$ in terms of the dipole operator of the radiating source atom [see Fig. 8.2]. In order to simplify the problem is possible to introduce some other approximations:

- we only consider the emitted radiation polarized along ε

- we assume stationary condition also neglecting the time shift $\frac{|\mathbf{r}-\mathbf{R}|}{c}$

Introducing the simplified expression of the field operators in the expression for the $g^{(2)}(\tau)$ Eq. 8.2 we obtain:

$$g^{(2)}(\tau) = \frac{\langle \hat{\pi}^\dagger(t)\hat{\pi}^\dagger(t+\tau)\hat{\pi}(t+\tau)\hat{\pi}(t)\rangle}{\langle \hat{\pi}^\dagger(t)\hat{\pi}(t)\rangle^2} \tag{8.19}$$

Due to the time reversal condition (Eq. 8.8) we will refer in the following to positive τ. It is then convenient to use in the following the interaction representation for $\hat{\pi}^\dagger(t)$ and $\hat{\pi}(t)$

For a simpler calculation is possible to change the representation of the quantum operators in their interaction representation where they are decoupled:

$$\hat{\pi}^\dagger(t) = \hat{\pi}^\dagger(0)e^{i\omega_0 t} \tag{8.20}$$

$$\hat{\pi}(t) = \hat{\pi}(0)e^{-i\omega_0 t} \tag{8.21}$$

By using these expressions and using the density matrix is possible to show that:

$$\langle \hat{\pi}^\dagger(t)\rangle = \rho_{21}e^{i\omega_0 t} \tag{8.22}$$

$$\langle \hat{\pi}(t)\rangle = \rho_{12}e^{-i\omega_0 t} \tag{8.23}$$

$$\langle \hat{\pi}^\dagger(t)\hat{\pi}(t)\rangle = \rho_{22}(t) \tag{8.24}$$

where ρ_{ij} are density matrix elements, which can be obtained by the appropriate rate equations. Note that the density matrix elements are not fully independent, in fact the following relations hold: $\rho_{11} + \rho_{22} = 1$ and $\rho_{12}(t) = \rho_{12}^*(t)$ which result in only three independent coefficients.

Since the above expressions involve only a single time t is necessary to generalize

them for any delay $t+\tau$ as follows:

$$\langle\hat{\pi}(t+\tau)\rangle e^{-i\omega_0 t+\tau} = \rho_{21}(t+\tau) = \alpha_1(\tau) + \alpha_2(\tau)\rho_{21}(t) + \alpha_3(\tau)\rho_{12}(t) + \alpha_4(\tau)\rho_{22}(t) \tag{8.25}$$

$$\langle\hat{\pi}^\dagger(t+\tau)\hat{\pi}(t+\tau)\rangle = \rho_{22}(t+\tau) = \beta_1(\tau) + \beta_2(\tau)\rho_{21}(t) + \beta_3(\tau)\rho_{12}(t) + \beta_4(\tau)\rho_{22}(t) \tag{8.26}$$

where the time dependent coefficients α_i and β_i have been introduced. The expressions in Eq.8.19 can be calculated by using the *quantum regression theorem* hereafter reported.

If an operator $\widehat{A}$ can be decomposed as follows:

$$\langle\hat{A}(t+\tau)\rangle = \sum_i \alpha_i(\tau)\langle\hat{A}_i(t)\rangle \tag{8.27}$$

than it is possible to demonstrate that the following relation holds for any operators $\hat{B}(t)$ and $\hat{C}(t)$:

$$\langle\hat{B}(t)\hat{A}(t+\tau)\hat{C}(t)\rangle = \sum_i \alpha_i(\tau)\langle\hat{B}(t)\hat{A}_i(t)\hat{C}(t)\rangle \tag{8.28}$$

The numerator of the expression in Eq.8.19 can be expressed as the left term of Eq. 8.29 assuming $\hat{A}(t+\tau) \equiv \hat{\pi}^\dagger(t+\tau)\hat{\pi}(t+\tau)$ and $\hat{B}^\dagger(t) \equiv \hat{\pi}(t)$. By applying 8.29 taking into account Eq.s 8.26 and relations 8.22, 8.23, 8.24 we obtain:

$$\begin{aligned}\langle\hat{\pi}^\dagger(t)\hat{\pi}^\dagger(t+\tau)\hat{\pi}(t+\tau)\hat{\pi}(t)\rangle &= \beta_1(\tau) + \beta_2(\tau)\langle\pi^\dagger(t)\hat{\pi}^\dagger(t)\hat{\pi}(t)\rangle + \\ &+ \beta_3(\tau)\langle\pi^\dagger(t)\hat{\pi}(t)\hat{\pi}(t)\rangle + \\ &+ \beta_4(\tau)\langle\pi^\dagger(t)\hat{\pi}^\dagger(t)\hat{\pi}(t)\hat{\pi}(t)\rangle\end{aligned}$$

using the properties of the operators $\hat{\pi}$ and $\hat{\pi}^\dagger$ of Eq. 8.14 and 8.15 we obtain:

$$\frac{\langle \hat{\pi}^\dagger(t)\hat{\pi}^\dagger(t+\tau)\hat{\pi}(t+\tau)\hat{\pi}(t)\rangle}{\langle \hat{\pi}^\dagger(t)\hat{\pi}(t)\rangle^2} = \frac{\beta_1(\tau)}{\rho_{22}(t)} \tag{8.29}$$

considering the steady value of $\rho_{22}(t)$ we have:

$$g^{(2)}(\tau) = \lim_{t\to+\infty} \frac{\beta_1(\tau)}{\rho_{22}(t)} \tag{8.30}$$

The two terms $\beta_1(\tau)$ and $\rho_{22}(t)$ can be obtained from the rate equation (seeFig.8.1):

$$\frac{d\rho_{22}}{dt} = R - \frac{\rho_{22}}{\tau_2} \tag{8.31}$$

The solution is:

$$\rho_{22}(t) = R \cdot \tau_2(1 - e^{-\frac{t}{\tau_2}}) \tag{8.32}$$

For steady stationary condition we then obtain $\rho_{22}(\infty) = R \cdot \tau_2$. The expression in Eq. 8.32 can be evaluated at a time $t + \tau$:

$$\rho_{22}(t+\tau) = R \cdot \tau_2(1 - e^{-\frac{\tau}{\tau_2}}) + \rho_{22}(t)e^{-\frac{\tau}{\tau_2}} \tag{8.33}$$

which allows to obtain the expression for $\beta_1(\tau)$:

$$\beta_1(\tau) = R \cdot \tau_2(1 - e^{-\frac{\tau}{\tau_2}}) \tag{8.34}$$

We can finally obtain the explicit expression for the $g^{(2)}(\tau)$:

$$g^{(2)}(\tau) = 1 - e^{-\frac{\tau}{\tau_2}} \tag{8.35}$$

The function described in Eq.8.35 is plotted in Fig.8.1 (b) for different lifetimes τ_2. The plot points out the antibunching behavior of $g^{(2)}(\tau)$ and that $g^{(2)}(0) = 0$.

8.3 Three level system: correlated photons

Another important process considered here is the photon emission from a three level system, shown in Fig.8.3. This system is typical of some atomic system and, as shown in Chapter 6, can be used to interpret the radiative process of the biexciton–>exciton cascade in quantum dot nanostructures. The system is schematized as three energy level $|1\rangle$, $|2\rangle$ and $|3\rangle$, which energy are E_1, E_2 and E_3, respectively. Here we fix $E_1 = 0$ as ground state of the system. The constant pump $\mathbf{R}$ transfers the population of the level $|1\rangle$ to the excited state $|3\rangle$. This excited level decays with a lifetime τ_3 toward the level $|2\rangle$ emitting a photon of energy $\hbar\omega_{32} = E_3 - E_2$. The level $|2\rangle$ decay toward the ground state $|1\rangle$ with a radiative lifetime τ_2 emitting a photon with energy $\hbar\omega_{21} = E_2 - E_1$. In this case the electromagnetic fields is the result of the overlap of the two field produced in the two distinct radiative transitions. Hereafter we study the autocorrelation functions for each single transition $g^{(2)}_{22}$, $g^{(2)}_{33}$ and the cross-correlation function $g^{(2)}_{32}$ of the two fields. The generic expression of the (auto/cross)correlation function can be written as follows:

$$g^{(2)}_{ij}(\tau) = \frac{\langle \hat{\mathbf{E}}^-_i(t)\hat{\mathbf{E}}^-_j(t+\tau)\hat{\mathbf{E}}^+_j(t)\hat{\mathbf{E}}^+_i(t+\tau)\rangle}{\langle \hat{\mathbf{E}}^-_i(t)\hat{\mathbf{E}}^+_i(t)\rangle\langle \hat{\mathbf{E}}^-_j(t)\hat{\mathbf{E}}^+_j(t)\rangle} \tag{8.36}$$

In the present case the two coefficients i and j can take the values 2 and 3 and they are referred to the corresponding states $|2\rangle$ and $|3\rangle$. Note that from the definition follows that $g^{(2)}_{ij}(\tau) = g^{(2)}_{ji}(-\tau)$.

Extending the treatment made for the two levels system to the present case, it is possible to obtain the expression in Eq. 8.36 as a function of the quantum

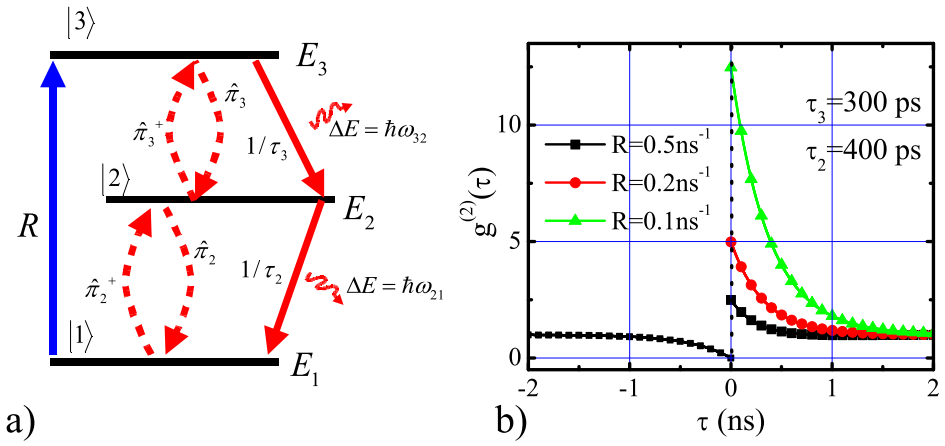

Figure 8.3: (a) Three level system scheme. The radiative process involve the pump mechanism **R** from the ground state $|1\rangle$ to the excited state $|3\rangle$ and the optical transition $|1\rangle \Leftrightarrow |2\rangle \Leftrightarrow |3\rangle$. (b) $g^2_{32}(\tau)$ for different pump rate **R**

operators of the atomic system

$$g^{(2)}(\tau) = \frac{\langle \hat{\pi}_i^\dagger(t)\hat{\pi}_j^\dagger(t+\tau)\hat{\pi}_j(t+\tau)\hat{\pi}_i(t)\rangle}{\langle \hat{\pi}_i^\dagger(t)\hat{\pi}_i(t)\rangle\langle \hat{\pi}_j^\dagger(t)\hat{\pi}_j(t)\rangle} \tag{8.37}$$

where the quantum operators at $t = 0$ are defined as follows:

$$\hat{\pi}_3^\dagger(0) = |3\rangle\langle 2|,\ \hat{\pi}_3(0) = |2\rangle\langle 3|;\ \hat{\pi}_2^\dagger(0) = |2\rangle\langle 1|,\ \hat{\pi}_2(0) = |1\rangle\langle 2| \tag{8.38}$$

Since for the expectation value of product of operators $\hat{\pi}_i^\dagger(t+\tau)\hat{\pi}_i(t+\tau)$ the hypothesis of Eq. 8.27 still holds we can apply the *quantum regression theorem.*

By using a similar to derivation to those shown in Eq.s 8.25 and 8.26 we can obtain:

$$\begin{aligned}\rho_{22}(t+\tau) = \alpha_1(\tau) + \alpha_2(\tau)\rho_{12}(t) + \alpha_3(\tau)\rho_{21}(t) + \\ + \alpha_4(\tau)\rho_{22}(t) + \alpha_5(\tau)\rho_{23}(t) + \\ + \alpha_6(\tau)\rho_{32}(t) + \alpha_7(\tau)\rho_{33}(t)\end{aligned} \tag{8.39}$$

$$\begin{aligned}\rho_{33}(t+\tau) = \beta_1(\tau) + \beta_2(\tau)\rho_{12}(t) + \beta_3(\tau)\rho_{21}(t) + \\ + +\beta_4(\tau)\rho_{22}(t) + \beta_5(\tau)\rho_{23}(t) + \\ + \beta_6(\tau)\rho_{32}(t) + \beta_7(\tau)\rho_{33}(t)\end{aligned} \tag{8.40}$$

The density matrix elements are bound to the expectation values of the three levels system operators by relation similar to Eq.s 8.22, 8.23 and 8.24. It is then possible to calculate the expectation values:

$$\langle \hat{\pi}_2^\dagger(t)\hat{\pi}_2^\dagger(t+\tau)\hat{\pi}_2(t+\tau)\hat{\pi}_2(t)\rangle = \alpha_1(\tau)\rho_{22}(t) \tag{8.41}$$

$$\langle \hat{\pi}_3^\dagger(t)\hat{\pi}_3^\dagger(t+\tau)\hat{\pi}_2(t+\tau)\hat{\pi}_3(t)\rangle = \beta_1(\tau)\rho_{33}(t) \tag{8.42}$$

$$\langle \hat{\pi}_2^\dagger(t)\hat{\pi}_3^\dagger(t+\tau)\hat{\pi}_3(t+\tau)\hat{\pi}_2(t)\rangle = \beta_1(\tau)\rho_{22}(t) \tag{8.43}$$

$$\langle \hat{\pi}_3^\dagger(t)\hat{\pi}_2^\dagger(t+\tau)\hat{\pi}_2(t+\tau)\hat{\pi}_3(t)\rangle = (\alpha_1(\tau) + \alpha_4(\tau))\rho_{33}(t) \tag{8.44}$$

In steady state conditions, the the density matrix elements and the τ dependent coefficients can be obtained by the rate equations of the system shown in Fig. 8.3 (a):

$$\frac{d\rho_{33}(t)}{dt} = R - \frac{\rho_{33}}{\tau_3} \tag{8.45}$$

$$\frac{d\rho_{22}(t)}{dt} = \frac{\rho_{33}}{\tau_3} - \frac{\rho_{22}}{\tau_2} \tag{8.46}$$

$$\frac{d\rho_{11}(t)}{dt} = \frac{\rho_{22}}{\tau_2} - R \tag{8.47}$$

These three equations are not completely independent and their sum gives:

$$\rho_{33}(t) + \rho_{22}(t) + \rho_{11}(t) = constant \tag{8.48}$$

of the others.

The three rate equations well describe the three levels system in the hypothesis of low pumping regime far from saturation ($R(\tau_2 + \tau_3) \ll 1$). The stationary solutions are:

$$\rho_{22}(t) = R \cdot \tau_2, \ \rho_{33}(t) = R \cdot \tau_3 \tag{8.49}$$

With the initial condition $\rho_{33}(0) = 1$ and $\rho_{22}(0) = \rho_{11}(0) = 0$ it is possible to find the general solutions:

$$\rho_{33}(t+\tau) = R \cdot \tau_3[1 - e^{-\frac{\tau}{\tau_3}}] + \rho_{33}(t)e^{-\frac{\tau}{\tau_3}} \tag{8.50}$$

$$\rho_{22}(t+\tau) = \frac{R \cdot \tau_2[\tau_3(1 - e^{-\frac{\tau}{\tau_3}}) - \tau_2(1 - e^{-\frac{\tau}{\tau_2}})]}{\tau_3 - \tau_2} + \tag{8.51}$$

$$+ \rho_{22}(t)e^{-\frac{\tau}{\tau_2}} - \rho_{33}(t)\frac{\tau_2(e^{-\frac{\tau}{\tau_2}} - e^{-\frac{\tau}{\tau_3}})}{\tau_3 - \tau_2} \tag{8.52}$$

By using the results in Eq.s 8.49, 8.50 and 8.51 it is possible to determine all the elements necessary to calculate the expectation values in 8.41, 8.42 and 8.43 and finally obtain four auto– and cross–correlation functions:

$$g_{33}^{(2)}(\tau) = g_{23}^{(2)}(\tau) = 1 - e^{-\frac{\tau}{\tau_3}} \tag{8.53}$$

$$g_{22}^{(2)}(\tau) = \frac{\tau_3(1-e^{-\frac{\tau}{\tau_3}}) - \tau_2(1-e^{-\frac{\tau}{\tau_2}})}{\tau_3 - \tau_2} \tag{8.54}$$

$$g_{32}^{(2)}(\tau) = g_{22}^{(2)}(\tau) + \frac{1}{R \cdot \tau_2} \cdot e^{-\frac{\tau}{\tau_2}} \tag{8.55}$$

The functions $g_{33}^{(2)}(\tau)$ and $g_{22}^{(2)}(\tau)$ represent the autocorrelation function of the radiation field associated to each specific transition and in analogy with the case of the two levels system they show an antibunched behavior.

The complete form of the $g_{32}^{(2)}(\tau)$ can be obtained using the property $g_{ij}^{(2)}(\tau) = g_{ji}^{(2)}(-\tau)$:

$$g_{32}^{(2)}(\tau) = \begin{cases} 1 - e^{-\frac{\tau}{\tau_3}} & \tau < 0 \\ \frac{\tau_3(1-e^{-\frac{\tau}{\tau_3}}) - \tau_2(1-e^{-\frac{\tau}{\tau_2}})}{\tau_3 - \tau_2} + \frac{1}{R \cdot \tau_2} \cdot e^{-\frac{\tau}{\tau_2}} & \tau > 0 \end{cases} \tag{8.56}$$

An example of the $g_{32}^{(2)}(\tau)$ is displaced in Fig.8.3 (b) for three different pumping rates R. The marked bunched behavior of the cross-correlation function is a signature of the high probability of the emission of a photon $\hbar\omega_{21}$ after the emission of a photon $\hbar\omega_{32}$. We note that the bunched behavior of the $g_{32}^{(2)}(\tau > 0)$ increases if the the second term $R\tau_2$ increases. In other words, the bunching peak is more pronounced for low pumping regime of the upper level [for a review of the saturation effect see Ref. [146, 164]]. The first term shows an antibunching behavior and may influence the shape of the intensity cross-correlation function in the case of $\tau_3 > \tau_2$ and high pumping rate, producing an antibunched behavior. For $\tau < 0$ we observe an single exponential antibunching behavior ruled by the lifetime τ_3, reflecting the small probability to observe a $\hbar\omega_{21}$ before the emission of a photon $\hbar\omega_{32}$.

An example of these considerations can be found in Section 6.2.2 where the $g_{32}^{(2)}(\tau)$ function is measured for the biexciton –> exciton cascade.

Experimental determination of the second order correlation function

In the following Appendix a brief review of the $g^{(2)}$ function measurement is given. Firstly we show that the signal measured by the Hanbury Brown and Twiss interferometer reproduces the $g^{(2)}(\tau)$. Secondly the effect of the instrumental response is taken into account.

8.4 Hanbury Brown and Twiss interferometer and $g^{(2)}$ function measurement

The Hanbury brown and Twiss interferometer HBT has been described in Section 2.2.1. We refer to (Fig. 2.5 (a)) for the interferometer scheme and to Fig. 2.5 (b) the measurement procedure .

The experimental apparatus allows the collection of the photoluminescence from single nanostructures and produces a collimate beam which is fed into the HBT setup. We don't consider here photons losses, but we remind that we always assume to work in single photon counting regime (low detection efficiency).

The time delays measured through the TAC (see Section 2.2.1) are converted in logic signals through a 14 bit ADC which produces a discrete time scale (T_{ch} is the time interval associated to each ADC channel and it can be determined through a tarature with a pulsed laser source). The histogram realized through the detection of START–STOP events (reported as counts in the corresponding ADC channel) over the integration time of the measure is the correlation function $C^2_{21}(\tau)$ of the filtered field with frequency ω_2 and ω_1 [145, 38] and is given by:

$$C^{(2)}_{21}(\tau) = \int_{-T_{ch}/2}^{T_{ch}/2} \int_{T_0}^{T_F} n_{\omega_1}(t) n_{\omega_2}(t + t' + \tau) dt dt' \tag{8.57}$$

where n_{ω_1} and n_{ω_2} are the photon fluxes at the two frequencies (n_{ω_2} are the delayed photons). The first integration over $t^{'}$ is extended over the channel interval T_{ch} while the integral in t is extended over all the measurement integration time (starting at T_0 and ending at T_F). In stationary condition $C^{(2)}_{21}(\tau)$ does not depend on the specific time of the measurement and it results proportional to the $g^{(2)}_{21}(\tau)$ function through a normalization factor:

$$g^{(2)}_{21}(\tau) = \frac{C^{(2)}_{21}(\tau)}{\overline{n}_{\omega_2} \overline{n}_{\omega_1} T_{ch} T_M} \tag{8.58}$$

where $\overline{n}_{\omega_1}$ and $\overline{n}_{\omega_2}$ are the mean photons number and $T_M = T_F - T_0$ is the measurement time. The expression in Eq. 8.58 holds in the limit low photon detection efficiency.

For details on the $g^{(2)}$ measurement under pulsed excitation and the related saturation effects we remind to the literature [146, 164, 165]. In order to get the measured signal, the expression in Eq. 8.58 must be also convoluted with the instrumental response. In fact, as evident in the case of CW measurement of the $g^{(2)}(\tau)$ function of Fig. 6.3 the limited time resolution does not allow to reveal a $g^{(2)}(\tau = 0) = 0$. In fact, in our case, the exciton lifetime [$\tau_{rad} \simeq 400ps$] is usually

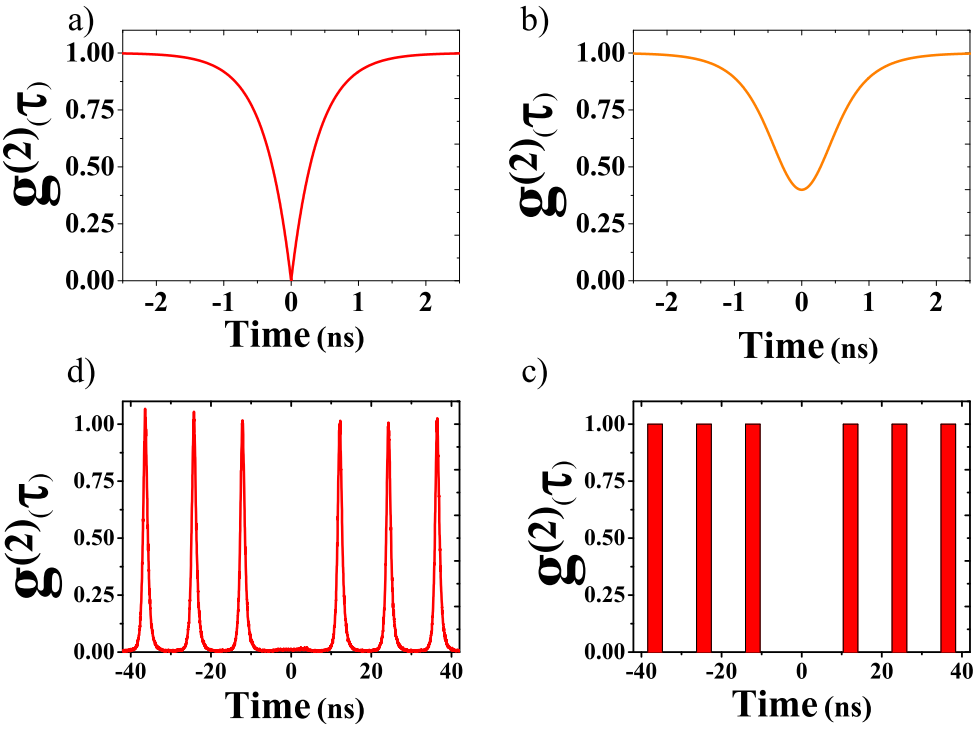

Figure 8.4: (a) theoretical $g^{(2)}(\tau)$ function for a two level system which lifetime is 400 ps under CW excitation. (b) effect of the instrumental response on the $g^{(2)}(\tau)$ of graph (a). The instrumental time response is assumed to be a gaussian profile with a $FWHM$ of 300 ps. (c) theoretical $g^{(2)}(n\tau)$ function under pulsed excitation (repetition rate: 82 MHz). (d) time binning of the $g^{(2)}(n\tau)$ of graph (c). The red columns have the same area of the bunching peak in graph (c).

comparable with the time response of our HBT apparatus [$\tau_{exp} \simeq 600ps$]. As an example we report in Fig. 8.4 (a) the $g^{(2)}(\tau)$ measured with an ideal detector and in (b) the $g^{(2)}(\tau)$ convoluted with a gaussian profile (standard deviation 300 ps) which approximate the time response of the detectors. The advantage of a CW respect to the pulsed excitation measurement is a complete reconstruction of the $g^{(2)}(\tau)$ which for example allows to determine the radiative lifetime of the recombination processes involved. The price to be paid is that the direct determination of $g^{(2)}(0)$ is not allowed.

In Fig. 8.4 (c) the $g^{(2)}(nT)$ is reported for pulsed excitation in the case of an ideal detector. The time displacement and the shape of the bunching peaks for $nT \neq 0$ provide information on the recombination process and on the lifetime of the transitions involved [145, 38]. That kind of measurement permits a direct determination of the $g^{(2)}(0)$ value avoiding the drawbacks related to the temporal response convolution. In fact when the instrumental response is introduced we observe a broadening of the bunching peaks for $nT \neq 0$. Nevertheless the area of each bunching peak in the ideal and non–ideal detector case still remain the same. This is of the utmost importance since it means that the value of $g^{(2)}(nT = 0)$ is not changed by the instrumental response.

List of publications

- **Carrier dynamics and recombination in GaN quantum discs embedded in AlGaN nanocolumns**

  M. Zamfirescu, M. Abbarchi, M. Gurioli, A. Vinattieri, J. Ristic, and E. Calleja.

  phys. stat. sol. (c) 2, No. 2, 822.825 (2005)

- **Recombination lifetime of single GaAs/AlGaAs quantum dots**

  M. Abbarchi, M. Gurioli, S. Sanguinetti, M. Zamfirescu, A. Vinattieri, N. Koguchi

  phys. stat. sol. (c) 3, No. 11, 3860,3863 (2006)

- **Temperature dependence of the photoluminescence of single GaAs/AlGaAs concentric quantum ring structure**

  M. Bonfanti , S. Sanguinetti, T. Mano, T. Kuroda, M. Gurioli, M. Abbarchi,E. Grilli, and N. Koguchi

  phys. stat. sol. (c) 3, No. 11, 3856,3859 (2006)

- **Emission lineshape in strain free quantum dot**

  E. Poliani, M.Bonfanti, S. Sanguinetti, E. Grilli, M. Guzzi, M. Gurioli, M. Abbarchi, and N. Koguchi.

  phys. stat. sol. (c) 3, No. 11, 3819,3822 (2006)

- **Exciton and multiexciton dynamics in single GaAs/AlGaAs quantum dots**

  M. Abbarchi, M. Gurioli, A. Vinattieri, M. Zamfirescu, S. Sanguinetti and N. Koguchi.

  in: *Beam injection based nanocharacterization of advanced materials*, ed. by G. Salviati, T. Sekiguchi, S. Heun, and A. Gustafsson, Research Signpost (in press)

- **Magneto-photoluminescence study in single GaAs/AlGaAs self assembled quantum dot**

  M. Abbarchi, T. Kuroda, T. Mano, K. Sakoda, G. Kido, N. Koguchi, L. Cavigli, M. Gurioli, S. Sanguinetti

  Physica E: Low-dimensional Systems and Nanostructures, Volume 40, Issue 6, April 2008, Pages 1982-1984

- **Photon correlation for exciton complexes in single GaAs self-assembled quantum dots**

  T. Kuroda, M. Abbarchi, T. Mano, K. Watanabe, M. Yamagiwa, K. Kuroda, K. Sakoda, G. Kido, N. Koguchi, C. Mastrandrea, L. Cavigli, M. Gurioli, Y. Ogawa, and F. Minami

  Appl. Phys. Exp. 1 (2008) 042001

- **Carrier Dynamics in Individual Concentric Quantum Rings.**

  S. Sanguinetti, M. Abbarchi, A. Vinattieri, M. Zamfirescu, M. Gurioli, T.Mano, T. Kuroda, and N. Koguchi.

  Phys. Rev. B 77, 125404 (2008)

- **Phonon sideband recombination kinetics in single quantum dots.**

M. Abbarchi, A. Vinattieri, M. Gurioli, S. Sanguinetti, M. Bonfanti, T.Mano, K.Watanabe, T. Kuroda, and N. Koguchi.

J. Appl. Phys. 104, 023504 (2008)

- **Purcell Effect In Micropillars With Oxidized Bragg Mirrors**

  L. Cavigli, L. Lunghi, M. Abbarchi, A. Vinattieri, B. Alloing, C. Zinoni, A. Fiore, A. Gerardino, P. Frigeri, L. Seravalli, S. Franchi, M. Gurioli.

  phys. stat. sol. (c) 5, No. 7, 2433–2436 (2008)

- **Quantum dots to double concentric quantum ring structures transition**

  S. Bietti, C. Somaschini, N. Koguchi, S. Sanguinetti, M. Gurioli, M. Abbarchi, A. Vinattieri, T. Kuroda, T. Mano and K. Sakoda

  Submitted to phys. stat. sol. (c)

- **Line broadening of excitonic complexes in self assembled GaAs/AlGaAs single quantum dot**

  M. Abbarchi, T. Kuroda, C. Mastrandrea, A. Vinattieri, M. Gurioli, T. Mano, N. Koguchi, K. Sakoda

  Accepted phys. stat. sol. (c)

- **High resolution spectroscopy of self assembled single GaAs/AlGaAs quantum dot**

  M. Abbarchi, T. Kuroda, C. Mastrandrea, A. Vinattieri, M. Gurioli, T. Mano, N. Koguchi, K. Sakoda

  Accepted phys. stat. sol. (c)

- **Spectral diffusion and line broadening in single self-assembled GaAs/AlGaAs quantum dot photoluminescence**

  M. Abbarchi, F. Troiani, C. Mastrandrea, G. Goldoni, T. Kuroda, T. Mano, K. Sakoda, N. Koguchi, S. Sanguinetti, A. Vinattieri and M. Gurioli, ,

  Appl. Phys. Lett. 93, 162101 (2008)

- **Exciton fine structure in strain-free GaAs/$Al_{0.3}Ga_{0.7}As$ quantum dots: Extrinsic effects**

  M. Abbarchi, C. A. Mastrandrea, T. Kuroda, T. Mano, K. Sakoda, N. Koguchi, S. Sanguinetti, A. Vinattieri, and M. Gurioli

  Phys. Rev. B 78, 125321 (2008)

- **Single photon emission from GaAs/AlGaAs concentric quantum ring**

  M. Abbarchi, S. Sanguinetti, T. Kuroda, C. Mastrandrea, A. Vinattieri, M. Gurioli, T. Mano, N. Koguchi, K. Sakoda

  submitted to Phys. Rev. B(R)

- **Rapid Thermal Annealing Effects on Self–Assembled Quantum Dot and Quantum Ring Structures**

  S. Sanguinetti, T. Mano, A. Gerosa, C. Somaschini, S. Bietti, N. Koguchi, E. Grilli, M. Guzzi, M. Gurioli, and M. Abbarchi

  In press on J. Appl. Phys.

- **Single quantum dots emission by nanoscale selective growth of InAs on GaAs: a bottom-up approach**

Fulvia Patella, Fabrizio Arciprete , Ernesto Placidi , Massimo Fanfoni , Adalberto Balzarotti , Anna Vinattieri , Lucia Cavigli , Marco Abbarchi , Massimo Gurioli , Lamberto Lunghi , Annamaria Gerardino.

In press on Appl. Phys. Lett.

- **Bunching visibility for correlated photons from single GaAs quantum dots**

  T. Kuroda, Belhadj, M. Abbarchi, C. A. Mastrandrea, M. Gurioli, T. Mano, N. Ikeda, Y. Sugimoto, K. Asakawa, N. Koguchi, K. Sakoda, B. Urbaszek, T. Amand, and X. Marie.

  accepted to Phys. Rev. B(R)

Bibliography

[1] N. Zurauskiene, S. S. Asmontas, A. Dargys, J. Kundrotas, G. Janssen, E. Goovaerts, J. H. Wolter S. Marcinkevicius, P. M. Koenraad, and R. Leon. Semiconductor nanostructures for infrared applications. *Functional Nanomaterials for Optoelectronics and Other Applications (Solid State Phenomena)*, 99-100:99–108, 2003.

[2] O. Manasreh. In *Semiconductor Heterojunctions and Nanostructures*. New York: McGraw Hill, 2005.

[3] T. Steiner. In *Semiconductor Nanostructures for Optoelectronic Applications*. Norwood: Artech House Inc, 2004.

[4] M. Geiger, A. Bauknecht, F. Adler, H. Schweizer, and F. Scholz. Observation of the 2D-3D growth mode transition in the InAs/GaAs system. *J. Crystal Growth*, 170:558–562, 1997.

[5] M. Grundmann and D. Bimberg. Formation of quantum dots in twofold cleaved edge overgrowth. *Phys. Rev. B*, 55:4054–4056, 1997.

[6] E. Bockenhoff and H. Benisty. Evolution of 3d growth-patterns on nonplanar substrates. *Journal of Crystal Growth*, 114:619–632, 1991.

[7] T. C. Hasenberg, P. S. Day, E. M. Shaw, D. J. Magarreli, J. T. Olesberg, C. Yu, T. F. Boggess, and M. E. Flatte. Molecular beam epitaxy growth and characterization of broken-gap (type II) superlattices and quantum wells for midwave-infrared laser diodes. *Journal of Vacuum Science and Technology B*, 18:1623–1627, 2000.

[8] F. Heinrichsdorff, A. Krost, M. Grundmann, D. Bimberg, F. Bertram, J. Christen, A. Kosogov, and P. Werner. Self organization phenomena of InGaAs/GaAs quantum dots grown by metalorganic chemical vapour deposition. *J. of Crystal Growth*, 170:568–573, 1997.

[9] T. R. Ramachandran, A. Madhukar, I. Mukhametzhanov, R. Heitz, A. Kalburge, Q. Xie, and P. Chen. Nature of Stranski-Krastanow growth of InAs on GaAs(001). *Journal of Vacuum Science and Technology B*, 16:1330–1333, 1998.

[10] U. Bockelmann, W. Heller, A. Filoramo, and P. Roussignol. Microphotoluminescence studies of single quantum dots. *Phys. Rev. B*, 55:4456–4468, 1997.

[11] K. Brunner, U. Bockelmann, G. Abstreiter, M. Walther, G. Bohm, G. Trankle, and G. Weimann. Photoluminescence from a single GaAs/AlGaAs quantum dot. *Phys. Rev. Lett.*, 69:3216–3219, 1992.

[12] R. Heitz, O. Stier, I. Mukhametzhanov, A. Madhukar, and D. Bimberg. Quantum size effect in self-organized InAs/GaAs quantum dots. *Phys. Rev. B*, 62:11017–11028, 2000.

[13] Valery Zwiller, Thomas Aichele, and Oliver Benson. Quantum optics with single quantum dot devices. *New Journal of Physics*, 6:96, 2004.

[14] Brahim Lounis and Michel Orrit. Single-photon sources. *Rep. Prog. Phys.*, 68:1129–1179, 200.

[15] C. Santori, M. Pelton, G. Salomon, Y. Dale, and Y. Yamamoto. Triggered single photons from a quantum dot. *Phys. Rev. Lett.*, 86:1502, 2001.

[16] E. Knill, R. Laflamme, and G.J. Milburn. A scheme for efficient quantum computation with linear optics. *Nat.*, 409:46, 2002.

[17] M. Pelton O. Benson, C. Santori and Y. Yamamoto. Regulated and entangled photons from a single quantum dot. *Phys. Rev. Lett.*, 84:2513–2516, 2000.

[18] R. M. Stevenson, R. J. Young, P. Atkinson, D. A. Ritchie, and A. J. Shields. A semiconductor source of triggered entangled photon pairs. *Nat.*, 439:179, 2006.

[19] N. Akopian, N. H. Lindner, E. Poem, Y. Berlatzky, J. Avron, D. Gershoni, B. D. Gerardot, and P. M. Petroff. Entangled photon pairs from semiconductor quantum dots. *Phys. Rev. Lett.*, 96:130501, 2006.

[20] C. H. Bennett, G. Brassard, and A.K. Eckert. Quantum cryptography. *Scientific American*, 267:50–57, 1992.

[21] A. Einstein, B. Podolsky, and N. Rosen. Can quantum-mechanical description of physical reality be considered complete? *Phys. Rev.*, 47(10):777–780, May 1935.

[22] Alain Aspect, Philippe Grangier, and Gérard Roger. Experimental tests of realistic local theories via bell's theorem. *Phys. Rev. Lett.*, 47(7):460–463, Aug 1981.

[23] Charles H. Bennett, Gilles Brassard, Sandu Popescu, Benjamin Schumacher, John A. Smolin, and William K. Wootters. Purification of noisy entanglement and faithful teleportation via noisy channels. *Phys. Rev. Lett.*, 76(5):722–725, Jan 1996.

[24] D. Loss and D. P. DiVincenzo. Quantum computation with quantum dots. *Phys. Rev. A*, 57:120, 2000.

[25] M. Sherwin, A. Imamoglu, and T. Montroy. Quantum computation with quantum dots and terahertz cavity quantum electrodynamics. *Phys. Rev. A*, 60:3508, 1999.

[26] T. Tanamoto. Quantum gates by coupled asymmetric quantum dots and controlled-not-gate operation. *Phys. Rev. A*, 61:022305, 1999.

[27] R. Loudon. In *The quantum theory of light*. Oxford, Oxford, 1973.

[28] D. Fattal, K. Inoue, J. Vuckovic, C. Santori, G. S. Solomon, and Y. Yamamoto. Entanglement formation and violation of bellŠs inequality with a semiconductor single photon source. *Phys. Rev. Lett.*, 92:037903, 2004.

[29] R. M. Stevenson, R. J. Young, P. Atkinson, K. Cooper, D.A.Ritchie, and A.J.Shields. *Nature*, 439:179, 2006.

[30] A. Imamoglu, D. D. Awschalom, G. Burkard, D. P. DiVincenzo, D. Loss, M. Sherwin, and A. Small. Quantum information processing using quantum dot spins and cavity qed. *Phys. Rev. Lett.*, 83:4204, 1999.

[31] David P. DiVincenzo. The physical implementation of quantum computation. *Fortschr. Phys.*, 48:9–11, 2000.

[32] Lorenzo Pavesi and Mario Guzzi. Photoluminescence of $al_xga_{1-x}as$ alloys. *J. Appl. Phys.*, 75:4779, 1994.

[33] D. Gammon, E. S. Snow, B. V. Shanabrook, D. S. Katzer, and D. Park. Homogeneous linewidths in the optical spectrum of a single gallium arsenide quantum dot. *Science*, 273:87, 1996.

[34] N. Koguchi, S. Takahashi, and T. Chikyow. New mbe method for InSb quantum well boxes. *Journal of Crystal Growth*, 111:688–692, 1991.

[35] D. Leonard, M. Krishnamurthy, C. M. Reaves, S. P. Denbaars, and P. M. Petroff. Direct formation of quantum-sized dots from uniform coherent islands of InAs on GaAs surfaces. *Appl. Phys. Lett.*, 63:3203, 1993.

[36] T. Mano and N. Koguchi. Nanometer-scale GaAs ringstructure grown by droplet epitaxy. *J. of Crystal Growth*, 278:108, 2005.

[37] M. Yamagiwa, T. Mano, T. Kuroda, T. Tateno, K. Sakoda, G. Kido, N. Koguchi, and F. Minami. Self-assembly of laterally aligned GaAs quantum dot pairs. *Appl. Phys. Lett.*, 89:113115, 2006.

[38] T. Kuroda, M. Abbarchi, T. Mano, K. Watanabe, M. Yamagiwa, K. Kuroda, K. Sakoda, G. Kido, N. Koguchi, C. Mastrandrea, L. Cavigli, M. Gurioliand Y. Ogawa, and F. Minami. Photon correlation in GaAs self-assembled quantum dots. *Appl. Phys. Express.*, 1:0420014779, 2004.

[39] M. Abbarchi, M. Gurioli, S. Sanguinetti, M. Zamfirescu, A. Vinattieri, and N. Koguchi. Recombination lifetime of single GaAs/AlGaAs quantum dots. *phys. stat. sol. (c)*, 3:3860, 2006.

[40] E. Dekel, D. Gershoni, E. Ehrenfreund, J. M. Garcia, and P. M. Petroff. Carrier-carrier correlations in an optically excited single semiconductor quantum dot. *Phys. Rev. B*, 61:11009, 2000.

[41] M. Bayer, A. Kuther, F. Schaĺfer, J.P. Reithmaier, and A. Forchel. Strong variation of the exciton g factors in self-assembled $in_{0.6}ga_{0.4}as$/gaas quantum dots. *Phys. Rev. B*, 60:8481, 1999.

[42] R. Seguin, A. Schliwa, S. Rodt, K. Pötschke, U.W. Pohl, and D. Bimberg. Size-dependent fine-structure splitting in self-organized inas/gaas quantum dots. *Phys. Rev. Lett.*, 95:257402, 2005.

[43] A. Kuther, M. Bayer, A. Forchel, A. Gobunov, V. B. Timofeev, F. Schäfer, and J. P. Reithmaier. Zeman splitting of excitons and biexcitons in single $In_{0.6}Ga_{0.4}As$/GaAs self–assembled quantum dots. *Phys. Rev. B*, 58:7508, 1998.

[44] V. D. Kulakovskii, G. Bacher, R. Weigand, T. Kummell, A. Forchel, E. Borovitskaya, K. Leonardi, and D. Hommel. *Phys. Rev. Lett.*, 82:1780, 1999.

[45] Filippo Troiani and Carlos Tejedor. Entangled photon pairs from a quantum-dot cascade decay: The effect of time reordering. *Physical Review B*, 78(15):155305, 2008.

[46] N. Akopian, N. H. Lindner, E. Poem, Y. Berlatzky, J. Avron, D. Gershoni, B. D. Gerardot, and P. M. Petroff. *Phys. Rev. Lett.*, 96:130501, 2006.

[47] C. Klingshirn. *Semiconductors opitcs*. Springer-Verlag, 2005.

[48] G. Bastard. *Wave Mechanics Applied to Semiconductor Heterostructures*. Les Editions de Physique, 1990.

[49] P. Y. Yu and M. Cardona. *Fundamentals of Semiconductors*. Springer, Berlin, 1996.

[50] U. Bockelmann and G. Bastard. Interband absorption in quantum wires. i. zero-magnetic-field case. *Phys. Rev. B*, 45:1688, 1992.

[51] D. Y. Dupertuis M. A. Gustafsson A. ; Reinhardt F. Kapon E Vouilloz, F. Oberli. Effect of lateral confinement on valence-band mixing and polarization anisotropy in quantum wires. *Phys. Rev. B*, 57:12387, 1998.

[52] E. L. Ivchenko and A. A. Kiselev. Electron g factor in quantum wires and quantum dots. *JETP Lett.*, 67:43, 1998.

[53] B. Xu P. Jin C. Zhao, Y. H. Chen and Z. G. Wang. Evolution of inas nanostructures grown by droplet epitaxy. *Appl. Phys. Lett.*, 91:033112, 2007.

[54] L. G. Wang, P. Kratzer, N. Moll, and M. Scheffler. Size, shape, and stability of InAs quantum dots on the GaAs (001) substrate. *Phys. Rev. B*, 62:1897, 2000.

[55] V. Mantovani, S. Sanguinetti, M. Guzzi, E. Grilli, M. Gurioli, K. Watanabe, and K. Koguchi. Low density GaAs/AlGaAs quantum dots grown by modified droplet epitaxy. *J. Appl. Phys.*, 96:4416, 2004.

[56] K. Watanabe, N. Koguchi, and Y. Gotoh. Gabrication of GaAs quantum dots by modified droplet epitaxy. *Jpn. J. Appl. Phys.*, 39:L79, 2000.

[57] T. Kuroda, S. Sanguinetti, M. Gurioli, K. Watanabe, F. Minami, and N. Koguchi. Picosecond nonlinear relaxation of photoinjected carriers in a single $GaAs/Al_{0.3}Ga_{0.7}As$ quantum dot. *Phys. Rev. B*, 66:121302(R), 2002.

[58] S. Sanguinetti, E. Poliani, M. Bonfanti, M. Guzzi, E. Grilli, M. Gurioli, and N. Koguchi. Electron-phonon interaction in individual strain-free $GaAs/Al_{0.3}Ga_{0.7}As$ quantum dots. *Phys. Rev. B*, 73:125342, 2006.

[59] Takaaki Mano, Takashi Kuroda, Stefano Sanguinetti, Tetsuyuki Ochiai, Takahiro Tateno, Jongsu Kim, Takeshi Noda, Mitsuo Kawabe, Kazuaki Sakoda, Giyuu Kido, and Nobuyuki Koguchi. Self-assembly of concentric quantum double rings. *Nano Lett.*, 5:425, 2005.

[60] T. Kuroda, T. Mano, T. Ochiai, S. Sanguinetti, K. Sakoda, G. Kido, and N. Koguchi. Optical transitions in quantum ring complexes. *Phys. Rev. B*, 72:205301, 2005.

[61] S. Sanguinetti, M. Abbarchi, A. Vinattieri, M. Zamfirescu, M. Gurioli, T. Mano, T. Kuroda, and N. Koguchi. Carrier dynamics in individual concentric quantum rings: Photoluminescence measurements. *Phys. Rev. B*, 77:125404, 2008.

[62] Yoshiji Horikoshi, Minoru Kawashima, and Hiroshi Yamaguchi. Migration-enhanced epitaxy of GaAs and AlGaAs. *Jpn. J. Appl. Phys.*, 27:169, 1988.

[63] Ch. Heyn, A. Stemmann, A. Schramm, H. Welsch, , W. Hansen, and A. Nemcsics. Regimes of GaAs quantum dot self-assembly by droplet epitaxy. *Phys. Rev. B*, 76:075317, 2007.

[64] S. Sanguinetti, T. Mano, A. Gerosa, C. Somaschini, S. Bietti, N. Koguchi, E. Grilli, M. Guzzi, M. Gurioli, , and M. Abbarchi. Rapid thermal annealing effects on selfŰ-assembled quantum dot and quantum ring structures. *J. Appl. Phys.*, in press, 2008.

[65] B. Patton, W. Langbein, and U. Woggon. Trion, biexciton and exciton dynamics in single self-assembled CdSe quantum dots. *Phys. Rev. B*, 68:125316, 2003.

[66] E. S. Moskalenko, M. Larsson, W. V. Schoenfeld, P. M. Petroff, and P. O. Holtz. Carrier transport in self–organized InAs/GaAs quantum-dot structures studied by single–dot spectroscopy. *Phys. Rev. B*, 27:155336, 2006.

[67] Young-Jun Yu, In-Taek Jeong, Jong-Chun Woo, and Wonho Jhe. Near-field spectroscopy of bimodal size distribution of InAs/AlGaAs single quantum dots. *Appl. Phys. Lett.*, 87:143108, 2005.

[68] P. G. Gucciardi, A. Vinattieri, M. Colocci, B. DamilanoĘ, N. Grandjean, F. SemondĘ, and J. MassiesĘ. Photoluminescence properties of multiple stacked planes of GaN/AlN quantum dots studied by near-field optical microscopy. *Journ. of Microsc.*, 202:212, 2001.

[69] J. Kudrna, P.G. Gucciardi, A. Vinattieri, M. Colocci, B. Damilano, F. Semond, N. Grandjean, and J. Massies. Steady-state and time-resolved near-field optical spectroscopy of GaN/AlN quantum dots and InGaN/GaN quantum wells. *Phys. Stat. Sol. (a)*, 190:155, 2002.

[70] B. Lounis, H. A. Bechtel, D. Gerion, A. P. Alivisatos, and W. E. Moerner. Photon antibunching in single CdSe/ZnS quantum dot fluorescence. *Chem. Phys. Lett.*, 329:399–404, 2000.

[71] V. Mantovani, S. Sanguinetti, M. Guzzi, E. Grilli, M. Gurioli, K. Watanabe, and N. Koguchi. Low density GaAs/AlGaAs quantum dots grown by modified droplet epitaxy: Ga coverage and post growth annealing effects. *J. Appl. Phys.*, 96:4416, 2004.

[72] E. Dekel, D. V. Regelman, D. Gershoni, E. Ehrenfreund, W. V. Schoenfeld, and P. M. Petroff. Cascade evolution and radiative recombination of quantum dot multiexcitons studied by time-resolved spectroscopy. *Phys. Rev. B*, 62:11038, 2000.

[73] S. A. Empedocles, D. J. Norris, and M. G. Bawendi. Photoluminescence spectroscopy of single CdSe nanocrystallite quantum dots. *Phys. Rev. Lett.*, 77:3873, 1996.

[74] H. D. Robinson, B. B. Goldberg, L. Marsal, and H. Mariette. Light-induced spectral diffusion in single self–assembled quantum dots. *Phys. Rev. B*, 61:R5086, 2000.

[75] L. Besombes, K. Kheng, L. Marsal, and H. Mariette. Few-particle effects in single CdTe quantum dots. *Phys. Rev. B*, 65:121314, 2002.

[76] I. Favero, A. Berthelot, G. Cassabois, C. Voisin, C. Delalande, Ph. Roussignol, R. Ferreira, and J. M. Gerard. Temperature dependence of the zero-phonon linewidth in quantum dots: An effect of the fluctuating environment. *Phys. Rev. B*, 75:073308, 2007.

[77] A. Berthelot, I. Favero, G. Cassabois, C. Voisin, C. Delalande, Ph. Roussignol, R. Ferreira, and J. M. Gerard. Unconventional motional narrowing in the optical spectrum of a semiconductor quantum dot. *Nature Phys.*, 2:759, 2006.

[78] Mitsuru Sugisaki, Hong-Wen Ren, Selvakumar V. Nair, Kenichi Nishi, Shigeo Sugou, Tsuyoshi Okuno, and Yasuaki Masumoto. Optical anisotropy in self-assembled InP quantum dots. *Phys. Rev. B*, 59(8):R5300–R5303, Feb 1999.

[79] Gabriel Bester, Selvakumar Nair, and Alex Zunger. Pseudopotential calculation of the excitonic fine structure of million-atom self-assembled $In_{1-x}Ga_xAs/GaAs$ quantum dots. *Phys. Rev. B*, 67(16):161306, Apr 2003.

[80] D. Bellucci, F. Troiani, G. Goldoni, and E. Molinari. Neutral and charged electron-hole complexes in artificial molecules: Quantum transitions induced by the in-plane magnetic field. *Phys. Rev. B*, 70:205332, 2004.

[81] S. Fafard, S. Rymond, G. Wand, R. Leon, D. Leonard, S. Charbonneau, J. L. Merz, P. M. Petroff, and J. E. Bowers. Temperature effects on the radiative recombination in self–asembled quantum dots. *Surface Science*, 361/362:778, 1996.

[82] R. Heitz, I. Mukhametzhanov, A. Madhukar, A. Hoffmann, and D. Bimberg. Temperature dependent optical properties of self–organized InAs/GaAs quantum dots. *J. Electronic Materials*, 28:520, 1999.

[83] G. Ortner, M. Schwab, M. Bayer, R. Passler, S. Fafard, Z. Wasilewski, P. Hawrylak, and A. Forchel. Temperature dependence of the excitonic band gap in $In_xGa_{1-x}As$/GaAs self-assembled quantum dots. *Phys. Rev. B*, 72:085328, 2005.

[84] P. Borri, W. Langbein, S. Schneider, U. Woggon, R. L. Sellin, D. Ouyang, and D. Bimberg. Ultralong dephasing time in InGaAs quantum dots. *Phys. Rev. Lett.*, 87:157401, 2001.

[85] M. Bayer, G. Ortner, O. Stern, A. Kuther, A. A. Gorbunov, A. Forchel, P. Hawrylak, S. Fafard, K. Hinzer, T. L. Reinecke, S. N. Walck, J. P. Reithmaier, K. Klopf, and F. Schafer. *Phys. Rev. B*, 65:195315, 2002.

[86] C. Kammerer, C. Voisin, G. Cassabois, C. Delalande, Ph. Roussignol, F. Klopf, J. P. Reithmaier, A. Forchel, and J. M. Gérard. Line narrowing in single semiconductor quantum dots: Toward the control of environment effects. *Phys. Rev. B*, 66:041306(R), 2002.

[87] I. Favero, G. Cassabois, R. Ferreira, D. Darson, C. Voisin, J. Tignon, C. Delalande, G. Bastard, Ph. Roussignol, and J. M. Gerard. Acoustic phonon sidebands in the emission line of single InAs/GaAs quantum dots. *Phys. Rev. B*, 68:233301, 2003.

[88] P. Borri, W. Langbein, U. Woggon, V. Stavarache, D. Reuter, and A. D. Wieck. Exciton dephasing via phonon interactions in InAs quantum dots: Dependence on quantum confinement. *Phys. Rev. B*, 71:115328, 2005.

[89] E. A. Muljarov and R. Zimmermann. Dephasing in quantum dots: Quadratic coupling to acoustic phonons. *Phys. Rev. Lett.*, 93:237401, 2004.

[90] Charles Santori, Glenn S. Solomon, Matthew Pelton, and Yoshihisa Yamamoto. Time-resolved spectroscopy of multiexcitonic decay in an InAs quantum dot. *Phys. Rev. B*, 65(7):073310, Feb 2002.

[91] P. Borri, W. Langbein, J. Mork, J. M. Hvam, F. Heinrichsdorff, M. H. Mao, and D. Bimberg. Dephasing in InAs/GaAs quantum dots. *Phys. Rev. B*, 60:7784, 1999.

[92] D. Birkedal, K. Leosson, and J. M. Hvam. Long lived coherence in self-assembled quantum dots. *Phys. Rev. Lett.*, 87:227401, 2001.

[93] L. Besombes, K. Kheng, L. Marsal, and H. Mariette. Acoustic phonon broadening mechanism in single quantum dot emission. *Phys. Rev. B*, 63:155307, 2001.

[94] B. Krummheuer, V. M. Axt, and T. Kuhn. Theory of pure dephasing and the resulting absorption line shape in semiconductor quantum dots. *Phys. Rev. B*, 65:195313, 2002.

[95] Phedon Palinginis, Hailin Wang, Serguei V. Goupalov, D. S. Citrin, M. Dobrowolska, and J. K. Furdyna. Exciton dephasing in self-assembled CdSe quantum dots. *Phys. Rev. B*, 70:073302, 2004.

[96] T. Takagahara. Theory of exciton dephasing in semiconductor quantum dots. *Phys. Rev. B*, 60:2638, 1999.

[97] D. Alderighi, Anna Vinattieri, F. Bogani, Marcello Colocci, Stefano Gottardo, N. Grandjean, and J. Massies. Phonon replica dynamics in high quality GaN epilayers and AlGaN/GaN quantum wells. *Phys.Stat.Sol. (a)*, 183:129, 2001.

[98] B. Patton, W. Langbein, and U. Woggon. Dynamics of excitons, multiexcitons and trion states in II-VI quantum dots. In A. R. Long and J. H. Davies, editors, *Physics of Semiconductors 2002: Proceedings of the 26th International Conference on the Physics of Semiconductors*, Bristol, 2003. Institute of Physics.

[99] H. D. Robinson and B. B. Goldberg. Light-induced spectral diffusion in single self-assembled quantum dots. *Phys. Rev. B*, 61:R5086, 2000.

[100] M. Califano and P. Harrison. Presentation and experimental validation of a single-band, constant-potential model for self-assembled InAs/GaAs quantum dots. *Phys. Rev. B*, 61:10959, 2000.

[101] J. Y. Marzin and G. Bastard. Calculation of the energy levels in InAs/GaAs quantum dots. *Solid State Comm.*, 92(5):437–442, 1994.

[102] D. Bimberg, M. Grundmann, and N. N. Ledentsov. *Quantum Dots Heterostructures*. Wiley, New York, 1999.

[103] J. Bellessa, V. Voliotis, R. Grousson, X. L. Wang, M. Ogura, and H. Matsuhata. Quantum-size effects on radiative lifetimes and relaxation of excitons in semiconductor nanostructures. *Phys. Rev. B*, 58(15):9933–9940, Oct 1998.

[104] Mitsuru Sugawara. Theory of spontaneous-emission lifetime of wannier excitons in mesoscopic semiconductor quantum disks. *Phys. Rev. B*, 51(16):10743–10754, Apr 1995.

[105] O. Stier, M. Grundmann, and D. Bimberg. Electronic and optical properties of strained quantum dots modeled by 8-band k p theory. *Phys. Rev. B*, 59:5688, 1999.

[106] Gustavo A. Narvaez, Gabriel Bester, and Alex Zunger. Excitons, biexcitons, and trions in self-assembled (In,Ga)As/GaAs quantum dots: Recombination energies, polarization, and radiative lifetimes versus dot height. *Phys. Rev. B*, 72(24):245318, 2005.

[107] R. Heitz, M. Veit, N. N. Ledentsov, A. Hoffmann, D. Bimberg, V. M. Ustinov, P. S. Kop'ev, and Zh. I. Alferov. Energy relaxation by multiphonon processes in InAs/GaAs quantum dots. *Phys. Rev. B*, 56:10435, 1997.

[108] Thomas F. Boggess, D. L. Huffaker L. Zhang D. G. Deppe, and C. Cao. Spectral engineering of carrier dynamics in In(Ga)As self-assembled quantum dots. *Appl. Phys. Lett.*, 78:276, 2001.

[109] S. Malik, E. C. Le Ru, D. Childs, and R. Murray. Time-resolved studies of annealed InAs/GaAs Self-Assembled quantum dots. *Phys. Rev. B*, 63:155313, 2001.

[110] S. Pellegrini L. Ya. Karachinsky, G. S. Buller, A. S. Shkolnik, N. Yu. Gordeev, V. P. Evtikhiev A. F. Ioffe, and V. B. Novikov. Spectral engineering of carrier dynamics in In(Ga)As self-assembled quantum dots. *Appl. Phys. Lett.*, 84:7, 2004.

[111] M. Bayer and A. Forchel. Temperature dependence of the exciton homogeneous linewidth in $In_{0.60}Ga_{0.40}As$/GaAs self-assembled quantum dots. *Phys. Rev. B*, 65:041308(R), 2002.

[112] T. Nakaoka, T. Saito, J. Tatebayashi, and Y. Arakawa. Size, shape, and strain dependence of the g factor in self-assembled In(Ga)As quantum dots. *Phys. Rev. B*, 70(23):235337, Dec 2004.

[113] M. J. Snelling, E. Blackwood, C. J. McDonagh, R. T. Harley, and C. T. B. Foxon. Exciton, heavy-hole, and electron g factors in type-I GaAs/Al_xGa_{1-x}As quantum wells. *Physical Review B (Condensed Matter)*, 45(7):3922–3925, 1992.

[114] T. A. Kennedy M. Rosen D. S. Katzer D. Park S. W. Brown V. L. Korenev I. A. Mrkulov D. Gammon, Al. L. Efros. Electron and nuclear spin interactions in the optical spectra of single GaAs quantum dots. *Phys. Rev. Lett.*, 86:5176, 2001.

[115] N. I. Cade, H. Gotoh, H. Kamada, H. Nakano, and H. Okamoto. Fine structure and magneto-optics of exciton, trion, and charged biexciton states in single InAs quantum dots emitting at 1.3 μm. *Physical Review B*, 73(11):115322, 2006.

[116] D. F. Nelson, R. C. Miller, and D. A. Kleinman. Band nonparabolicity effects in semiconductor quantum wells. *Physical Review B (Condensed Matter)*, 35(14):7770–7773, 1987.

[117] Emil S. Koteles and J. Y. Chi. Experimental exciton binding energies in GaAs/Al_xGa_{1-x}As quantum wells as a function of well width. *Phys. Rev. B*, 37(11):6332–6335, Apr 1988.

[118] Bouwmeester. *D. Bouwmeester, A. Ekert, A. Zeilinger, The Physics of Quantum Information*. Springer, Berlin, 2000.

[119] A. I. Tartakovskii, M. N. Makhonin, I. R. Sellers, J. Cahill, A. D. Andreev, D. M. Whittaker, J-P. R. Wells, A. M. Fox, D. J. Mowbray, M. S. Skolnick,

K. M. Groom, M. J. Steer, H. Y. Liu, , and M. Hopkinson. Effect of thermal annealing and strain engineering on the fine structure of quantum dot excitons. *Phys. Rev. B*, 70:193303, 2004.

[120] M. S. Skolnick A. D. Ashmore C. Baker Finley J. J. Finley, D. J. Mowbray and A. F. G. Monte M. Hopkinson. Fine structure of charged and neutral excitons in $InAs/Al_{0.6}Ga_{0.4}As$ quantum dots. *Phys. Rev. B*, 66:153316, 2002.

[121] E. L. Ivchenko S. V. Gupalov and A. V. Kovokin. *JETP*, 86:388, 1998.

[122] T. Takagahara. Theory of exciton doublet structures and polarization relaxation in single quantum dots. *Phys. Rev. B*, 62:16840, 2000.

[123] G. Bester and A. Zunger. Cylindrically shaped zinc-blende semiconductor quantum dots do not have cylindrical symmetry: Atomistic symmetry, atomic relaxation, and piezoelectric effects. *Phys. Rev. B*, 71:045318, 2005.

[124] M. Winkelnkemper A. Schliwa and D. Bimberg. Impact of size, shape, and composition on piezoelectric effects and electronic properties of In(Ga)As/GaAs quantum dots. *Phys. Rev. B*, 76:205324, 2007.

[125] M. Galluppi, A. Frova, M. Capizzi, F. Boscherini, P. Frigeri, S. Franchi, and A. Passaseo. Atomic equilibrium concentrations in (InGa)As quantum dots. *Appl. Phys. Lett.*, 78:3121, 2001.

[126] N. Liu, J. Tersoff, O. Baklenov, A. L. Holmes, and C. K. Shih. Nonuniform composition profile in $In_{0.5}Ga_{0.5}As$ alloy quantum dots. *Phys. Rev. Lett.*, 84:334, 2000.

[127] I. Marderfeld D. Galushko N. Akopian E. Poem, J. Shemesh, A. Badolato D. Gershoni, B. D. Gerardot, and P. M. Petroff. Polarization sensitive spectroscopy of charged quantum dots. *Phys. Rev. B.*, 76:235304, 2007.

[128] S.Sanguinetti, K.Watanabe, T.Kuroda, F.Minami, Y.Gotoh, and N.Koguchi. Effects of post growth annealing on the optical properties of self assembled GaAs/AlGaAs quantum dots. *J. Crystal Growth*, 242:321, 2002.

[129] T. Mano B. Urbaszek K. Sakoda N. Koguchi T. Amand T. Belhadj, T. Kuroda and X. Marie. Optically monitored nuclear spin dynamics in individual droplet expitaxy quantum dots. *(not published)*, 2008.

[130] X. Wu G. Bester, A. Zunger and D. Vanderbilt. Effects of linear and nonlinear piezoelectricity on the electronic properties of InAs/GaAs quantum dots. *Phys. Rev. B*, 74:081305, 2006.

[131] P. A. Dalgarno B. D. Gerardot, a S. Seidl and R. J. Warburton. Manipulating exciton fine structure in quantum dots with a lateral electric field. *Appl. Phys. Lett.*, 90:041101, 2005.

[132] E. L. Ivchenko V. L. Korenev Yu. G. Kusraev N. N. Ledentsov V. M. Ustinov A. E. Zhukov R. I. Dzhioev, B. P. Zakharchenya and A. F. TsatsulŠnikov. *JETP Lett.*, 65:804, 1997.

[133] R. Ferreira. Exhange coupling and polarization relaxation in self assembled quantum dots. *Physica E*, 13:216, 2002.

[134] P. Michler, A. Imamoglu, M. D. Mason, P. J. Carson, G.F. Strouse, and S.K. Buratto. Quantum correlation among photons from a single quantum dot at room temperature. *Nature*, 406:968, 2000.

[135] P. Michler, A. Kiraz, C. Becher, W. V. Schoenfeld, P. M. Petroff, Lidong Zhang, E. Hu, and A. Imamoglu. A quantum dot single-photon turnstile device. *Science*, 290:2282, 2000.

[136] Valery Zwiller, Hans Blom, Per Jonsson, Nikolay Panev, Soren Jeppesen, Tedros Tsegaye, Edgard Goobar, Mats-Erik Pistol, Lars Samuelson, and Gunnar Bjork. Single quantum dots emit single photons at a time: Antibunching experiments. *Appl. Phys. Lett.*, 78:2476, 2001.

[137] E. Moreau, I. Robert, J. M. Gerard, I. Abram, L. Manin, and V. Thierry-Mieg. Single-mode solid-state single photon source based on isolated quantum dots in pillar microcavities. *App. Phys. Lett.*, 79:2865, 2001.

[138] Zhiliang Yuan, Beata E. Kardynal, R. Mark Stevenson, Andrew J. Shields, Charlene J. Lobo, Ken Cooper, Neil S. Beattie, David A. Ritchie, and Michael Pepper. Electrically driven single-photon source. *Science*, 295:102, 2002.

[139] Kazuya Takemoto, Yoshiki Sakuma, Shinichi Hirose, Tatsuya Usuki, Naoki Yokoyama, Toshiyuki Miyazawa, Motomu Takatsu, and Yasuhiko Arakawa. Non-classical photon emission from a single InAs/InP quantum dot in the 1.3-μm optical-fiber band. *Jpn. J. Appl. Phys.*, 43:205324, 2004.

[140] T. Miyazawa, K. Takemoto, Y. Sakuma, S. Hirose, T. Usuki, N. Yokoyama, M. Takatsu, and Y. Arakawa. Single-photon generation in the 1.55-μm optical-fiber band from an InAs/InP quantum dot. *Jpn. J. Appl. Phys.*, 44:L620, 2005.

[141] C. Zinoni, B. Alloing, C. Monat, V. Zwiller andL. H. Li, A. Fiore, L. Lunghi, A. Gerardino, H. de Riedmatten H. Zbinden, and N. Gisin. Time-resolved and antibunching experiments on single quantum dots at 1300 nm. *Appl. Phys. Lett.*, 88:131102, 2006.

[142] V. Zwiller, T. Aichele, W. Seifert, J. Persson, and O. Benson. Generating visible single photons on demand with single inp quantum dots. *Appl. Phys. Lett.*

[143] S. Kimura, H. Kumano, M. Endo, I. Suemune, T. Yokoi, H. Sasakura, S. Adachi, S. Muto, H. Z. Song, S. Hirose, and T. Usuki. Photon anti-bunching observed from an InAlAs single quantum dot. *Jpn. J. Appl. Phys.*, 44:L793, 2005.

[144] K. Kuroda, T. Kuroda, K. Watanabe, T. Mano, K. Sakoda, G. Kido, and N. Koguchi. Final-state readout of exciton qubits by observing resonantly excited photoluminescence in quantum dots. *Appl. Phys. Lett.*, 90:051909, 2007.

[145] E. Moreau, I. Robert, L. Manin, V. Thierry-Mieg, J. M. Gerard, and I. Abram. Quantum cascade of photons in semiconductor quantum dots. *Phys. Rev. Lett.*, 87:183601, 2001.

[146] T. Kuroda, C. Mastrandrea, M. Abbarchi, and M. Gurioli. Notes on the bunching peak of $g^{(2)}$ functions for correlated photons from single quantum dots. *arXiv.*, page 0801.2460, 2008.

[147] A. Kiraz, S. Falth, C. Becher, B. Gayral, W. V. Schoenfeld, P. M. Petroff, L. Zhang, E. Hu, and A. Imamoglu. Photon correlation spectroscopy of a single quantum dot. *Phys. Rev. B*, 65:161303(R), 2002.

[148] D.V. Regelman, U. Mizrahi, D. Gershoni, E. Ehrenfreund, W.V. Schoenfeld, and P.M. Petroff. Semiconductor quantum dot: A quantum light source of multicolor photons with tunable statistics. *Phys. Rev. Lett*, 25:257401, 2001.

[149] S. Sanguinetti, K. Watanabe, T. Tateno, M. Wakaki, N. Koguchi, T. Kuroda, F. Minami, and M. Gurioli. Role of the wetting layer in the carrier relaxation in quantum dots. *Appl. Phys. Lett.*, 81:613, 2002.

[150] A. Feltrin, J. L. Staehli, B. Deveaud, and V. Savona. Modeling the photoluminescence lifetime in realistic quantum wires. *Phys. Rev. B*, 69:233309, 2004.

[151] Y. Aharonov and D. Bohm. Significance of electromagnetic potentials in the quantum theory. *Phys. Rev.*, 115:485, 1959.

[152] N. A. J. M. Kleemans, I. M. A. Bominaar-Silkens, V. M. Fomin, V. N. Gladilin, D. Granados, A. G. Taboada, J. M. García, P. Offermans, U. Zeitler, P. C. M. Christianen, J. C. Maan, J. T. Devreese, and P. M. Koenraad. Oscillatory persistent currents in self-assembled quantum rings. *Physical Review Letters*, 99(14):146808, 2007.

[153] M. Grochol, F. Grosse, and R. Zimmermann. Optical exciton aharonov-bohm effect, persistent current, and magnetization in semiconductor nanorings of type i and ii. *Physical Review B (Condensed Matter and Materials Physics)*, 74(11):115416, 2006.

[154] I. R. Sellers, V. R. Whiteside, A. O. Govorov, W. C. Fan, W-C. Chou, I. Khan, A. Petrou, and B. D. McCombe. Coherent aharonov-bohm oscillations in type-II (Zn,Mn)Te/ZnSe quantum dots. *Physical Review B (Condensed Matter and Materials Physics)*, 77(24):241302, 2008.

[155] Wen-Hsuan Kuan, Chi-Shung Tang, and Cheng-Hung Chang. Spectral properties and magneto-optical excitations in semiconductor double rings under rashba spin-orbit interaction. *Physical Review B (Condensed Matter and Materials Physics)*, 75(15):155326, 2007.

[156] Axel Lorke, R. Johannes Luyken, Alexander O. Govorov, Jörg P. Kotthaus, J. M. Garcia, and P. M. Petroff. Spectroscopy of nanoscopic semiconductor rings. *Phys. Rev. Lett.*, 84(10):2223–2226, Mar 2000.

[157] T. Ihn T. Heinzel K. Ensslin W. Wegscheider M. Bichler A. Fuhrer, S. Luscher. Energy spectra of quantum rings. *Nature*, 413:822, Oct 2001.

[158] Luis G. G. V. Dias da Silva, José M. Villas-Bôas, and Sergio E. Ulloa. Tunneling and optical control in quantum ring molecules. *Physical Review B (Condensed Matter and Materials Physics)*, 76(15):155306, 2007.

[159] Vincenzo Savona. Effect of interface disorder on quantum well excitons and microcavity polaritons. *J. Phys. Condens. Matter*, 19:295208, 2007.

[160] Valentina Emiliani, Francesca Intonti, Christoph Lienau, Thomas Elsaesser, Richard Nötzel, and Klaus H. Ploog. Near-field optical imaging and spectroscopy of a coupled quantum wire-dot structure. *Phys. Rev. B*, 64(15):155316, Sep 2001.

[161] C. Becher, A. Kiraz, P. Michler, A. Imamoğlu, W. V. Schoenfeld, P. M. Petroff, Lidong Zhang, and E. Hu. Nonclassical radiation from a single self-assembled InAs quantum dot. *Phys. Rev. B*, 63(12):121312, Mar 2001.

[162] A. Feltrin, F. Michelini, J. L. Staehli, B. Deveaud, V. Savona, J. Toquant, X. L. Wang, and M. Ogura. Localization-dependent photoluminescence spectrum of biexcitons in semiconductor quantum wires. *Physical Review Letters*, 95(17):177404, 2005.

[163] F. T. Arecchi, E. Gatti, and A. Sona. Time distribution of photons from coherent and gaussian sources. *Phys. Lett.*, 20:27, 1966.

[164] T. Kuroda, T. Belhadj, M. Abbarchi, C. Mastrandrea, M. Gurioli, T. Mano andN. Ikeda, Y. Sugimoto, K. Asakawa andN. Koguchi, K. Sakoda, B. Urbaszek, T. Amand, and X. Marie. Bunching visibility for correlated photons from single GaAs quantum dots. *Phys. Rev. B*, 2008.

[165] Charles Santori, David Fattal, Jelena Vučković, Glenn S. Solomon, Edo Waks, and Yoshihisa Yamamoto. Submicrosecond correlations in photoluminescence from InAs quantum dots. *Phys. Rev. B*, 69(20):205324, 2004.